TURBIDITY CURRENTS AND SEDIMENTATION IN CLOSED-END CHANNELS

By

CHUNG-PO LIN

A DISSERTATION PRESENTED TO THE GRADUATE SCHOOL
OF THE UNIVERSITY OF FLORIDA IN
PARTIAL FULFILLMENT OF THE REQUIREMENTS
FOR THE DEGREE OF DOCTOR OF PHILOSOPHY

UNIVERSITY OF FLORIDA

1987

ACKNOWLEDGEMENTS

The author would like to express his sincerest appreciation to his advisor and supervisory committee chairman, Dr. Ashish J. Mehta, Associate Professor of Civil Engineering and Coastal and Oceanographic Engineering, for his continuing guidance and support throughout this research. Appreciation is also extended for the valuable advice and suggestions of Dr. B. A. Christensen, Professor of Civil Engineering, as well as the guidance received from Dr. R. G. Dean, Graduate Research Professor of Coastal and Oceanographic Engineering, Dr. D. M. Sheppard, Professor of Coastal and Oceanographic Engineering, and Dr. A. K. Varma, Professor of Mathematics.

Sincere thanks also go to Dr. B. A. Benedict, Dr. Y. Peter Sheng, and Mr. J. W. Lott for their suggestions and help in this study.

Special thanks go to the staff of the Coastal Engineering Laboratory at the University of Florida, Marc Perlin, Vernon Sparkman, and Jim Joiner, and to Messrs. E.C. McNair, Jr. A. Teeter, and S. Heltzel at the U. S. Army Corps Waterways Experiment Station, Vicksburg, Mississippi, for their cooperation and assistance with the experiments. The author wishes to thank Ms. L. Pieter for the drafting of figures, and Ms. L. Lehmann and Ms. H. Twedell of the Coastal Engineering Archives for their assistance.

The support of the National Science Foundation, under grant number CEE-84-01490, is sincerely acknowledged.

Finally, the author would like to thank his wife Ferng Mei-Chiung for her love, moral encouragement and patience, and his parents for their love and support.

TABLE OF CONTENTS

Page

ACKNOWLEDGEMENTS..... ii

LIST OF TABLES..... vi

LIST OF FIGURES..... vii

LIST OF SYMBOLS..... xi

ABSTRACT..... xix

CHAPTERS

1 INTRODUCTION..... 1

1.1 Turbidity Currents and Sedimentation in a Closed-End Channel..... 1
1.2 Approach to the Problems..... 5
1.3 Scope of Investigation..... 8

2 LITERATURE REVIEW..... 11

2.1 Front Behavior of Turbidity Current..... 11
2.2 Stationary Sediment Wedge..... 18
2.3 Mathematical Model..... 21
2.4 Depositional Properties of Fine-Grained Sediments..... 24

3 METHODOLOGY..... 31

3.1 Dimensional Analysis..... 31
3.2 Development of Mathematical Model..... 40
3.3 Analytical Developments..... 57

4 EXPERIMENTAL EQUIPMENT AND PROCEDURES..... 69

4.1 Experiments at WES..... 69
4.2 Experiments at COEL..... 82

5 RESULTS AND DISCUSSION..... 96
5.1 Typical Results..... 96
5.2 Characteristic Test Parameters..... 127
5.3 Characteristic Results..... 127
5.4 Results of Tidel Effect Tests..... 165

6 CONCLUSIONS AND RECOMMENDATIONS..... 173

6.1 Summary of Investigation..... 173
6.2 Conclusions..... 174
6.3 Recommendations for Future Study..... 184

APPENDICES

A GRID SYSTEM, FLOW CHART, AND STABILITY CONDITION FOR MATHEMATICAL MODELING.....187

B FLOW REGIME IN A CLOSED-END CHANNEL..... 193

C COMPUTATION OF MAXIMUM SURFACE RISE..... 201

D CHARACTERISTICS OF CLOSED-END CHANNEL DEPOSITS..... 203

REFERENCES..... 205

BIOGRAPHICAL SKETCH..... 212

LIST OF TABLES

Table		Page
4.1	Chemical Composition of a Water Sample from the 100 m Flume	77
4.2	Summary of Test Conditions at WES	83
4.3	Chemical Composition of the Tap Water	90
4.4	Summary of Test Conditions at COEL	95
5.1	Basic Test Parameters for WES Tests	128
5.2	Basic Test Parameters for COEL Tests	129
5.3	Critical Deposition Shear Stress of Kaolinite	156
C.1	Computation of Maximum Surface Rise	202
D.1	Characteristics of Closed-End Channel Deposits	203

LIST OF FIGURES

Figure		Page
1.1	Schematic of Closed-End Channel and Turbidity Current. (a) Plan View. (b) Elevation View.....	4
2.1	Front Shape of Gravity Current From Theoretical Model.....	13
2.2	Schematic of Mean Flow Relative to a Gravity Current Head Subject to No-Slip Conditions at Its Lower Boundary.....	13
2.3	The Front Position as a Function of Time for Different Releases.....	19
2.4	Median Settling Velocity vs. Concentration for Severn Estuary Mud.....	27
2.5	Suspended Sediment Concentration vs. Time for Three Cohesive Sediments.....	27
2.6	(a) Median Dispersed Grain Size vs. Distance.....	30
	(b) Suspended Sediment Settling Velocity vs. Distance.....	30
3.1	Front Shape of a Propagating Turbidity Current.....	32
3.2	Schematic of Theoretical Two-Layered Model.....	58
3.3	Schematic of Stationary Sediment Wedge and Water Surface Rise.....	66
4.1	Schematic of Hydraulic System at WES.....	70
4.2	A Digital Electric Thermometer at WES.....	73
4.3	Suspension Sampling Apparatus Deployed in the WES Flume.....	73
4.4	Particle Size Distributions of Fine-Grained Sediments.....	74
4.5	Two Different Size Settling Columns with a Mixing Pump.....	76

4.6 Median Settling Velocity vs. Concentration..... 78

4.7 Locations of Measurements in WES Tests (Plan View).... 81

4.8 Schematic of Hydraulic System at COEL (Plan View)..... 84

4.9 Locations of Measurements and Sampling Apparatus.

Measurement Locations (a) Plan..... 87

Suspension Sampling Apparatus (b) Plan, (c) Elevation..... 87

4.10 Electromagnetic Current Meter..... 89

4.11 Water Surface Variation for Tide Effect Tests..... 94

5.1 Main Channel Horizontal Velocity vs. Elevation..... 98

5.2 Main Channel Concentration vs. Elevation..... 98

5.3 Front Position vs. Elapsed Time..... 99

5.4 Instantaneous Front Speed vs. Distance From Entrance..... 101

5.5 Horizontal Velocity at z = 2.5 cm vs. Elapsed Time at Five Locations..... 103

5.6 Horizontal Velocity at z = 2.5 cm vs. Elevation, for Four Times After Gate Opening..... 105

5.7 Horizontal Velocity at Steady State vs. Elevation for Three Locations..... 106

5.8 Horizontal Velocity Contours at Steady State in Closed-End Channel..... 107

5.9 Concentration at z = 0.7 cm vs. Elapsed Time for Five Locations. (calibration Results)..... 109

5.10 Concentration at z = 0.7 cm vs. Elapsed Time for Five Locations. (Verification Results)..... 110

5.11 Concentration at Steady State vs. Elevation for Five Locations. (Calibration Results)..... 112

5.12 Concentration at Steady State vs. Elevation for Five Locations. (Verification Results)..... 113

5.13 Concentration at Front Head vs. Distance From Entrance..... 115

5.14 Mean Concentration Below Interface vs. Distance From Entrance..... 117

5.15 Mean Concentration Below Interface vs. Distance From Entrance. (Verification Results)..... 118

5.16 Concentration Contours at Steady State in Closed-End Channel..... 120

5.17 Surface Elevation Difference vs. Distance From Entrance..... 121

5.18 Sediment Deposition Rate vs. Distance From Entrance. (Calibration Results)..... 123

5.19 Sediment Deposition Rate vs. Distance From Entrance. (Verification Results)..... 124

5.20 Particle Size Distributions of Deposits at Three Locations..... 126

5.21 Front Nose Height to Head Height Ratio vs. Local Head Reynolds Number..... 131

5.22 Front Head Height to Neck Height Ratio vs. Local Neck Reynolds Number..... 132

5.23 Initial Front Speed to Densimetric Velocity Ratio vs. Densimetric Reynolds Number..... 134

5.24 Dimensionless Front Speed vs. Dimensionless Distance From Entrance..... 138

5.25 Local Densimetric Froude Number vs. Local Neck Reynolds Number..... 140

5.26 Dimensionless Front Position vs. Dimensionless Elapsed Time..... 142

5.27 Dimensionless Excess Density at Front Head vs. Dimensionless Distance From Entrance..... 144

5.28 (a) Dimensionless Mean Concentration Below Interface vs. Distance From Entrance for Kaolinite Tests.... 145

(b) Dimensionless Mean Concentration Below Interface vs. Distance From Entrance for Flyash Tests..... 146

5.29 (a) Dimensionless Settling Velocity vs. Dimensionless Distance From Entrance for Cohesive Sediments..... 149

(b) Dimensionless Settling Velocity vs. Dimensionless Distance From Entrance for Cohesionless Sediments. 150

5.30 Dimensionless Median Dispersed Particle Size of Deposit vs. Dimensionless Distance From Entrance..... 152

5.31 Settling Velocity and Median Dispersed Particle Size vs. Main Channel Concentration..... 154

5.32 Flocculation Factor vs. Distance From Entrance..... 157

5.33 Flocculation Factor vs. Median Dispersed Particle Size..... 159

5.34 (a) Dimensionless Deposition Rate vs. Dimensionless Distance From Entrance for Cohesive Sediments..... 161

(b) Dimensionless Deposition Rate vs. Dimensionless Distance From Entrance for Cohesionless Sediments. 162

5.35 Mean Sediment Flux into the Side Channel Through Entrance vs. Mean Sediment Concentration at Entrance.. 164

5.36 Dimensionless Front Speed vs. Dimensionless Distance From Entrance for Tide Effect Tests..... 166

5.37 Dimensionless Front Position vs. Dimensionless Elapsed Time for Tide Effect Tests..... 169

5.38 Dimensionless Mean Concentration Below Interface vs. Dimensionless Distance From Entrance for Tide Effect Tests..... 171

A.1 Spatial Grid System for Numerical Modeling..... 187

B.1 (a) Dimensionless Vertical Velocity Profile at x = 1.8 m (Unsteady State)..... 199

(b) Dimensionless Vertical Velocity Profile at x = 4.D m (Unsteady State)..... 199

B.2 (a) Dimensionless Vertical Velocity Profile at x = 1.8 m (Steady State)..... 2DD

(b) Dimensionless Vertical Velocity Profile at x = 4.0 m (Steady State)..... 200

LIST OF SYMBOLS

A	A positive coefficient in linear parabolic equation
a_o	Amplitude of tide
B	Width of closed-end channel
C	Suspended sediment concentration
C'	Mean concentration at front head
C_o	Concentration in main channel
$\overline{C}_o$	Depth-mean concentration in main channel
C_1	Concentration just inside closed-end channel entrance
$\overline{C}_1$	Depth-mean concentration just inside closed-end channel entrance
$\overline{C}_b$	Depth-mean concentration below zero-velocity interface
$\overline{C}_{b1}$	Depth-mean concentration below zero-velocity interface just inside closed-end channel entrance
C_D	Drag coefficient
C_p	Constant in the expression of initial front speed (eq.2.1)
^oC	Degree Celsius
d	Sediment deposition rate
d_m	Median dispersed particle size
d_{m1}	Median dispersed particle size of deposit just inside closed-end channel entrance
d_{85}	Eighty-five percent finer than particle size
e	Base of natural logarithm
e_x	Horizontal momentum diffusion coefficient
e_z	Vertical momentum diffusion coefficient in stratified flows
e_o	Vertical momentum diffusion coefficient in homogeneous flows

f	A continuous function
f_o	Friction factor
F	Flocculation factor
F_1	Hydrostatic force acting on the cross section of closed-end channel entrance
F_2	Hydrostatic force acting on the cross section of stationary sediment wedge toe
F_i	Component force
F_k	Complex fourier coefficient of function f
Fr_Δ	Densimetric Froude number
g	Acceleration due to gravity
G_s	Specific gravity of sediment particles
h	Total water depth in closed-end channel
H	Total water depth in main channel
h_1	Height of front nose
h_2	Height of front head
h_3	Height of front neck
ΔH	Water surface elevation difference with reference to H
ΔH_{max}	Maximum ΔH in closed-end channel
i	Column number in spatial grid system for numerical simulation
j	Layer number in spatial grid system for numerical simulation
k	Component in complex Fourier series
k_1	Coefficient of settling velocity expression (eq.2.4)
k_2	Coefficient of settling velocity expression (eq.2.5)
k_3	Coefficient of deposition rate expression (eq.2.7)
L	Length of closed-end channel
L'	Wave length of tide in shallow water, $(gH)^{1/2}T$
m	Deposited (dry) mass per unit bed area

m_f	Mass of turbidity front
M	Total dry mass of sediment deposited in closed-end channel during test
M_a	Total mass of water-sediment mixture
M_D	Mass deposited in closed-end channel due to turbidity current over a tidal period
M_s	Total mass of sediment
M_T	Mass deposited in closed-end channel due to tidal motion over a a tidal period
M_w	Total mass of fresh water
n	Manning's roughness coefficient; also, time step number of numerical simulation
N	Top layer in spatial grid system for numerical simulation
n_1	Exponent of settling velocity expression (eq.2.4)
n_2	Exponent of settling velocity expression (eq.2.5)
p	Pressure force
q_1	Constant in vertical momentum diffusion coefficient expression (eq.3.36)
q_2	Constant in vertical mass diffusion coefficient expression (eq.3.37)
Q_1	Discharge of water-sediment mixture in upper layer at closed-end channel entrance
Q_2	Discharge of water-sediment mixture in lower layer at closed-end channel entrance
r	Sediment erosion rate
R	Hydraulic radius
Re	Reynolds number
Re_Δ	Densimetric Reynolds number
Re_h	Head Reynolds number
Re_n	Neck Reynolds number
R_i	Gradient Richardson number

R_k	Amplification factor
S	Mean net sediment flux into closed-end channel through entrance
S'	Stagnation point at front nose
s_o	Water surface slope
t	Time
T	Tidal period
Δt	Time step in numerical simulation
u	Horizontal velocity
u_o	Horizontal velocity in main channel
u_1	Horizontal velocity at closed-end channel entrance
$\bar{u}_o$	Depth-mean velocity in main channel
$\bar{u}_1$	Depth-mean velocity above zero-velocity interface at closed-end channel entrance
$\bar{u}_2$	Depth-mean velocity below zero-velocity interface at closed-end channel entrance
u_3	Depth-mean velocity at front neck
u_b	Horizontal velocity of bottom layer
u_f	Instantaneous front speed
u_{f1}	Initial front speed
$\bar{u}_{f1}$	Initial front speed as mean of local speeds between $x = 0.4$-2.0 m
u_j	Horizontal velocity at the j th layer
u_N	Horizontal velocity at the top layer
u_Δ	Densimetric velocity
u_r	Flow velocity of river opposing the advancing saline wedge
u_s	Horizontal velocity at water surface
u_T	Horizontal velocity at the top of a layer
V_o	Total volume of water-sediment mixture

$\forall_s$	Volume of sediment occupied
w	Vertical velocity
w_b	Vertical velocity at the bottom of a layer
w_N	Vertical velocity at the bottom of the top layer
w_s	Particle settling velocity; also, computed (floc) settling velocity
w_{so}	Reference settling velocity
w_{s1}	Particle settling velocity inside entrance of closed-end channel
w_{sd}	Stokes settling velocity of solid spherical particle with diameter equal to d_m
w_{sm}	Median quiescent column settling velocity
w_T	Vertical velocity at the top of a layer
x	Horizontal position coordinate along longitudinal axis of closed-end channel
x_f	Instantaneous position of front head along closed-end channel
x_o	Lock length in lock exchange flow
Δx	Longitudinal grid size in numerical simulation
z	Vertical elevation coordinate
Δz	Vertical grid size in numerical simulation
Δz_b	Thickness of the bottom layer
Δz_j	Thickness of the j th layer
Δz_N	Thickness of the top layer
α	Constant in sediment flux formula (eq.3.61)
α_1	Coefficient in vertical momentum diffusion coefficient expression (eq.3.36)
α_2	Coefficient in vertical mass diffusion coefficient expression (eq.3.37)
β	Constant in the expression for mean concentration below interface (eq.3.52)

β_1	Coefficient used to express longitudinal distribution of settling velocity
β_2	Coefficient used to express longitudinal distribution of horizontal velocity
γ	parameter used in eq.5.1
Ω	Constant in tide-induced deposition formula (eq.3.66)
δ	Deposition rate (dry sediment mass deposited per unit bed area per unit time)
δ_1	Deposition rate inside closed-end channel entrance
η	Height of interface (zero-velocity elevation)
π	Pi term notation used in dimensional analysis
ρ	Density
ρ_1	Density of sediment-laden water just inside closed-end channel entrance
$\bar{\rho}_1$	Depth-mean density just inside closed-end channel entrance
ρ'	Density in front head
ρ_b	Density at the bottom layer
ρ_h	Density at water surface
ρ_m	Mean density between turbid lower layer and clear upper layer in closed-end channel
ρ_N	Density at the top layer
ρ_s	Density of sediment particles
ρ_w	Density of water
ρ_η	Density at interface
$\bar{\rho}_{1L}$	Depth-mean density in the lower layer at channel entrance
$\bar{\rho}_{1U}$	Depth-mean density in the upper layer at channel entrance
$\Delta\rho$	Density difference
$\Delta\rho_o$	Density difference between sediment-laden water and fresh water in main channel

$\Delta\rho_1$	Density difference between sediment-laden water and fresh water just inside closed-end channel entrance
$\Delta\rho'$	Local density difference, based on concentration in front head
$\Delta\rho_d$	Local density difference, based on concentration in front head at x= 2.1 m
ν	Kinematic viscosity of water
ν_1	Kinematic viscosity of suspension
ζ	Ratio of vertical elevation to total water depth (z/h)
ξ	Ratio of interface elevation to total water depth (η/h)
τ_b	Bed shear stress; also, shear stress at the bottom of a layer
τ_{cd}	Critical deposition shear stress
τ_T	Shear stress at the top of a layer
ε_x	Horizontal mass diffusion coefficient
ε_o	Vertical mass diffusion coefficient in homogeneous flows
ε_z	Vertical mass diffusion coefficient in stratified flows
θ_i	Parameters used in the derivation of horizontal velocity, i = 1-5
λ	Spatial interval of periodicity in complex Fourier series

Abstract of Dissertation presented to the Graduate School of the University of Florida in Partial Fulfillment of the Requirements for the Degree of Doctor of Philosophy

TURBIDITY CURRENTS AND SEDIMENTATION IN CLOSED-END CHANNELS

By

CHUNG-PO LIN

May, 1987

Chairman: Dr. Ashish J. Mehta
Major Deparment: Civil Engineering

As a result of concern over sedimentation and water quality in closed-end channels such as docks, pier slips and residential canals, an investigation on the front behavior of turbidity currents and associated sedimentation in a closed-end channel was carried out. The focus of the present study was on the case of a closed-end channel of rectangular cross section and horizontal bed connected orthogonally to a main channel, where turbulent flow and high suspension concentration existed. Experiments were conducted in two specially designed flume systems to investigate front characteristics of turbidity currents, flow regime, and sediment deposition.

A group of dimensionless parameters for each physical aspect of concern derived from dimensional analysis provided the basis for selecting the measurement items in laboratory experiments and for presenting the results. A two-dimensional, explicit, coupled finite difference numerical model for simulating vertical flow circulation and sedimentation in a closed-end channel was made. In addition, analytic

cal developments for the longitudinal distribution of mean concentration below interface, flow field, the maximum rise of water surface, sediment flux through the entrance, and tide-induced deposition were also attempted.

No significant differences were found between the front shapes of turbidity currents and non-settling gravity currents. The rate of the decrease of front speed of turbidity currents with distance was faster than that of non-settling gravity currents. Characteristics which showed an exponential-type decrease with distance in the closed-end channel include front speed, mean concentration below interface, front concentration, settling velocity of suspension, dispersed particle size of deposit, and deposition rate. The relative settling velocity, i.e. the ratio of particle settling velocity to the densimetric velocity, was found to be the best parameter to interpret the differences between tests. Durations of front propagation in the initial adjustment phase, inertial self-similar phase, and viscous self-similar phase were found to be mainly dependent on sediment type and the relative settling velocity. A relationship for predicting the sediment flux into a closed-end channel through entrance was found. According to the relationship, the sediment flux is proportional to $H^{1/2}$ and $\bar{C}_1^{3/2}$, where H is the total water depth and $\bar{C}_1$ is the depth-mean concentration at the entrance of the closed-end channel. It was shown that the numerical model could simulate the suspension concentration distribution in the channel satisfactorily.

CHAPTER 1
INTRODUCTION

1.1 Turbidity Currents and Sedimentation in a Closed-End Channel

Sedimentation problems in pier slips, tidal docks, and closed-end channels have been mentioned by many investigators (e.g., Simmons, 1966; O'Dell, 1969; Wanless, 1975; Hoffman, 1982). In order to maintain the required depth of navigation in these shoaled channels, frequent costly dredging becomes inevitable. Recently, increases in dredging costs and the problem of dredged spoil disposal have motivated the search for other methods of sediment control (Hoffman, 1982; Bailard et al., 1985). Because of the complexity and variety of the factors involved in the shoaling processes at each shoaled area, thus far no efficient and standard method of sedimentation control is available. In fact, the prevention of sedimentation at a particular site must be based on a knowledge of the local dominant forces and associated mechanisms.

The main causative factors of the sedimentation problem, for example, in coastal closed-end residential canals of southwest Florida, suggested by van de Kreeke et al. (1977), are density and wind-induced flows. In tidal docks on the Mersey Estuary, England, investigated by Halliwell and O'Dell (1970), tidal flows and density currents are the primary causes of sedimentation. Accordingly, tide, wind, and density currents are the most likely physical factors involved in shoaling

processes in areas such as pier slips, tidal docks, and closed-end channels. Density currents include currents induced by salinity, temperature, and turbidity gradients. There is a large body of papers describing mechanisms related to tide- and wind-driven circulation as well as salinity- and thermally-induced density currents in bays and estuaries. However, less consideration seems to be given the mechanism of turbidity-induced density currents (turbidity currents) in shallow water environments. In some areas with high suspended sediment concentrations, turbidity currents may play an important role in the sedimentation problems of channels.

Inside a closed-end channel, suspended sediments tend to settle onto the channel bottom because of the quiescent conditions. Subsequently, the suspension concentration inside the channel will become lower than that of the outside water body. Consequently, a turbidity gradient between outside waters and inside waters appears, resulting in the intrusion of a turbidity current into the channel along the bottom. During the penetration of the turbidity current, the clear water overlying the layer of turbid water is forced to flow out of the channel due to the water surface gradient generated by the intrusion of denser fluid. In essence, therefore, a vertical circulation of fluid is set up. Such a circulation pattern can provide exchange between outside and inside waters, and may affect the water quality in the channel.

One significant feature of the turbidity current is that the density current caused by sediment in suspension itself tends to keep sediment in suspension (Bagnold, 1962). The type of turbidity current

--depositing, eroding, or autosuspension (neither deposting nor eroding) -- depends on the properties of suspended sediment, the front speed of the turbidity current, and the period of consolidation of the bed material (Pallesen, 1983). In the present study, the turbidity currents considered are depositing currents, which carry suspended sediments from the outside area into the closed-end channel and deposit them on the channel bed.

In this study, turbidity currents and associated sedimentation in closed-end laboratory flumes were investigated. Prior to the start of a test, steady flow and sediment concentration were established in the main channel with the entrance gate closed, separating the quiescent clear water in the closed-end channel from turbid water in the main channel. The gate was lifted; then measurements were made as the intrusion turbidity front propagated. Characteristics of resulting deposits were determined subsequently. A schematic diagram showing the geometry of the laboratory flume and an intruding turbidity front in the closed-end channel is shown in Fig. 1.1(a) and (b). The gyre zone shown in the figure indicates a circulation cell developed just inside the entrance. This circulation was induced by the lateral shear force exerted by the main flow at the flow boundary near the entrance. This gyre zone was relatively short in longitudinal extent. The suspended sediment was fairly well mixed vertically in the gyre. Beyond the gyre, the turbidity front was stratified. Definitions of the other terms indicated in the figures are given in section 2.1. It suffices to note here that the major influencing parameters are the sediment properties, channel geometry, and suspension concentration at the

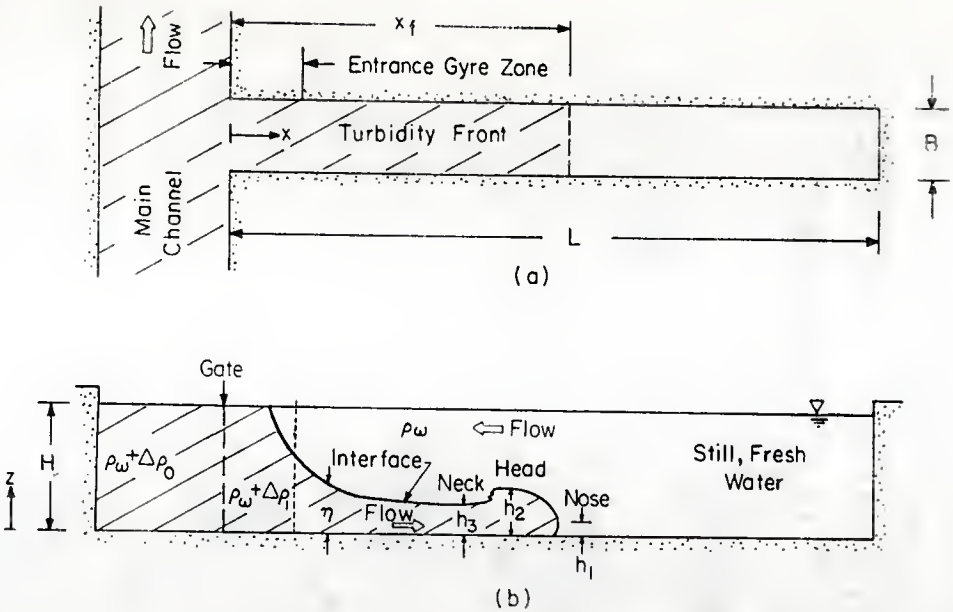

Figure 1.1 Schematic of Closed-End Channel and Turbidity Current. (a) Plan View. (b) Elevation View.

entrance of the closed-end channel, which is connected to a main flow channel.

1.2 Approach to the Problem

In order to study the front behavior of the turbidity current and the associated sedimentation in a closed-end channel, dimensional analysis was first carried out to relate the phenomena of interest to their influencing dimensionless parameters. Next, physical and mathematical models were developeded to investigate the general characteristics of the problems of concern. An attempt was made to solve the equations of convective-diffusion and momentum for concentration distribution and flow regime in the channel under a steady state condition.

Dimensional analysis of several important aspects of this investigation was carried out using the Buckingham - π theorem which provided a group of dimensionless parameters. These dimensionless parameters can aid understanding of the phenomena of concern in a physical sense, to reduce the number of measurement items in laboratory experiments, and to express the investigation results in a compact format.

The study of the problem by physical model includes two sets of laboratory experiments, which were conducted in two different-sized flume systems. Each measurement taken in the flume tests and the presentation of the results were based on the dimensionless parameters obtained from the dimensional analyses mentioned above. Two types of fine-grained sediments, cohesive and cohesionless, were used. The settling velocities and median particle sizes of these sediments were determined by settling column analysis (McLaughlin, 1959) and hydro-

meter or pipette analysis (ASTM, 1983; Guy, 1975). Owing to the complexity involved in scaling the properties of fine-grained sediment and internal density conditions, no presently-known model technique can reproduce the field phenomena in the small-scale models (Tesaker, 1975). Therefore, the results of this flume study are regarded as indicative of a qualitative approach to the prototype scale problem.

A two-dimensional (x and z directions), explicit, finite difference mathematical numerical model was developed. In the model, the coupled momentum and convective-diffusion equations govern the movement of water and suspended sediments. A common procedure used for simulating tide- and wind-induced sediment transport in estuaries by a numerical model is to solve the flow field directly from the momentum equation, then the transport of suspended sediment can be obtained by solving the convective-diffusion equation with the known flow field. In the present study, since the motivating force in the momentum equation is the density gradient resulting from suspended sediment concentration, the flow regime and the distribution of suspended sediment closely affect each other. Hence the two governing equations must be coupled and solved simultaneously. The four coefficients -- longitudinal and vertical momentum diffusion coefficients, and longitudinal and vertical mass diffusion coefficients -- were calibrated until the model's predictions showed a reasonable agreement with the measured data from a selected laboratory test. With the chosen coefficients, the model's predictions of sediment distribution and deposition rate were compared with the corresponding experimental results for other tests.

Five physical aspects of concern in the closed-end channel at the steady state condition are discussed in the analytical development section. They include 1) the longitudinal variation of mean suspension concentration below the interface; 2) the flow regime in the channel; 3) sediment flux into the channel; 4) the maximum rise of water surface in the channel; and 5) the tide-induced to turbidity current-induced deposition ratio. The longitudinal variation of mean concentration below the interface is obtained by solving the vertically-integrated form of the convective-diffusion equation at steady state. Based on this result, the steady state equation of motion is solved for the flow field inside the closed-end channel. The formula for predicting the sediment flux into the channel through the entrance is obtained as a product of the mean velocity and suspension concentration below the interface at the channel entrance; furthermore, the mean velocity is related to the densimetric velocity, which is the characteristic velocity induced by density differences (Keulegan, 1957).

A stationary sediment wedge can be established by a force balance between the force induced by the dense fluid at the entrance of the closed-end channel and the hydrostatic pressure of clear water with an elevated water surface in the region beyond the toe of the stationary sediment wedge. A formula for predicting the magnitude of the rise of water surface needed for the establishment of a stationary sediment wedge in the closed-end channel is derived based on the conservation of momentum.

The ratio of tide-induced deposition to turbidity current-induced deposition in the closed-end channel can be computed based on the

concept of tidal prism and the sediment flux of turbidity current mentioned above.

1.3 Scope of Investigation

Three major foci of this study were 1) front behavior of the turbidity current, 2) mechanics of a stationary sediment wedge, 3) turbidity-induced sedimentation.

Front behavior of turbidity currents (which play a significant role in sediment transport) was examined primarily by laboratory flume tests. The investigation included initial front speed, characteristics of front propagation, and front shape. Results are compared with the corresponding front behavior of salinity-induced density currents reported in previous studies.

For the stationary sediment wedge, the longitudinal variation of mean concentration (mean sediment concentration in the layer below the interface) along the closed-end channel was investigated experimentally and analytically. The flow pattern in the channel was analytically derived from the equation of motion. In addition, formulas for predicting sediment flux into the closed-end channel and for computing the magnitude of the water surface rise in the region beyond the toe of sediment wedge were derived, and the predictions were compared with experimental data.

Characteristics of turbidity-induced sedimentation in a closed-end channel were investigated experimentally and by means of the numerical model. Herein, the longitudinal variations of the deposition rate, median dispersed particle size and settling velocity of deposits along the flume are presented and discussed in Chapter 5.

A number of publications are reviewed in Chapter 2. These papers describe the front behavior of density currents (most are salinity-induced density currents), the steady-state sediment wedge in a closed-end channel, mathematical models for estuarial sediment transport, and the depositional behavior of cohesive sediments.

Chapter 3 presents and discusses a dimensional analysis for several subjects of concern in the present study. Finite difference formulations of the coupled governing equation in the mathematical model are developed and the stability conditions of the numerical scheme are examined. Analytical solutions for mean sediment concentration below interface and water velocity at steady state are obtained from the equations of convective-diffusion and momentum. In addition, the solutions for sediment flux into the closed-end channel, the rise of water surface in the closed-end channel at steady state, and tide-induced to turbidity current-induced deposition ratio are presented.

In Chapter 4, the set-up, equipment, test materials, and procedure of two sets of laboratory experiments are described. The first set was performed in a 9.1 m long flume at the U. S. Army Corps of Engineers Waterways Experiment Station (WES), Vicksburg, Mississippi; the second set was conducted in a 14.7 m long flume at the Coastal Engineering Laboratory (COEL) of the University of Florida.

Chapter 5 shows typical experimental observations of a selected laboratory test. It also includes the comparison between experimental results and the corresponding predictions obtained by the calibrated numerical model and/or analytical approach. Subsequently, characteris-

tic results, which include the data of all experimental tests, are presented mostly in a dimensionless format. Some of the characteristic results are compared with the corresponding results reported by previous studies and/or from the present analytical approach. In addition, the results of two tidal effect tests, (one for "flood tide," one for "ebb tide"), and a reference test are discussed.

In Chapter 6, a summary of this study, conclusions, and recommendations for future work are presented.

In Appendix A, the spatial grid system, flow chart, and stability condition for the mathematical modeling are presented. Appendix B includes the derivations for the relationship between suspension concentration and density of water-sediment mixture, and the flow regime in the closed-end channel at steady state. In Appendix C, a computation of the maximum water surface rise in the closed-end channel at steady state for a select laboratory test is given. The characteristics of closed-end channel deposits are presented in Appendix D.

CHAPTER 2
LITERATURE REVIEW

2.1 Front Behavior of Turbidity Current

2.1.1 Classification

Gravity currents, sometimes called density currents, are formed by fluid flowing under the influence of gravity into another fluid of different density. Due to the greater weight of the denser fluid, a larger hydrostatic pressure exists inside the current than in the fluid ahead, which provides the motive force to drive the gravity current. Gravity currents occur in many natural and man-made situations, for example, a turbidity current resulting from a landslide at the sea bottom; oil spillage on the sea surface; spreading of warm water discharged from power plants into rivers; a cold air front confronted by a warm air front in the atmosphere; and accidental release of dense industrial gases. Because of the wide and frequent occurrence of gravity currents, investigations of the front behavior of such current have continued to the present time (O'Brien & Cherno, 1934; Von Kármán, 1940; Ippen & Harleman, 1952; Barr, 1963a, 1963b, 1967; Middleton, 1966a, 1966b, 1967; Benjamin, 1968; Simpson, 1982; Akiyama & Stefan, 1985). In these studies, the front shape, which indicates the coverage range of the current, and the front speed, which shows the spreading rate of the current, were of primary concern.

The gravity current is characterized by a "head wave" where the head height, h_2, is higher than neck height, h_3 (see Fig.1.1(b)). On the rearward side of the head wave there is a highly turbulent zone suggestive of wave-breaking and mixing. These features appear to be common to many physical phenomena that may be classfied as gravity currents.

2.1.2 Front Shape

Von Kármán (1940) investigated the front shape of the gravity current based on Stokes' deduction of the extreme sharp-crested shape of water waves, and concluded that the stagnation point, denoted as S' in Fig.2.1, lies on the no-slip bottom boundary, and a tangent line drawn from the point S' on the interface of the front has a slope of $\pi/3$. The same result was derived in Benjamin's (1968) extensive treatment which was based on inviscid fluid theory. However, from laboratory experiments, the stagnation point was observed to be elevated (Fig.2.2), unlike the analytical predictions by Von Kármán (1940) and Benjamin (1968).

From their laboratory experiments, Ippen and Harleman (1952), Keulegan (1958), and Middleton (1966) have suggested a universal dimensionless front shape profile which will approximately fit all gravity current heads of different sizes and velocities. In these profiles, estimates of the ratio of nose height to head height h_1/h_2, where h_1 is the nose height or the distance from the bottom to the point S', and h2 is the head height, shown in Fig.2.2, vary from 0.1 to 0.27. This result reveals that in real flows, because of friction resistance at the stationary boundary, the lowest streamline in the

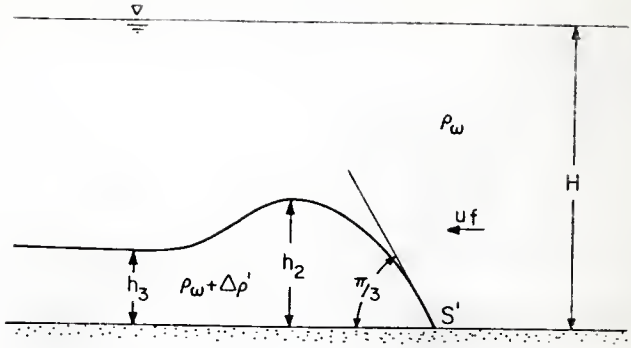

Figure 2.1. Front Shape of Gravity Current From Theoretical Model (after Von Kårmån, 1940).

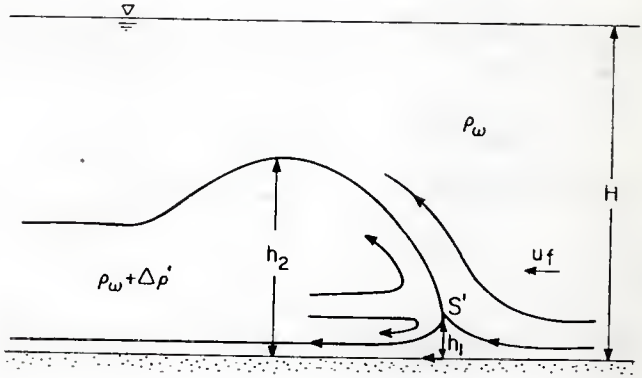

Figure 2.2 Schematic of Mean Flow Relative to a Gravity Current Head Subject to No-Slip Conditions at Its Lower Boundary (after Simpson, 1972).

flow relative to the head must be towards the rear, and the stagnation point S' then is raised some small distance above the floor (Fig.2.2).

Simpson (1972) further found that the ratio, h_1/h_2, where h_1 is the nose height, is not a universal constant, but is dependent on a local head Reynolds number, $Re_h = u_f h_2/\nu$, where u_f is the front speed of the gravity current and ν is the kinematic viscosity of water. Based on his experiments, he proposed a relationship between h_1/h_2 and Re_h, according to which h_1/h_2 decreases as Re_h increases. In Chapter 5, the trend between h_1/h_2 and Re_h, observed in the laboratory measurements of the present study, is compared with the results of previous investigations.

Another important aspect of front shape is the ratio of h_2/h_3, where, as noted, h_2 and h_3 are the heights of the head and the neck, respectively. An approximately constant value of 2.08 was obtained by Keulegan (1958) in the range of Re_n between 10^3 and 10^5, where $Re_n = u_f h_3/\nu$ designates the local neck Reynolds number, using the characteristic length, h_3. Simpson and Britter (1979) found empirically that the ratio h_2/h_3 is not a universal constant, but depends upon the fraction depth h_3/H, where H is the total water depth. A comparison between the variation of h_2/h_3 with Re_n, obtained from the present and previous investigations, is given in Chapter 5.

The existence of a "head wave" in the gravity current is due to the excess mass flux of the lower fluid brought forward to the head from the neck region and lifted upward within the head, then returned back toward the neck region by means of interface waves breaking just behind the head. In order to explore the intensity of mixing between

the two fluids at the head interface, which is related to the front head height, the ratio u_f/u_3, where u_3 is the depth-averaged velocity in the neck, was examined by Komar (1977). Based on his experimental results, Komar pointed out that u_f/u_3 is dependent on the densimetric Froude Number, $Fr_\Delta = u_f/[\Delta\rho gH/\rho_w]^{1/2}$, where ρ_w is the density of fresh water and g is the acceleration of gravity. Note that u_3 is greater than u_f. As the ratio u_f/u_3 becomes smaller with increasing Fr_Δ, the ratio h_2/h_3 will become larger (i.e. more intensive mixing between two fluids will take place). Since the rate of mixing at the head between the two fluids results from the excess mass flux into the head; therefore this rate can be computed as $(u_3 - u_f)h_3$.

2.1.3 Front Speed

The initial front speed, u_{f1}, in lock exchange flow of saline water has been investigated by, among others, O'Brien and Cherno (1934), Yih (1965) and Keulegan (1957). These investigations found that in a mutual intrusion between two liquids of a lock exchange flow, a stagnation point appears at the elevation of one-half of the total water depth at the cross section of the barrier (used to separate two fluids of different densities before the test). The initial front speed, u_{f1}, can be expressed as

$$u_{f1} = C_p \left[\frac{\Delta\rho}{\rho_m} gH \right]^{1/2} \qquad (2.1)$$

where C_p is a "universal" constant, and $\Delta\rho$ and ρ_m are the density difference and mean density between the two liquids, respectively. In eq.2.1 the square-root term was denoted as the densimetric velocity,

u_Δ, by Keulegan (1957):

$$u_\Delta = \left[\frac{\Delta\rho}{\rho_m} gH \right]^{1/2} \qquad (2.2)$$

The coefficient, C_p, in eq.2.1 was found to be 0.50 by Yih (1965) using an approach based on the conservation of energy, and 0.46 from the laboratory experiments conducted by Yih (1965) and Keulegan (1957). Initial front speeds were examined in laboratory experiments of the present study, and the results are compared in Chapter 5 with those obtained by Keulegan (1957).

Benjamin (1968) pointed out that the initial front speed which occurs after removing the barrier in lock exchange flow will remain unchanged over a distance, during which the gravity current propagates without energy losses. After the front propagates beyond a certain distance, energy conservation no longer holds, because of interfacial as well as bottom friction. During energy dissipation, a "head wave" at the front is formed, and both front speed and head height decrease. A dimensionless factor, $Fr_\Delta = u_f/[\Delta\rho' g h_3/\rho_w]^{1/2}$, termed the <u>local</u> densimetric Froude number, is used to express the relationship between the front speed, u_f, and local densimetric velocity, where $\Delta\rho'$ is the local density difference between the liquid in the front head and the liquid ahead. Keulegan (1958) found that Fr_Δ is independent of the local neck Reynolds number $u_f h_3/\nu$ when the number is greater than 400, but is a function of $u_f h_3/\nu$ when $u_f h_3/\nu < 400$. A similar conclusion that the dimensionless front speed is strongly dependent on the densimetric Reynolds number, $Re_\Delta = u_\Delta H/\nu$, as $Re_\Delta <$ order(10^3), and Reynolds number-independent as $Re_\Delta >$ order(10^3) was made by Barr (1967)

based on a large-scale flume study. In the present investigation, values of Fr_Δ were computed from measured data in the range of $324 < Re_\Delta < 3{,}830$ and are compared in Chapter 5 with those obtained by Keulegan (1958).

A series of recent studies on the front propagation of salinity-induced gravity currents in lock exchange flow have been carried out by Huppert and Simpson (1980), Didden and Maxworthy (1982), Huppert (1982), and Rottman and Simpson (1983). According to their studies, there are three distinct phases which may exist during front propagation along the flume. In each phase the front movement is controlled by different combinations of dominant forces and can be characterized by a specific function of the elapsed time t. In the first phase (initial adjustment phase), during which the initial conditions are important, the front position, x_f, changes in linear proportion to the elaped time, t. This was empirically and numerically verified by Rottman and Simpson (1983). The second phase is the inertial self-similar phase, during which the gravity force (or buoyancy force) is balanced by the inertia force. That x_f moves as $t^{2/3}$ was theoretically derived by Huppert and Simpson (1980), and was experimentally and numerically confirmed by Rottman and Simpson (1983). At the stage when the viscous force becomes more important than the inertia force, a viscous self-similar phase is reached. In this third phase the force balance is governed by gravity and viscous forces. That x_f moves as $t^{1/5}$ was obtained by Didden and Maxworthy (1982) by estimating the order of magnitude of forces involved. Also, Huppert (1982) found the same characteristic relationship between x_f and t for the viscous

self-similar phase after studying the viscous gravity current using a lubrication theory approximation. Within the first two phases (when the Reynolds number of the gravity current is high), the front movement is locally controlled by the conditions at the front. In the viscous phase (low Reynolds number gravity current), the front shape and front speed are independent of the conditions at the front. A figure (Fig.2.3) given by Rottman and Simpson (1983) clearly illustrats the existence of these three distinct phases as the salinity front propagated along a flume. In the figure, x_0 is the lock length, and t_0 is a characteristic time parameter. Evidence of these three phases was found from the laboratory measurements in the present study, and a discussion in detail is given in Chapter 5.

The effect of the internal stratification in the gravity current front on the front movement was of particular interest for this study because a strong stratification in the turbidity front can exist due to the settling of suspended sediment. Stratification considerably reduces front speed, according to the findings of Kao (1977).

2.2 Stationary Sediment Wedge

If the leading wedge (toe) of the turbidity current has propagated to the point where all suspended sediment at the front head has deposited, a steady or quasi-steady state sediment wedge can be established in a closed-end channel where the force balance is achieved by a raising of the water level in the region beyond the toe. McDowell (1971) mentioned that such a stationary sediment wedge may exist in an enclosed, quiescent basin connected to open water. He proposed a simple means of determining the sediment flux from outside waters into

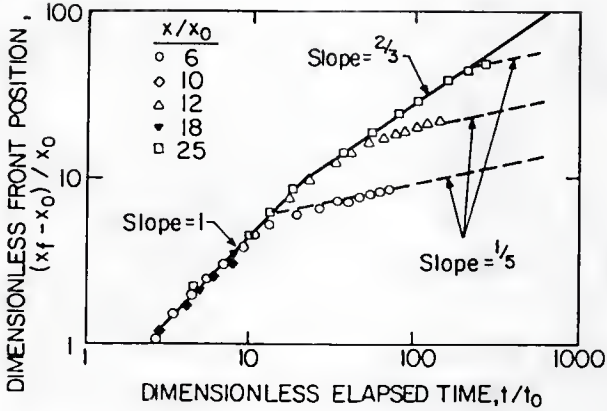

Figure 2.3. The Front Position as a Function of Time for Different Releases (after Rottman & Simpson, 1983)

the basin, as the product of the mean settling velocity of particles and the arrested wedge length. In addition, based on analytical considerations, he found that for the case of particles with small settling velocity and high suspension concentration, inflow velocity in the lower layer would be approximately equal to $0.71u_{\Delta}$, where u_{Δ} is the densimetric velocity. Yet, no evidence was provided to verify his findings.

Gole et al. (1973) conducted an experimental investigation of a stationary sediment wedge in a two-dimensional (i.e relatively narrow) closed-end channel by permitting the denser silt-laden saline water to intrude into silt-free saline water. Under the equilibrium condition, the surface outflow velocity of silt-free water at the entrance of the channel was measured and found to be approximately $0.35u_{\Delta}$, which is only one-half of McDowell's (1971) finding. Based on the volumetric conservation of water, the magnitudes of volume flux in lower and upper layers should be identical. Accordingly, if the zero-velocity interface (stagnation point) occurs at the mid-depth, it can be assumed that the depth-averaged velocities in both layers at the channel entrance are equal. Once the inflow velocity is known, then the sediment flux into the channel can easily be computed based on the inflow velocity, inflow depth, and sediment concentration at the entrance.

One of the objectives in the present study was to find out the longitudinal suspended sediment distribution, sediment flux into the closed-end channel, and the flow regime in a stationary sediment wedge by means of experimental, analytical, and/or mathematical model approaches. The results are discussed in Chapter 5.

2.3 Mathematical Model

Fischer (1976) attempted to simulate density currents in estuaries by a numerical model and found that numerical instability or large numerical errors which occur in solving the convective-diffusion equation will be encountered if a common numerical method (e.g. leapfrog method) is used to solve the eqution for the density current with a fairly sharp density discontinity (i.e. at the density front). A higher-order difference approximation, Hermite interpolation function, was suggested by Fischer to be used to formulate the convective-diffusion equation. A conclusion resulting from comparing the solutions obtained by a semi-analytical method, the higher-order Hermite approximation, and other methods, is that the numerical errors were considerably reduced by using the higher-order Hermite function approximation.

Miles (1977) developed a multi-layered, one-dimensional model to study the detailed vertical structure of the flow and salinity distributions in estuaries. Non-uniform layer thicknesses can be deployed over the water depth to give thinner layers at the locations where vertical velocity or salinity varies rapidly. In the equations of motion and convective-diffusion equation, a mixing length turbulence model was adopted to express the vertical momentum and mass transfer in the stratified flow with stratified buoyancy effects. A semi-implicit numerical scheme was used to formulate the governing equations in which explicit finite differences for the convective terms and implicit finite differences for the remaining terms were used in the equations. Subsequently, the double sweep method (Abbott, 1979) was applied to

solve the finite difference formulations with known boundary conditions.

Perrels and Karelse (1981) developed a two-dimensional, laterally-averaged model to study salinity intrusion in estuaries. A finite difference method was selected, in combination with a coordinate transformation, for the numerical integration of the system of differential equations. An explicit technique was used in the longitudinal direction and an implicit technique in the vertical direction for both equations of momentum and convective-diffusion. For the continuity equation a central difference scheme was used. The calibration and verification of the model were carried out by comparing model results with experimental data obtained from laboratory flume tests.

One of the first mud transport models was developed by Odd and Owen (1972). It is a two-layered, one-dimensional coupled model which simulates both the tidal flow and mud transport in a well-mixed estuary. The two layers can be of unequal thickness, with uniform properties (e.g. flow velocity, suspension concentration) assumed for each layer. The equations of motion and continuity for each layer are solved using a finite-difference formulation, while the convective-diffusion equation governing the transport of suspended sediments in two layers is solved using the method of characteristics. Erosion and deposition are included in this model.

Ariathurai (1974) and Ariathurai and Krone (1976) developed an uncoupled two-dimensional, depth-averaged cohesive sediment transport model which used the finite element method to solve the convective-diffusion equation. The model simulates erosion, transport, and deposi-

tion of suspended cohesive sediments. Aggregation of cohesive sediment was accounted for by determining the sediment settling velocity as a function of the suspension concentration. Ariathurai et al. (1977) modified the model to solve the two-dimensional, laterally-averaged suspended sediment transport problem. The model was verified using field observations from the Savannah River Estuary. Required data for the model include the two-dimensional, laterally-averaged velocity field, diffusion coefficients, and sediment deposition and erosion properties.

Kuo et al. (1978) devloped a two-dimensional, laterally-averaged, coupled model which simulates the motion of water and suspended sediment near the turbidity maximum of an estuary. The vertical dimension was divided into a number of layers, and a finite difference method was used to solve the equations of motion, continuity and convective-diffusion for each layer. Stratification effects on the vertical momentum and mass diffusion coefficients were considered in this model. Furthermore, an empirical formula was used for the relationship between the vertical momentum or mass diffusion coefficient and the local Richardson number, suggested by Pritchard (1960). The longitudinal momentum and mass diffusion coefficients were obtained by multiplying a constant ($=10^5$) times the vertical momentum and mass diffusion coefficients, respectively. Erosion and deposition were accounted for in the convective-diffusion equation for the bottom layer.

2.4 Depositional Properties of Fine-Grained Sediments

Two different types of fine-grained sediments, cohesionless and cohesive sediments, were used in the present investigation of sedimentation in closed-end channels. Understanding the sedimentation characteristics in the channel requires knowledge pertaining to the settling characteristics of suspended sediment and the depositional properties of sediment. Several important depositional properties of fine-grained sediments are reviewed as follows.

2.4.1 Settling Velocity

For cohesionless fine sediments, the settling velocity can practically be assumed to be concentration-independent and can easily be determined by Stokes' formula (Daily & Harleman, 1966):

$$w_s = \frac{d_m^2 \, (G_s - 1) \, g}{18 \, \nu} \qquad (2.3)$$

where w_s is particle settling velocity, d_m is median grain size, and G_s is the specific gravity of sediment.

However, for cohesive sediments (particle sizes less than about 20 microns), the settling velocity is dependent on floc or particle size, suspension concentration, local physico-chemical conditions, and microbiological activity in the water or at the particle surface. Of these factors, the effect of suspension concentration on the settling velocity was found to be very significant due to the change of the frequency of inter-particle collision in suspension with changes in concentration. Collision, which influences the rate and degree of floc aggregation, is caused by Brownian motion, the presence of a velocity

gradient, and differential particle settling velocities (Hunt, 1980). Krone (1962) has discussed the effect on inter-particle collision in suspension by each mechanism. It was noted that when settling occurs under static or quiescent flow conditions, i.e. the conditions of the present study, Brownian motion and differential settling velocities mainly determine the frequency of collision and, consequently, the degree of aggregation.

Mehta (1986) summarized the relationship between settling velocity of cohesive sediment and initial suspension concentration in three different concentration ranges. At very low concentrations, the rate of aggregation is negligible, and the settling velocity, w_s, does not depend on the suspension concentration. At moderate concentrations, aggregation causes w_s to increase with concentration, and a relationship was found, from laboratory settling column analyses, of the form

$$w_s = k_1 C^{n_1} \qquad (2.4)$$

where k_1 depends on the sediment composition, while n_1 was theoretically and experimentally found to be equal to 1.33 by Krone (1962) for San Francisco Bay sediment, and to be less than unity by Teeter (1983) for Atchafalaya Bay sediment.

At high concentrations, w_s decreases with increasing concentration because w_s is hindered by the mutual interference of particles and by the upward flux of fluid escaping through the small spaces among the network of aggregates. Brownian motion becomes important under these conditions. The following relationship has been suggested by the work of Richardson and Zaki (1954) to be applicable in this range:

$$w_s = w_{s0} (1-k_2C)^{n_2} \qquad (2.5)$$

Where w_{s0} is a reference settling velocity, k_2 is a coefficient which depends on the sediment composition, and n_2 is a coefficient which has been analytically derived to be equal to 4.65 by Richardson and Zaki (1954) and was empirically found to be equal to 5.0 by Teeter (1983).

An example of the variation of the settling velocity, w_s, with concentration is shown in Fig.2.4, which is based on measurements in a settling column using mud in salt water from the Severn Estuary, England (Thorn, 1981).

Settling column tests for the settling velocities of the fine-grained sediments used in the present flume study were carried out at the Coastal Engineering Laboratory of the University of Florida. In these tests, the settling velocities of kaolinite were examined over the concentration range from 0.45 g/l to 10.0 g/l, and the results are presented in Chapter 4.

2.4.2 Deposition Rate

Krone (1962) and Mehta (1973) conducted laboratory deposition experiments in which they monitored the variation of suspension concentration with time under a given applied bed shear stress, τ_b. In several tests τ_b was selected to be smaller than the critical deposition shear stress, τ_{cd}, i.e. the shear stress below which all initially suspended sediment deposits eventually.

With reference to the time-concentration curves in Fig.2.5 (Mehta, 1973), the linear portions corresponding to the range of low concentra-

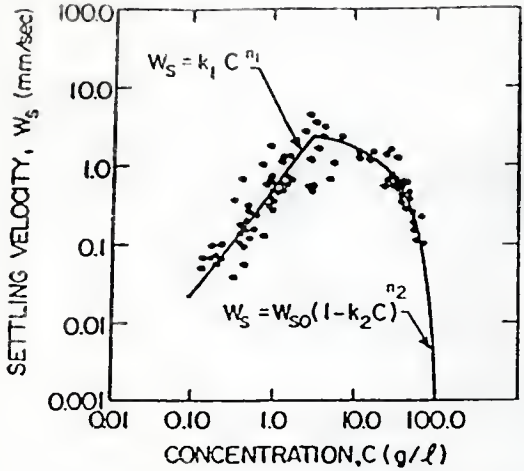

Figure 2.4. Median Settling Velocity vs. Concentration for Severn Estuary Mud (after Thorn, 1981).

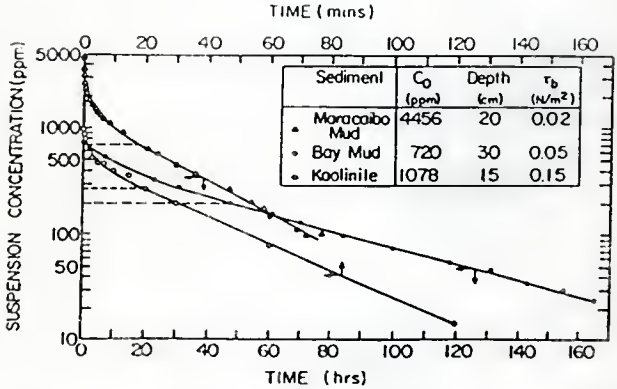

Figure 2.5. Suspended Sediment Concentration vs. Time for Three Cohesive Sediments (after Mehta, 1973).

tions, where aggregation is negligibly slow, leads to the relation

$$\frac{dm}{dt} = - w_s C \left(1 - \frac{\tau_b}{\tau_{cd}}\right) , \qquad \tau_b < \tau_{cd} \qquad (2.6)$$

where m is the mass of suspended sediment per unit bed area over the depth of flow. Eq.2.6 is a mass balance equation which essentially represents dilution of the suspension with time. Eq.2.6 can also be used to compute the deposition rate of suspended particles.

When aggregation is proceeding at a significant rate, as in the initial phase of the curves of Fig.2.5, the dilution rate of suspension has been described by Krone (1962) as

$$\frac{dm}{dt} = - \left[k_3 C \left(1 - \frac{\tau_b}{\tau_{cd}}\right)\right] \frac{1}{t} , \qquad \tau_b < \tau_{cd} \qquad (2.7)$$

where k_3 is a factor that must be determined empirically, and t is the time since the beginning of aggregation.

Mehta (1973) also carried out extensive deposition tests under steady flows using kaolinite as well as muds from San Francisco Bay and Maracaibo Estuary, Venezuela, and in addition reanalyzed some previous flume data. The critical deposition shear stress, τ_{cd}, was found to depend on the sediment composition, and varied from 0.04 to 0.15 N/m^2. Note that τ_{cd} of kaolinite was equal to 0.15 N/m^2, which will be referred to in comparison with τ_{cd} of kaolinite obtained from the laboratory measurements of the present study.

2.4.3 Sorting of Deposited Sediments

Dixit et al. (1982) analyzed a series of data from deposition experiments conducted by McAnally (Mehta et al. 1982) in a 100 m long

flume at the U.S. Army Corps of Engineers Waterway Experiment Station, Vicksburg, Mississippi. In one test, a kaolinite-water mixture was introduced from the headbay of the flume with an initial concentration on the order of 10 g/l. The depth of flow was 0.17 m, the bed shear stress was 0.11 N/m^2 and Manning's roughness coefficient was approximately 0.01. The test was run for one hour, and a smooth surface without any ripple-scaled bed features was found at the end of the test. The variation of median grain size, d_m, of the dispersed sediment from the deposit with distance from the flume headbay is shown as Fig.2.6(a). Comparing these values with d_m = 0.001 mm of the injected sediment, a sorting effect is evident. In Fig.2.6(b) the settling velocity of the same deposit computed from the mass balance equation is plotted against the distance from the headbay. Similar sorting trends of d_m and w_s with distance, x, were found from the deposits of the present laboratory experiments, and are presented in Chapter 5.

Furthermore, the flocculation factor, F, of cohesive sediment is defined as the ratio of the median settling velocity of the flocs to the settling velocity of the primary constitutive particles. According to the relationship between F and the median primary particle diameter, d_m, found by Migniot (1968) and confirmed by Dixit et al. (1982), the dependence of cohesive sediment aggregation on primary particle size can be demonstrated in a quantitative manner. A similar relationship between F and dm was found in the present study and is discussed in Chapter 5.

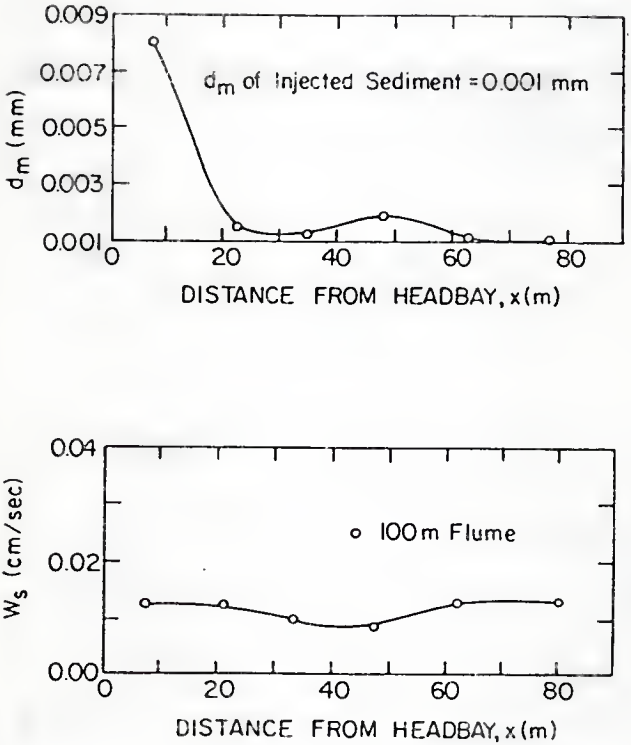

Figure 2.6. (a) Median Dispersed Grain Size vs. Distance; (b) Suspended Sediment Settling Velocity vs. Distance (after Dixit et al. 1982)

CHAPTER 3
METHODOLOGY

3.1 Dimensional Analysis

3.1.1 Front Shape

The height of front nose. The geometry of the experimental channel system is given in Fig.1.1 (a) and (b). The channel has the same cross section from the entrance to the closed end. The bottom of the channel system is in the same horizontal plane, and the water depths at main and closed-end channels are the same before removing the gate located at the connection between both channels. The suspended sediment source at the main channel remains constant. Here L, B, and H denote channel length, channel width, and water depth, respectively. Let ρ_w and ν be respectively the density and kinematic viscosity of fresh water, and $\rho_w + \Delta\rho$ and ν_1 be the corresponding quantities for the water-sediment mixture. Because the density and temperature variations occurring throughout a test were relatively small, the average value of the densities can be expressed as ρ_w, and of the kinematic viscosities as ν.

As mentioned in Chapter 2, the front shape of gravity currents has interested many investigators. During the present laboratory experiments, a typical front characteristic of turbidity current was observed and is shown in Fig.3.1. Let h_1 and h_2 be the heights of front nose and front head, respectively (Fig.2.2). Then an expression

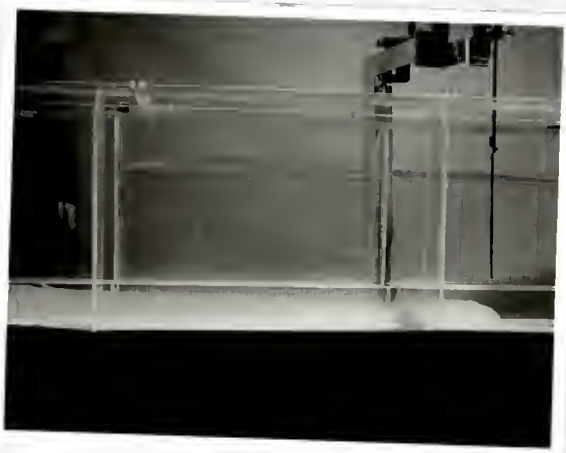

Figure 3.1. Front Shape of a Propagating Turbidity Current.

for h_1 is given as

$$h_1 = h_1 \ (h_2, H, u_f, \nu) \qquad (3.1)$$

where u_f is the front speed. An operation using Buckingham - π theorem (Streeter & Wylie, 1975) leads to the desired form:

$$\frac{h_1}{h_2} = f \left(\frac{u_f h_2}{\nu}, \frac{h_2}{H} \right) \qquad (3.2)$$

which shows that the ratio of nose height to head height may be dependent on the local head Reynolds number, $u_f h_2/\nu$, and fraction depth, h_2/H.

<u>The height of front head</u>. One significant feature of the front shape is that the height of the front head is larger than the height of front neck, and an intensive mixing takes place at the interface right behind the front head (Fig.2.2).

A series of photographs of the front shape taken in the present experiments indicated that the size of the advancing front and the degree of front mixing decrease as the front speed decreases. The front head completely disappears after the front travels for a relatively long distance. Let h_3 denote the height of front neck, then the expression of the height of the front head is

$$h_2 = h_2 \ (H, h_3, u_f, \nu, w_s, B) \qquad (3.3)$$

where w_s is the particle settling velocity at the front. It leads to the following expression:

$$\frac{h_2}{h_3} = f \left(\frac{u_f h_3}{\nu}, \frac{h_3}{H}, \frac{w_s}{u_f}, \frac{B}{H} \right) \qquad (3.4)$$

The quantity h_2/h_3 was found to be independent of B/H by Keulegan (1958), but dependent upon the fraction depth, h_3/H, by Simpson and Britter (1979). A final form of h_2/h_3 can be written

$$\frac{h_2}{h_3} = f\left(\frac{u_f h_3}{\nu}, \frac{h_3}{H}, \frac{w_s}{u_f} \right) \qquad (3.5)$$

which indicates that besides the fraction depth h_3/H, h_2/h_3 may be dependent on the local neck Reynolds number, $u_f h_3/\nu$, and the relative settling velocity of suspended sediment, w_s/u_f.

3.1.2 Front Speed

Initial front speed. Let u_{f1} denote the initial front speed of turbidity front, that is the velocity immediately after the gate is opened. Ideally the opening is very smooth and sudden. Within such a short time, the effect of the sediment settling velocity on the front movement is negligible. The expression of u_{f1} with the related geometrical and physical quantities is given as

$$u_{f1} = u_{f1}\ (\ g,\ \Delta\rho_1,\ \rho_w,\ \nu,\ H,\ B\ ) \qquad (3.6)$$

where $\Delta\rho_1$ is the density difference between the main channel and closed-end channel waters. One important velocity characteristic, densimetric velocity u_Δ, was introduced in eq.2.2. Another significant dimensionless parameter was noted as the densimetric Reynolds number, Re_Δ, by Keulegan (1957):

$$Re_\Delta = \frac{u_\Delta H}{\nu} \qquad (3.7)$$

A final form for eq. (3.6) is

$$\frac{u_{f1}}{u_\Delta} = f\left(\frac{u_\Delta H}{\nu}, \frac{B}{H}\right) \qquad (3.8)$$

which suggests that the dimensionless initial front velocity, u_{f1}/u_Δ, may depend upon the densimetric Reynolds number, $u_\Delta H/\nu$, and the width-to-depth ratio, B/H.

Instantaneous front speed. A major concern with front behavior of advancing turbidity current in the present study was how these physical parameters (e.g. channel geometry, boundary suspension concentration, and sediment properties) influence the front speed. It will be discussed in this section from two viewpoints; one is by relating the front speed to the channel geometry and suspension concentration at the entrance, and the other is by relating the front speed to the local front shape and suspension concentration at the front.

The front speed, u_f, and these possibly influencing parameters are grouped as follows:

$$u_f = u_f\,(x,\ H,\ B,\ g,\ \Delta\rho_1,\ \rho_w,\ \nu,\ w_s) \qquad (3.9)$$

This equation can be reduced to be in a final form

$$\frac{u_f}{u_\Delta} = f\left(\frac{x}{H}, \frac{B}{H}, \frac{u_\Delta H}{\nu}, \frac{w_s}{u_\Delta}\right) \qquad (3.10)$$

which shows that the dimensionless front speed may be a function of front position, width-to-depth ratio, densimetric Reynolds number, and

relative settling velocity. Eq.3.10 is similar to the dimensional analysis result of front speed of a saline wedge, which is advancing against the river flow, obtained by Keulegan (1971):

$$\frac{u_f}{u_\Delta} = f\left(\frac{x}{H}, \frac{B}{H}, \frac{u_\Delta H}{\nu}, \frac{u_r}{u_\Delta}\right) \qquad (3.11)$$

except for the term u_r/u_Δ, where u_r is the velocity of the river opposing the advancing wedge.

Barr (1967) investigated lock exchange flow of saline water in a large-scale flume (i.e. flume width, B, much greater than water depth, H), and found that the dimensionless front speed, u_f/u_Δ, is a function of the dimensionless distance, x/H, and the densimetric Reynolds number, Re_Δ:

$$\frac{u_f}{u_\Delta} = f\left(\frac{x}{H}, \frac{u_\Delta H}{\nu}\right) \qquad (3.12)$$

For a small-scale flume, it would be expected that u_f/u_Δ would also be a function of B/H. Therefore, the dimensionless grouping of instantaneous front speed for the lock exchange flow of saline water would be the same as eq.3.10 except for the relative settling velocity term, w_s/u_Δ.

It was noted in the experiments during the front propagating along the channel that whenever a decrease in the front speed was observed, a decrease in the front height was also observed. This suggested that possibly a relation between the front speed and the front height existed. The local density of the front, denoted as $\rho_w+\Delta\rho'$, decreases

by dropping a portion of suspended sediments to the bottom as it propagates downstream. Thus the effect of density decrease of the front on the instantaneous front speed must be taken into account. The expression of the front speed can be written as

$$u_f = u_f\ (\ h_3,\ g,\ \Delta\rho',\ \rho_w,\ \nu,\ w_s,\ H,\ B\ ) \qquad (\ 3.13\ )$$

here the neck height, h_3, is used as a height characteristic of the front. Equation 3.13 can be reduced to

$$Fr_\Delta = \frac{u_f}{[\Delta\rho' g h_3/\rho_w]^{1/2}} = f\ (\ \frac{u_f h_3}{\nu},\ \frac{w_s}{u_f},\ \frac{h_3}{H},\ \frac{B}{H}\ ) \qquad (\ 3.14\ )$$

where Fr_Δ designates local densimetric Froude number. Here, the parameter of w_s/u_f will introduce a stratification effect of suspension concentration at the front on the dimensionless front speed, as found by Kao (1977). Besides the internal stratification in the front, the local densimetric Froude number, Fr_Δ, may also be influenced by the local neck Reynolds number, $u_f h_3/\nu$, the fraction depth, h_3/H, and the width-to-depth ratio, B/H.

3.1.3 Front Position

The identification of three phases, each controlled by specific dominant forces, in the front propagation along a flume were mentioned in section 2.1.3. In each phase the front position, x_f, was found to be a specific function of the elapsed time, t. In the present study an attempt using dimensional analysis was made to provide the proper dimensionless forms of x_f and t for analyzing measured data and presenting the results. An expression of the front position may be

stated as

$$x_f = x_f\ (\ g,\ H,\ B,\ t,\ \Delta\rho_1,\ \rho_w,\ \nu,\ w_s\ ) \qquad (\ 3.15\ )$$

An operation using Buckingham - π theorem leads eq.3.15 to a final form with relevant dimensionless parameters:

$$\frac{x_f}{H} = f\ (\ \frac{B}{H},\ \frac{u_\Delta t}{H},\ \frac{w_s}{u_\Delta},\ \frac{u_\Delta H}{\nu}\ ) \qquad (\ 3.16\ )$$

which indicates that the dimensionless front position is dependent on the width-to-depth ratio, B/H , the relative settling velocity, w_s/u_Δ, the densimetric Reynolds number, $u_\Delta H/\nu$, and a dimensionless elapsed time, $u_\Delta t/H$.

Barr's (1967) study on the lock exchange flow of saline water in a large-scale flume provided a group of dimensionless influencing parameters for the dimensionless front position, x_f/H, i.e.

$$\frac{x_f}{H} = f\ (\ \frac{u_\Delta t}{H},\ \frac{u_\Delta H}{\nu}\ ) \qquad (\ 3.17\ )$$

Comparing eq.3.16 with eq.3.17, it can be seen that two additional dimensionless factors are included in eq.3.16. They are: 1) the width-to-depth ratio, B/H, which will introduce an effect on the front position x_f/H when the gravity current propagates in a small-scale flume, and 2) the relative settling velocity, w_s/u_Δ, which is a particular characteristic of turbidity currents.

3.1.4 Deposition Rate

One of the major concerns in the present study was the deposition of fine-grained sediments in a closed-end channel. The sediment

deposition rate in each subsection of the channel bed can be computed using the deposited sediment mass divided by the effective duration (i.e., the time elapsed from the passing of the turbidity front to the end of the test) and deposited area. The local deposition rate would be expected to vary with distance due to the distance variations of mean suspension concentration and of settling velocity of suspended sediment. The variation of deposition rate with distance and other relevant parameters are expressed as

$$\delta = \delta\ (\ x,\ H,\ w_s,\ g,\ B,\ \rho_w,\ \Delta\rho_1) \qquad (\ 3.18\ )$$

where δ is the local deposition rate. Eq.(3.18) can be further reduced to a desired form as

$$\frac{\delta}{\delta_1} = f\ (\ \frac{x}{H},\ \frac{B}{H},\ \frac{w_s}{u_\Delta},\ \frac{\Delta\rho_1}{\rho_w}) \qquad (\ 3.19\ )$$

where δ_1 is the deposition rate at the entrance of the closed-end channel. The normalized deposition rate, δ/δ_1, is thus observed to be a function of x/H and B/H. Also, that δ/δ_1 depends upon the relative settling velocity, w_s/u_Δ, is obvious. The influence of $\Delta\rho_1/\rho_w$ on δ/δ_1 can be made apparent by introducing different sizes of the flocculated particles through the entrance.

The dimensionless parameters obtained in eq.3.19 have also been used to examine the experimental results on the local sediment settling velocity, w_s, and the median dispersed particle size, d_m, since all data on δ, w_s, and dm were obtained by analyzing deposited samples from the flume tests.

3.2 Developement of Mathematical Model

3.2.1 Model Description

Basic governing equations. The mathematical model developed is a time varying, two-dimensional, coupled finite difference model that is capable of predicting the vertical and temporal variations in the suspension concentration of fine-grained sediments and in flow velocities in a coastal closed-end waterway with a horizontal bottom. In addition, it can be used to predict the steady-state or unsteady transport of any conservative substance or non-conservative constituent, if the reaction rates are known.

The governing equations, which control the flow regime and sediment transport, are expressed in conservation forms (Roache, 1972) and shown as

$$\frac{\partial u}{\partial x} + \frac{\partial w}{\partial z} = 0 \qquad (3.20)$$

$$\frac{\partial u}{\partial t} + \frac{\partial u^2}{\partial x} + \frac{\partial (uw)}{\partial z} = -\frac{1}{\rho}\frac{\partial p}{\partial x} + \frac{\partial}{\partial x}\left(e_x \frac{\partial u}{\partial x}\right) + \frac{\partial}{\partial z}\left(e_z \frac{\partial u}{\partial z}\right) \qquad (3.21)$$

$$0 = -g - \frac{1}{\rho}\frac{\partial p}{\partial z} \qquad (3.22)$$

$$\frac{\partial C}{\partial t} + \frac{\partial (uC)}{\partial x} + \frac{\partial}{\partial z}[(w-w_s)C] = \frac{\partial}{\partial x}\left(\varepsilon_x \frac{\partial C}{\partial x}\right) + \frac{\partial}{\partial z}\left(\varepsilon_z \frac{\partial C}{\partial z}\right) - d + r \qquad (3.23)$$

in which:

u, w = velocity components in the x and z directions, respectively

p = pressure force

e_x, e_z = momentum diffusion coefficients in the x and z directions, respectively

ε_x, ε_z = mass diffusion coefficients in the x and z directions, respectively

d = sediment deposition rate

r = sediment erosion rate

In fact, the physical quantities involved in these equations, such as u, w, p, and C, are time-averaged quantities over a period which is greater than the time scale of turbulence fluctuation when the flow is turbulent.

Equation 3.20 is the continuity equation for an incompressible fluid. Equation 3.21 is the equation of motion for an incompressible fluid, and represents the longitudinal momentum conservation of the flow. Equation 3.22 is the hydrostatic equation which results when the vertical components of the flow velocity and acceleration are smaller relative to the horizontal flow velocity and acceleration. Equation 3.23 is the convective-diffusion equation for suspended sediment, with resuspension and deposition as source and sink, respectively.

To obtain the time-varying solutions of the longitudinal and vertical velocity field, eq.3.21 must be solved with the continuity equation (eq.3.20). With the velocity field solved, it may be substituted into eq.3.23 to solve for the time-varying concentration field of suspended sediment.

Vertical integration of basic equations. Since the physical quantities in the channel can change rapidly over a short vertical distance, they require a grid size that is much smaller in the vertical direction than in the longitudinal direction. The fluid motion will be considered in horizontal slices with an exchange of mass and momentum between these slices. A so-called sparse grid system (Miles, 1977) in space used in the model and the location of physical quantities within the grid are shown in Fig.A.1 of Appendix A. At the top layer, the free surface is allowed to occupy any position within the layer, but the thicknesses of the others are fixed.

Integration over the height of the j th layer can be performed by assuming that all variables are practically constant through the depth of any layer, and that the fluxes of momentum and mass normal to the bottom of the channel and to the surface are zero.

Employing Leibnitz's rule for the vertical integration of equations 3.20, 3.21, and 3.23 over the j th layer and/or the surface layer, results in the following equations:

$$\frac{\partial h}{\partial t} = w_N - \frac{\partial}{\partial x}(u_N \Delta z_N) \qquad (3.24)$$

$$w_T = w_b - \frac{\partial}{\partial x}(u_j \Delta z_j) \qquad (3.25)$$

$$\frac{\partial u_j}{\partial t} + \frac{\partial}{\partial x}(u_j^2) + \frac{1}{\Delta z_j}(w_T u_T - w_b u_b) = -\frac{1}{\rho_j}\left(\frac{\partial p}{\partial x}\right)_j$$

$$+ \frac{\partial}{\partial x}\left(e_x \frac{\partial u}{\partial x}\right)_j + \frac{1}{\rho_j \Delta z_j}(\tau_T - \tau_b) \qquad (3.26)$$

$$\frac{\partial C_j}{\partial t} + \frac{\partial}{\partial x}(C_j u_j) + \frac{1}{\Delta z_j}[(w_T - w_s)C_T - (w_b - w_s)C_b]$$

$$= \frac{\partial}{\partial x}(\varepsilon_x \frac{\partial C}{\partial x})_j + \frac{1}{\Delta z_j}[(\varepsilon_z \frac{\partial C}{\partial z})_T - (\varepsilon_z \frac{\partial C}{\partial z})_b]$$

$$- \frac{d}{\Delta z_j} + \frac{r}{\Delta z_j} \qquad (3.27)$$

where:

u_j, Δz_j, ρ_j = longitudinal velocity, height, and density for the j th layer, respectively

u_T, w_T, τ_T = longitudinal velocity, vertical velocity, and shear stress at the top of a layer, respectively

u_b, w_b, τ_b = longitudinal velocity, vertical velocity, and shear stress at the bottom of a layer, respectively

u_N, w_N, Δz_N = longitudinal velocity, vertical velocity, and height for the top layer, respectively

h = water surface elevation.

Equations.3.24 and 3.25 are the continuity equations for the top layer and all other layers, respectively. Equation 3.26 is the longitudinal equation of momentum, and eq.3.27 is the convective-diffusion equation for suspended sediment.

Further derivation of the pressure term, $(1/\rho_j)(\partial P/\partial x)_j$ in eq.3.26 is necessary. The hydrostatic pressure at an elevation z in the fluid can be obtained from eq.3.22

$$p(z) = g \int_z^h \rho \, dz \qquad (3.28)$$

and its longitudinal gradient is

$$\frac{\partial p(z)}{\partial x} = \frac{\partial}{\partial x}\left(g \int_z^h \rho \, dz\right) = g \int_z^h \frac{\partial \rho}{\partial x} dz + g\rho_h \frac{\partial h}{\partial x} \qquad (3.29)$$

where ρ_h is the density at water surface.

The mean pressure gradient in the top layer can be derived thus

$$\left(\frac{\partial p}{\partial x}\right)_N = \frac{1}{\Delta z_N} \int_{h-\Delta z_N}^h \left(\frac{\partial p}{\partial x}\right) dz$$

$$= \frac{g}{\Delta z_N} \frac{\partial}{\partial x} \left[\int_{h-\Delta z_N}^h \left(\int_z^h \rho \, dz\right) dz \right]$$

$$= \frac{g}{2} \Delta z_N \frac{\partial \rho_N}{\partial x} + g\rho_N \frac{\partial h}{\partial x} \qquad (3.30)$$

where ρ_N is the average density in the top layer. For two adjacent layers, j and j+1, the relationship between the layer-averaged pressure gradients can be derived from eq.3.29, and the final expression is

$$\left(\frac{\partial p}{\partial x}\right)_j = \left(\frac{\partial p}{\partial x}\right)_{j+1} + \frac{g}{2}\left(\Delta z_{j+1} \frac{\partial \rho_{j+1}}{\partial x} + \Delta z_j \frac{\partial \rho_j}{\partial x}\right) \qquad (3.31)$$

where all of ρ_j, $(\partial p/\partial x)_j$, ρ_{j+1}, and $(\partial p/\partial x)_{j+1}$ are layer-averaged quantities. From eq.3.30 the mean pressure gradient at the top layer can be computed with a known mean density gradient at the same layer and the slope of water surface. Once the mean pressure gradient at the top layer is solved, the mean pressure gradient at the other layers can be calculated, based on eq.3.31.

Boundary conditions. At free surface boundary, no flow will occur across the free surface, and the vertical velocity on the water surface must be equal to zero. The shear stress induced by wind acting on the

water surface is not considered in this study; thus the shear stress at surface boundary can be regarded as zero. No mass flux of suspended sediment can flow through the free surface. This condition is expressed as

$$\varepsilon_z \frac{\partial C}{\partial z} = 0 \qquad \text{at } z = h \qquad (3.32)$$

At the bottom boundary, no flow can pass the bottom; therefore, the vertical velocity at the channel bed must be zero. The relationship between the friction factor, f_o, and Manning's roughness coefficient, n, can be obtained from the formulas of Manning and of Darcy-Weisbach (Daily & Harleman, 1966) as

$$f_o = \frac{8gn^2}{R^{1/3}} \qquad (3.33)$$

where R is hydraulic radius. Accordingly, the bottom shear stress, τ_b, can be expressed as

$$\tau_b = \frac{gn^2}{\Delta z_b} \rho_b \, u_b |u_b| \qquad (3.34)$$

where ρ_b, u_b, and Δz_b are the density, horizontal velocity, and thickness of the bottom layer, respectively. Like the free surface boundary, no mass flux of suspended sediment is allowed to pass through the bottom boundary, that is

$$\varepsilon_z \frac{\partial C}{\partial z} = 0 \qquad \text{at } z = 0 \qquad (3.35)$$

In addition, two boundary conditions at the entrance of the closed-end channel are necessary: 1) concentration profile of suspended sediment, and 2) the water surface elevation. The data from either condition can be time-varying quantities. To investigate the problem under tide effects, the surface elevation at the entrance of the closed-end channel can be specified with a periodic function including prototype tidal amplitude and period. The concentration profile of suspended sediment and water surface elevation involved in the present study did not vary with time. Also, the boundary conditions at the end of the closed-end channel include zero horizontal velocity and zero horizontal concentration gradient at the vertical wall.

Momentum and mass diffusion coefficients. In turbulent flow of a homogeneous fluid there are no buoyancy effects and lumps of fluid moved by turbulence fluctuations have no restoring force to return to their original position. When the flow is stratified, the buoyancy effect tends to restore the moved lumps back to their original position, and results in the reduction of the turbulent transfer of momentum and mass. Bowden and Hamilton (1975), among others, have pointed out the necessity of considering the buoyancy effects on the momentum and mass transfer in stratified flows. In order to consider the buoyancy effect of stratification, the momentum and mass diffusion coefficients were related to a dimensionless parameter, which is a function of vertical density and velocity gradients. Furthermore, according to many investigations based on measurements, a typical relationship between either vertical momentum diffusion coefficient, e_z, or mass diffusion coefficient, ε_z, and the dimensionless parameter,

R_i, is given as

$$e_z = e_o \left(1 + \alpha_1 R_i \right)^{q_1} \qquad (3.36)$$

or

$$\varepsilon_z = \varepsilon_o \left(1 + \alpha_2 R_i \right)^{q_2} \qquad (3.37)$$

where e_o and ε_o are the vertical momentum and mass diffusion coefficients in a homogeneous flow, respectively; α_1, q_1, α_2, and q_2 are constants needed to be calibrated using data; and R_i is the gradient Richardson number defined as follows:

$$R_i = \frac{g}{\rho} \frac{\frac{\partial \rho}{\partial z}}{\left(\frac{\partial u}{\partial z}\right)^2} \qquad (3.38)$$

which is generally used as a stability index in stratified flows (Turner, 1979). For the vertical diffusion coefficients, e_o and α_1 are assumed identical to ε_o and α_2, respectively, while q_1 is taken to be -1/2.

One well-known formula for the vertical mass diffusion coefficient has been suggested by Pritchard (1960). The formula was developed from a study of velocity and salinity distributions in the James River estuary by fitting observational results. The formulas of vertical mass diffusion coefficient in the stratified and homogeneous flow fields are given respectively as follows:

$$\epsilon_z = \epsilon_o (1 + 0.276 R_i) \qquad (3.39)$$

$$\epsilon_o = 8.59 \times 10^{-3} \frac{|u| z^2 (H-z)^2}{H^3} \qquad (3.40)$$

where H is the total water depth and z is the elevation at which ϵ_z is being calculated. In eq.3.39, α_2 and q_2 are equal to 0.276 and -2, respectively.

For the longitudinal momentum diffusion coefficient, e_x, Festa and Hansen (1976) changed the value of e_x from $e_x = e_z$ to $e_x = 10^6 e_z$ with negligible effects on the results of their tidal model. This indicates that the results are not sensitive to the actual value of e_x. Yet they found that varying the longitudinal mass diffusion coefficient, ϵ_x, from $\epsilon_x = \epsilon_z$ to $\epsilon_x = 10^7 \epsilon_z$ did produce significant changes in their model results. Dyer (1973) and Kuo et al. (1978) suggested that longitudinal momentum and mass diffusion coefficients are on the order 10^5 of the corresponding vertical diffusion coefficients.

Sediment settling velocity and deposition rate. In a mathematical model of sediment transport, model prediction is very sensitive to the settling velocity of suspended sediment given as input data. Thus the determination of sediment settling velocities for a mathematical model requires much care.

There are essentially four types of field or laboratory measurement of the suspension settling velocity mentioned by Mehta (1986): 1) the use of an *in situ* tube for prototype measurement, 2) fitting analytical solution to measured suspended sediment-depth profile from

the prototype measurement, 3) use of laboratory settling column, and 4) measurement of rates of deposition in the flume.

The measurement by means of a laboratory settling column for the settling velocities of fine-grained sediments used in the tests was made in the present study. The principle of this test is essentially based on the known relationship between the downward settling flux of suspended sediment and the dilution rate of suspension concentration in the settling column. During the test, the suspension samples are withdrawn at designated times from several vertically aligned taps, which are attached to the side wall of the settling column. The experimental facility and procedure of the settling column test performed in the present study were designed with reference to the work by Interagency Committee (1943), Mclaughlin (1959), Owen (1976), and Christodoulou et al. (1974). The results of the median settling velocity versus initial suspension concentration for each raw sediment are presented in Chapter 4. However, these settling velocities cannot appropriately represent the local suspension settling velocities in the closed-end channel due to the losses of a part of raw sediments before they reach the closed-end channel entrance and the non-uniform flow regime in the closed-end channel.

The suspension settling velocity in the closed-end channel, which is subject to local flow and concentration conditions, was computed based on the measurement of deposition rate from each test. These computed settling velocities are expected to be more realistic than those obtained using settling column analysis for representing the local settling velocities of suspension in the closed-end channel.

Therefore, the computed settling velocity was adopted as input data in the mathematical model.

In the present study, the bed shear stress generated by turbidity current was much smaller than the critical erosion shear stress which is on the order of 0.2 - 0.6 N/m^2 (Parchure and Mehta, 1985). Thus, the term for resuspension rate of bed material in the convective-diffusion equation was omitted.

The mass balance equation (eq.2.6) was used for computing the deposition rate of suspended sediment in the mathematical model. In this equation, the critical deposition shear stress, τ_{cd}, must be known before any computation. Therefore, an attempt at finding τ_{cd} for kaolinite was carried out based on the measured data in the main channel and is discussed in detail in Chapter 5. Note that the term for sediment deposition rate in the convective-diffusion equation is only considered at the bottom layer of the numerical grid system.

3.2.2 Finite Difference Formulation

There are many ways to present the derivative terms of the governing equations in the finite difference formulation for solving the flow velocity and sediment concentration numerically. An explicit numerical scheme was used to develop the mathematical model. In order to gain better stability and accuracy of the solutions of the finite difference formulations, the temporal, convective, and diffusive terms in the equations of motion and convective-diffusion were time- and space-centered.

With reference to the grid system of Fig.A.1 of the Appendix, three independent variables, x, z, and t denote longitudinal and

vertical space coordinates, and time, respectively. Using i and j to represent the number of space intervals in the x and z directions, respectively, and using n to denote the number of time intervals that have elapsed, variables will be represented using i, j, n subscripts, where i, j, or n = 0, 1, 2, 3, etc. The surface elevation, h, is a function of x and t only, while the layer thickness, Δz, is a function of t for the surface layer and a function of z only for the other layers.

The finite difference approximations of eqs.3.24, 3.25, 3.26, and 3.27 are:

the free surface elevation

$$\frac{h_i^{n+1} - h_i^{n-1}}{2\Delta t} = w_{i,N}^{n} - \frac{1}{\Delta x}\left[\frac{\Delta z_{i+1,N}^{n} + \Delta z_{i,N}^{n}}{2} u_{i,N}^{n} - \frac{\Delta z_{i,N}^{n} + \Delta z_{i-1,N}^{n}}{2} u_{i-1,N}^{n}\right] \qquad (3.41)$$

the vertical velocity

$$\frac{(w_{i,j+1}^{n} - w_{i,j}^{n})}{\Delta z_j^{n}} = -\frac{(u_{i,j}^{n} - u_{i-1,j}^{n})}{\Delta x} \qquad (3.42)$$

equation of motion

$$\frac{(u_{i,j}^{n+1} - u_{i,j}^{n-1})}{2\Delta t} = -\frac{[(u_{i,j}^{n} + u_{i+1,j}^{n})^2 - (u_{i-1,j}^{n} + u_{i,j}^{n})^2]}{4\Delta x}$$

$$- \frac{[(u^n_{i,j}+u^n_{i,j+1})(w^n_{i,j+1}+w^n_{i+1,j+1}) - (u^n_{i,j-1}+u^n_{i,j})(w^n_{i,j}+w^n_{i+1,j})]}{4\Delta z^n_j}$$

$$+ \frac{[(e_{x\,i,j}^{n+1}+e_{x\,i+1,j}^{n+1})(u^{n+1}_{i+1,j}-u^{n+1}_{i,j}) - (e_{x\,i-1,j}^{n-1}+e_{x\,i,j}^{n-1})(u^{n+1}_{i,j}-u^{n+1}_{i-1,j})]}{2\Delta x^2}$$

$$+ \frac{1}{\Delta z^{n+1}_j}\left[\frac{(e_{z\,i,j+1}^{n+1}+e_{z\,i+1,j+1}^{n-1})(u^{n+1}_{i,j+1}-u^{n+1}_{i,j})}{(\Delta z^{n+1}_j + \Delta z^{n-1}_{j+1})} - \frac{(e_{z\,i,j}^{n-1}+e_{z\,i+1,j}^{n+1})(u^{n-1}_{i,j}-u^{n-1}_{i,j-1})}{(\Delta z^{n+1}_j + \Delta z^{n+1}_{j-1})}\right]$$

$$- \frac{2\left(\frac{\partial p}{\partial x}\right)^2_{i,j}}{(\rho^n_{i,j} + \rho^n_{i+1,j})} \qquad (3.43)$$

and the convective-diffusion equation for sediemnt

$$\frac{(C^{n+1}_{i,j} - C^{n-1}_{i,j})}{2\Delta t} = - \frac{[(C^n_{i,j} + C^n_{i+1,j})u^n_{i,j} - (C^n_{i-1,j} + C^n_{i,j})u^n_{i-1,j}]}{2\Delta x}$$

$$- \frac{[(C^n_{i,j} + C^n_{i,j+1})(w^n_{i,j+1} - w_s) - (C^n_{i,j-1} + C^n_{i,j})(w^n_{i,j} - w_s)]}{2\Delta z^n_j}$$

$$+ \frac{[\varepsilon_{x\,i,j}^{n-1}(C^{n-1}_{i+1,j} - C^{n-1}_{i,j}) - \varepsilon_{x\,i-1,j}^{n-1}(C^{n-1}_{i,j} - C^{n-1}_{i-1,j})]}{\Delta x^2}$$

$$+ \frac{2}{\Delta z_j^{n-1}} \left[\frac{\varepsilon_{z_{i,j+1}}^{n-1} (C_{i,j+1}^{n-1} - C_{i,j}^{n-1})}{(\Delta z_j^{n-1} + \Delta z_{j+1}^{n-1})} - \frac{\varepsilon_{z_{i,j}}^{n-1} (C_{i,j}^{n-1} - C_{i,j-1}^{n-1})}{(\Delta z_{j-1}^{n-1} + \Delta z_j^{n-1})} \right] \qquad (3.44)$$

In addition, the finite difference formulation of the gradient Richardson number, eq.3.38, can be expressed as

$$R_i = - \frac{2g\,(\Delta z_{j+1}^{n} + \Delta z_j^{n})(\rho_{i,j+1}^{n} - \rho_{i,j}^{n})}{(\rho_{i,j+1}^{n} + \rho_{i,j}^{n})[(u_{i,j+1}^{n} - u_{i,j}^{n})^2 + (u_{i-1,j+1}^{n} - u_{i-1,j}^{n})^2]} \qquad (3.45)$$

The procedure of numerical calculation starts with all the variables assigned at their initial values, and moves from the channel entrance to the closed end in x direction, from the top layer to bottom layer in z direction. With all variables known at the n th time step, the continuity equation for the top layer (eq.3.41) is used to calculate h_i^{n+1}. With h_i^{n+1} known, $u_{i,j}^{n+1}$ and $C_{i,j}^{n+1}$ can be calculated for all i's and j's using equations 3.43 and 3.44. Knowing all the u's for the (n+1)st time step allows all the w's for the (n+1)st time step to be calculated using eq.3.41.

Next, the density, pressure gradient, and longitudinal and vertical mass diffusion coefficients are calculated for the (n+1)st time step. Subsequently, the entire procedure described is repeated to calculate the values of the variables at the (n+2)nd time step. A

brief flow chart which summaries the sequence of numerical calculations is shown in Appendix A.2.

3.2.3 Stability and Accuracy

As the derivatives in the governing equations are centered in time and space, the finite difference scheme has second order accuracy. Unconditional stability does not exist because explicit finite difference formulations are used. A stability analysis of the full set of governing equations is impossible due to the involvements of nonlinear terms and of the coupling characteristic. Instead, parts of the finite difference formulation representing different physical processes have been analyzed separately. The stability condition of each part is essential for the overall stabitity of the model, but is not sufficient to ensure that it is the stability criterion for the entire equation system. The stability condition (Courant-Friedrichs-Lewy condition) of the numerical solution when considering only temporal and linear convective terms in the finite difference equations of motion or convective-diffusion is

$$\Delta t \leq \frac{(\Delta x)_{min}}{u_{max}} \qquad (3.46)$$

which is valid for the explicit discretization of a hyperbolic equation. In eq.3.46, Δt is the time interval of each time step, $(\Delta x)_{min}$ is the minimum longitudinal space interval used in the grid system, and u_{max} is the maximum velocity occurring in the study area.

A linear parabolic equation including the temporal and diffusive terms, which are time- and space-centered with three successive time

levels, is expressed as

$$\frac{f_j^{n+1} - f_j^{n-1}}{2\Delta t} = A \frac{f_{j+1}^{n-1} - 2f_j^{n-1} + f_{j-1}^{n-1}}{\Delta x^2} \qquad (3.47)$$

where f denote velocity or sediment concentration, and A can be momentum or mass diffusion coefficient. The stability condition for eq.3.47, is derived using complex Fourier series analysis

$$\frac{A \cdot \Delta t}{(\Delta x)^2} < \frac{1}{4} \qquad (3.48)$$

The derivation of the inequality condition (eq.3.48) is given in Appendix A.3

The stability conditions found above provide guidance for selecting Δx, Δt, and momentum or mass diffusion coefficients.

3.2.4 Calibration and Verification

In the present study, calibration is defined as the adjustment of coefficients based on an assumption that the relations used in the model, in which the coefficients appear, adequately describe the physical phenomena under consideration. The unknown coefficients in the model are: 1) longitudinal and vertical momentum diffusion coefficients, e_x, e_z; 2) longitudinal and vertical mass diffusion coefficients, ε_x, ε_z; and 3) Manning roughness coefficient, n. Besides, some physical parameters need to be determined empirically; these include the settling velocity, w_s, and the critical deposition shear stress, τ_{cd}. The test COEL-4 was used as a calibration test, such that its conditions, i.e. water depth, water density, sediment specific gravity,

and concentration profile at the entrance of the closed-end channel, were related as the input data in the mathematical model simulation. In addition, for grid size (which is based on how detailed predictions in space one likes to obtain) and time step (which is referred to the stability conditions aforementioned), values of Δx=0.5 m, Δz=1.0 cm, and Δt=0.15 sec were adopted for simulating all tests of WES and COEL. Also, ε_x, ε_z are usually assumed to be identical to the longitudinal and vertical momentum diffusion coefficients, respectively, by virtue of Reynolds analogy. Since the turbidity currents were laminar in all the laboratory tests in the present study, the kinematic viscosity of water was used for e_z (i.e. $e_z = 10^{-6}$ m^2/sec). The longitudinal momentum diffusion coefficient, e_x, was determined with reference to the stability condition given as eq.3.48 and was found to be 5.0×10^{-3} m^2/sec. Manning's roughness coefficient, n, was 0.03 sec/$m^{1/3}$. This n value selection can be justified by comparing with an illustrative value n = 0.022 sec/$m^{1/3}$, which is obtained by utilizing the Moody diagram (Daily & Harleman, 1966) and eq.3.31 for a turbidity current with u = 0.5 cm and an interface thickness η = 5 cm. The calibration results are given in Chapter 5.

Model verification was carried out by checking how well the calibrated model reproduced the phenomena in other tests. Here, COEL-5 was selected as a verification test. Comparison between the results using the calibrated numerical model and experimental measurements for many aspects of test COEL-5 is given in Chapter 5.

3.3 Analytical Developments

3.3.1 Mean Sediment Concentration Below Interface

In order to examine the longitudinal variation of mean sediment concentration below interface in a stationary sediment wedge, an attempt at solving the steady state convective-diffusion equation analytically was made as follows.

The physical properties at each layer are assumed to be uniform. That is, the upper layer is assumed to be sediment-free, while the suspension concentration in the lower layer is assumed to be uniform. Also, the velocity profiles in both layers are assumed to be uniform. A schematic figure is shown in Fig.3.2. In the lower layer, upward vertical velocity of the fluid is small compared with the settling velocity of suspended sediment. Mass diffusion in both x and z directions is assumed to be negligible as compared with mass convection by flow. Under these assumptions the steady-state convective-diffusion equation can be expressed as

$$u \frac{\partial C}{\partial x} - w_s \frac{\partial C}{\partial z} = 0 \qquad (3.49)$$

Integrating eq.3.49 from bottom to interface, η, then using the boundary conditions at bottom ($C = \overline{C}_b$, at $z = 0$) and interface ($C = 0$, at $z = \eta$), an equation for mean concentration gradient is obtained

$$\frac{\partial \overline{C}_b}{\partial x} = - \frac{w_s}{u\eta} \overline{C}_b \qquad (3.50)$$

where $\overline{C}_b$ is the mean suspension concentration in the lower layer.

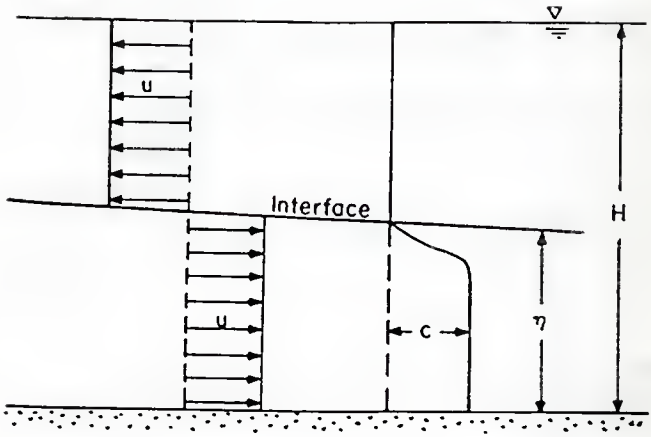

Figure 3.2. Schematic of Theoretical Two-Layered Model.

Furthermore, eq.3.50 is integrated from x=0 (i.e. the entrance of the close-end channel) to x. Since both w_s and u are functions of x, the integration of the term on the right hand side of eq.3.50 with dx cannot be carried out unless explicit forms of the functions, $w_s(x)$ and u(x), are known. According to the experimental observations from the present study, both sediment settling velocity and flow velocity decreased exponentially with distance from the entrance of the side channel. Therefore, w_s and u can be expressed as $w_s = w_{s1}\cdot\exp(-\beta_1 x)$ and $u = u_1\cdot\exp(-\beta_2 x)$, respectively, where w_{s1} and u_1 are the sediment settling velocity and the flow velocity at x = 0, and β_1, β_2 are constants. The thickness of the lower layer, η, is assumed unchanged because it decreases very slowly with x. Accordingly, the solution for the integration of eq.3.50 can be expressed as

$$\ln \frac{\overline{C}_b}{\overline{C}_{b1}} = -\frac{w_{s1}}{u_1 \eta(\beta_2 - \beta_1)} [\, e^{(\beta_2 - \beta_1)x} - 1 \,] \qquad (3.51)$$

where $\overline{C}_{b1}$ is the mean sediment concentration at x=0. The term $\exp[(\beta_2 - \beta_1)x]$ can be expanded using Taylor series, i.e. $1+(\beta_2-\beta_1)x+[(\beta_2-\beta_1)x]^2/2+\ldots\ldots$, and its second and higher order terms can be omitted if the exponent $(\beta_2-\beta_1)x$ is much less than unity (i.e. the local relative settling velocity w_s/u is very close to the ratio of w_{s1}/u_1 at the entrance). Also, it is assumed that η = constant·H and u_1 = constant·u_Δ, to relate these parameters (η and u_1) to the total water depth H and the densimetric velocity u_Δ, respectively. Finally, the dimensionless form of the relationship for the mean concentration below interface can be obtained as follows:

$$\frac{\bar{C}_b}{\bar{C}_{b1}} = \exp\left[-\beta\left(\frac{w_{s1}}{u_\Delta}\right)\left(\frac{x}{H}\right) \right] \qquad (3.52)$$

where β is a constant and must be determined empirically. The investigation of lock exchange flow (O'Brien & Cherno, 1934; Yih, 1965) showed that the interface at the gate and the initial front speed are equal to one half of the total water depth and densimetric velocity, respectively. Therefore, the β value in eq.3.52 could be expected to be larger than 4, since u_1 is smaller than the initial front speed and the interface at any location in the closed-end channel is lower than that at the entrance.

3.3.2 Flow Velocity

The unsteady state fluid motion in the closed-end channel is impossible to obtain by solving analytically the full set of equation of motion due to the nonlinear convection term involved (eq.3.21). As previously mentioned, there are three distinct phases found in the front motion of a gravity current, and the third phase is the so-called viscous self-similar phase, in which the front motion is governed by gravity and viscous forces. Huppert (1982) solved the flow velocity within the gravity current under this phase in a deep water channel. In the present study, a gravity-viscous force balance is also considered for solving the flow velocity in a sediment wedge arrested in a shallow water channel.

The channel may be assumed two-dimensional, and the length of the wedge will be considered to be much greater than the still water depth H. The layer above the interface will be assumed to be sediment-free;

all the sediment being confined to the wedge. Thus, momentum diffusion in the flow is more important in the vertical z-direction than in the horizontal x-direction. In addition, the closed end of the closed-end channel will result in a water surface slope towards the entrance, consequently, the hydrostatic head induced by the elevated water surface will balance the excess pressure due to the density gradient of sediment-laden water in the channel as well as the shear stress generated due to the vertical velocity gradient.

Under these conditions, the steady state equations of motion in x and z directions can be expressed as follows:

$$0 = -\frac{1}{\rho}\frac{\partial p}{\partial x} + e_z \frac{\partial^2 u}{\partial z^2} \qquad (3.53)$$

$$0 = -g - \frac{1}{\rho}\frac{\partial p}{\partial z} \qquad (3.54)$$

The horizontal pressure gradient term in eq.3.53 can be substituted by the result obtained by taking the horizontal derivative of the hydrostatic pressure from eq.3.54. In the upper layer, the horizontal pressure gradient is related only to free surface slope, but in the lower layer, this gradient is related to both the free surface slope and the horizontal density gradient. Therefore, eq.3.53 can be split into two equations corresponding to both layers, which are thus

$$e_z \frac{\partial^2 u}{\partial z^2} = g \frac{\partial h}{\partial x} \qquad \eta < z < h \qquad (3.55)$$

$$e_z \frac{\partial^2 u}{\partial z^2} = g \frac{\partial h}{\partial x} \frac{\rho_w}{\rho} + \frac{\rho_\eta - \rho_w}{\rho_w} g \frac{\partial \eta}{\partial x} + \frac{g}{\rho} \int_z^\eta \frac{\partial \rho}{\partial x} dz \qquad 0 < z < \eta \qquad (3.56)$$

where $h(x)$ is the elevation of free surface, and ρ_η is the density of sediment-water mixture at the interface. The second term on the right hand side in eq.3.56 can be neglected, since the fluid density at the interface, ρ_η, is very close to the water density, ρ_w. Here, the sediment concentration, C, is defined as the sediment mass per unit volume of water-sediment mixture. Therefore the density of the water-sediment mixture can be calculated from $\rho = \rho_w + C(1-1/G_s)$, where G_s is the specific gravity of sediment. The derivation of the relationship between ρ and C is given in Appendix B.1. Then the integration of $\partial\rho/\partial x$ in eq.3.56 can be carried out by using the expression of eq.3.52. In order to solve eqs.3.55 and 3.56, the following conditions are utilized; 1) no shear stress at the water surface (i.e. $\partial u/\partial z = 0$, at $z = h$), 2) no-slip boundary condition at the bed (i.e. $u = 0$, at $z = 0$), 3) the horizontal velocity is continuous at the interface, 4) the slope of vertical velocity profile is continuous at the interface, and 5) the volumetric rate of inflow in the lower layer is equal to the rate of outflow in the upper layer at every location in the closed-end channel (i.e. $\int_0^h u dz = 0$). Details of solving equations 3.55 and 3.56 are given in Appendix B.2.

The final solution of flow velocity in upper and lower layers are obtained as follows:

$$u = \frac{g s_o H^2}{e_z} \left[0.5\, \zeta^2 - \zeta + \frac{1}{3(1 - 0.25\xi)} \right] \qquad \xi < \zeta < 1 \qquad (3.57)$$

$$u = \frac{g s_o H^2}{e_z} \left[\frac{\zeta^3}{3\xi^3(1 - 0.25\xi)} + \left(0.5 - \frac{1}{\xi^2(1 - 0.25\xi)}\right) \zeta^2 \right.$$

$$\left. + \left(-1 + \frac{1}{\xi(1 - 0.25\xi)}\right) \zeta \right] \qquad 0 < \zeta < \xi \qquad (3.58)$$

where the water surface slope $s_o = \partial h/\partial x$, the dimensionless vertical coordinate $\zeta = z/h$, and the dimensionless interface elevation $\xi = \eta/h$. Eqs.3.57 and 3.58, in which s_o and ξ are the function of x, are valid everywhere in the closed-end channel except at the entrance where the water body is connected to open water, and the flow condition there is critical as found by Schijf and Schonfeld (1953). Furthermore, normalizing eqs.3.57 and 3.58 by the local surface outflow velocity, u_s, these equations become

$$\frac{u}{u_s} = \frac{(1.5 - 0.375\xi)\,\zeta^2 - (3 - 0.75\xi)\,\zeta + 1}{-0.5 + 0.375\xi} \qquad \xi < \zeta < 1 \qquad (3.59)$$

$$\frac{u}{u_s} = \frac{(\zeta/\xi)^3 + (-3 + 1.5\xi^2 - 0.375\xi^3)(\zeta/\xi)^2 + (3 - 3\xi + 0.75\xi^2)(\zeta/\xi)}{-0.5 + 0.375\xi} \qquad 0 < \zeta < \xi \qquad (3.60)$$

Note that u_s is always negative because the flow is towards the entrance.

3.3.3 Sediment Flux

Since analytical velocity solutions of eqs.3.57 and 3.58 are not applicable to the entrance of the closed-end channel, an attempt to develop a practical method for determining the sediment flux at the entrance of the channel is made in this section.

According to present and previous investigations, the initial front speed, u_{f1}, i.e., the particle velocity at the entrance immediately after the gate is removed, is approximately equal to one half of the densimetric velocity u_Δ. When the front of the turbidity current proceeds downstream along the closed-end channel, the flow velocity at the entrance, u_1, decreases and rapidly reaches a steady state. The particle velocity variation with the elapsed time at several locations in the closed-end channel is shown in Fig.5.5 in Chapter 5, which presents the simulation results obtained by the numerical model. From the results, it is observed that the period between the maximum velocity, i.e. during the front passing, and the steady state velocity is much shorter compared with the overall duration of the experiment, and the velocity at steady state is proportional to the maximum velocity. Therefore, it is reasonable to assume that a constant particle velocity at the entrance of the closed-end channel is established since the removal of the gate and u_1 = constant$\cdot u_{f1}$. Therefore, u_1 can be expressed as $u_1 = \alpha\, u_\Delta$, since $u_{f1} = 0.5\, u_\Delta$, where α is a constant and the densimetric velocity $u_\Delta = [\Delta\rho_1 gH/\rho_w]^{1/2}$. The sediment influx through the lower layer at the entrance per unit area is

$$S = u_1 \cdot \overline{C}_1 = \alpha \left[\frac{gH}{\rho_w}\left(1 - \frac{1}{Gs}\right) \right]^{1/2} \overline{C}_1^{3/2} \qquad (3.61)$$

where $\overline{C}_1$ is the depth-averaged concentration at the entrance of the closed-end channel. Note that the sediment flux into the closed-end channel is proportional to $\overline{C}_1^{3/2}$.

Prediction of sediment flux computed by eq.3.61 is compared with laboratory experimental results in Chapter 5.

3.3.4 Water Surface Rise

While a stationary sediment wedge is established in the closed-end channel, the water surface in the region beyond the toe of the sediment wedge must be raised in order to balance the excess force induced by density difference at the entrance. In this section, an attempt is made at solving for the maximum water surface rise, ΔH_{max}, based on momentmum conservation. A schematic diagram appears in Fig.3.3.

According to the equation of momentum conservation, the following expression can be deduced

$$F_1 + \bar{\rho}_{1L} Q_2 \bar{u}_2 = F_2 + \bar{\rho}_{1U} Q_1 \bar{u}_1 \qquad (3.62)$$

in which:

F_1, F_2 = hydrostatic forces acting on the cross sections at the entrance and wedge toe, respectively

$\bar{\rho}_{1U}$, $\bar{\rho}_{1L}$ = depth-averaged densities in upper and lower layers at the entrance, respectively

Q_1, Q_2 = discharges in upper and lower layers at the entrance, respectively and

$\bar{u}_1$, $\bar{u}_2$ = depth-averaged velocities in upper and lower layers at the entrance, respectively.

However, $Q_1 = Q_2$ must be satisfied due to the volumetric conservation of water at steady state. Accordingly, $\bar{u}_1$ is approximately equal to $\bar{u}_2$, since the interface elevation at the entrance is about one half of the water depth. Therefore, eq.3.62 reduces to

$$F_2 - F_1 = (\bar{\rho}_{1L} - \bar{\rho}_{1U}) Q_2 \bar{u}_2 \qquad (3.63)$$

in which:

$$F_1 = B \int_0^H \left(\int_0^H \rho_1(z) g dz \right) dz$$

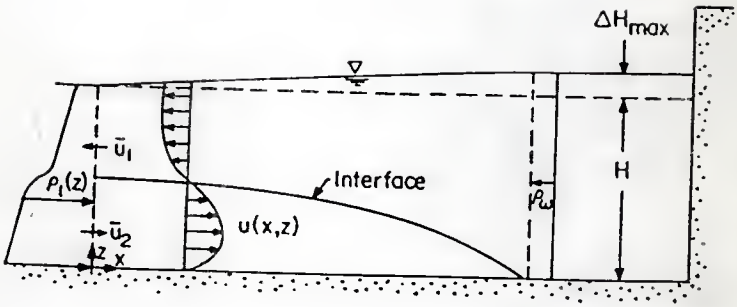

Figure 3.3. Schematic of Stationary Sediment Wedge and Water Surface Rise.

$$F_2 = \frac{B}{2} (H + \Delta H_{max})^2 \rho_w g, \text{ and}$$

B = channel width.

In eq.3.63, the term on the right hand side is assumed to be negligible because $(\bar{\rho}_{1L} - \bar{\rho}_{1U})$ is small. Also, for F_2, the term with the order of $(\Delta H_{max})^2$, is neglected, since ΔH_{max} is very small. Consequently, the rise of water surface at the region beyond the toe of the stationary sediment wedge, ΔH_{max}, is given as

$$\Delta H_{max} = \frac{1}{H} \{ \frac{1}{\rho_w} \int_0^H [\int_z^H \rho_1(z) dz] dz - \frac{H^2}{2} \} \qquad (3.64)$$

where $\rho_1(z)$ is the density profile at the entrance of the closed-end channel.

3.3.5 Tide-Induced to Turbidity Current-Induced Deposition Ratio

In many coastal regions, sedimentation occurring in closed-end channels have resulted from the combined effect of turbidity currents and tidal motions. It is of concern from an engineering viewpoint to distinguish the contribution of tide-induced deposition from total deposition. In this section, an attempt to estabilish a relationship between tide-induced deposition and turbidity current-induced deposition is made. A relationship for sediment flux into the closed-end channel due to turbidity currents has been derived as eq.3.61. The mass of sediment deposition over a tidal period can be computed as

$$M_D = S\ B\ (H/2)\ T \qquad (3.65)$$

where M_D is the mass of deposition induced by turbidity currents, and T is the tidal period.

Regarding tide-induced deposition, a simple way to compute the deposited mass over a tidal cycle is using the concept of tidal prism. This assumes that suspended sediment moves into the channel during flood tide, then parts of it settles at slack water, during ebb tide the remaining suspended sediment flows out of the channel. Accordingly, the deposition mass induced by tidal motion over a tidal cycle, M_T, is obtained as

$$M_T = 2\Omega\, a_o\, L\, B\, \overline{C}_1 \qquad (3.66)$$

where a_o is the tidal amplitude and Ω is the portion of sediment depositing inside the channel at slack water. $\Omega = 1$ if no sediment outflow during ebb tide, and $\Omega < 1$ if some sediment flows out of the channel. Consequently, the ratio of tide-induced to turbidity current -induced deposited mass (for $\Omega = 1$ case) can be obtained, by dividing eq.3.66 by eq.3.65, as

$$\frac{M_T}{M_D} = 11.42 \left(\frac{\Delta\rho_1}{\rho_w}\right)^{-1/2} \left(\frac{a_o}{H}\right) \left(\frac{L}{L'}\right) \qquad (3.67)$$

where $\Delta\rho_1$ is the excess density at the channel entrance, and L' is the tidal wave length in shallow water, $L'=(gH)^{1/2}T$. In eq.3.65, three basic dimensionless parameters are included, i.e. $\Delta\rho_1/\rho_w$, the relative excess density at the channel entrance, a_o/H, the relative tidal amplitude, and L/L', the channel length to tidal length ratio.

CHAPTER 4
EXPERIMENTAL EQUIPMENT AND PROCEDURES

Two sets of experiments were conducted in the present study. The first was performed in a flume system at the U. S. Army Corps of Engineers Waterways Experiment Station (WES), Vicksburg, Mississippi. These experiments served as the preliminary study for an understanding of turbidity current and sedimentation in a closed-end channel. The experimental results have been presented by Lin and Mehta (1986). During the tests, considerable temperature gradients in the flume were observed. The second set of experiments was conducted in a smaller size of flume system in a room with temperature control at the Coastal Engineering Laboratory (COEL) of the University of Florida. Observations in detail on the behavior of turbidity current and associated sedimentation were made.

4.1 Experiments at WES

4.1.1 Experimental Set-up

The laboratory tests at WES were performed in a T-shaped flume (Fig.1.1). A 9.1 m long, 0.46 m deep, and 0.23 m wide closed-end channel was orthogonally connected to a 100 m long, 0.46 m deep, and 0.23 m wide main channel at the approximate midpoint of the main channel. Fig.4.1 shows the experimental set-up schematically. Both main and closed-end channels were horizontal and made of 6 mm thick lucite. The walls of the main channel were artificially roughened

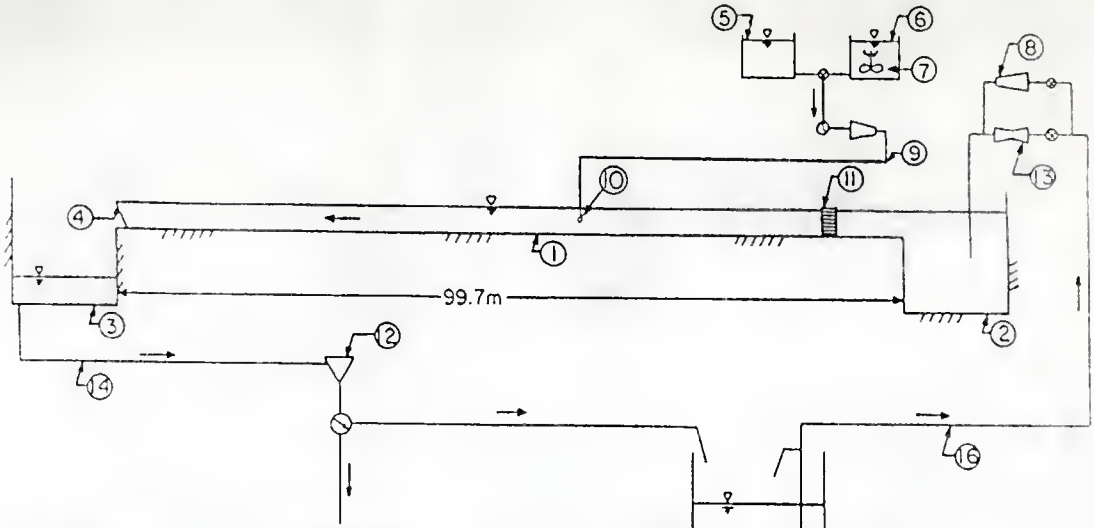

1 Flume
2 Headbay
3 Tailbay
4 Tailgate
5 Water Tank
6 Slurry Tank
7 Propellers
8 Rotameter
9 2.5cm Feed Line
10 Injection Manifold
11 Flow Straightener
12 V-Notch Weir
13 Venturi Meter
14 15.2cm Return Line
15 Supply Sump
16 15.2cm Supply Line

Figure 4.1. Schematic of Hydraulic System at WES (Elevation View).

using the lucite elements. Previous measurements in the main channel showed that the main channel had a Manning's roughness coefficient n = 0.022 with the artificially roughened walls (Dixit et al. 1982).

Other components of the experimental set-up comprised:

1) A 6.1 m square and 1.5 m deep basin at each end of the main channel. The upstream basin including an overflow weir structure served as the headbay and the basin at the downstream end as the tailbay.
2) Fluid injection apparatus consisting of a water tank of 114 liter capacity and a slurry tank of 4500 liter capacity. As shown in Fig.4.1, a quick action valve controlled the water supply between the water tank and the slurry tank. Four sets of 15 cm propellers driven by a 945 rpm electric motor and a mixing pump were provided in the slurry tank. One end of a 2.5 cm diameter hose was connected with the outlet of a rotameter, and the other was placed in the main channel 6.0 m upstream from the entrance center of the Closed-end channel.
3) Venturi meter attached to the water supply pipe towards the headbay in order to monitor the flow rate from the supply sump to the headbay.
4) V-notch weir to measure discharge from the main channel.

4.1.2 Auxiliary Equipment

1) Point gauges for the measurement of water surface and bed elevations at the main and closed-end channels.
2) Digital electric thermometers, shown in Fig.4.2, to monitor the temperature variation of fluid in the main and closed-end chan-

nels. The thermometers could read up to the second decimal place in degrees Fahrenheit.

3) A rotating cup current meter for measuring the distribution of the horizontal velocity over the vertical in the main channel. The frequency of wheel revolution could be converted to the flow velocity from a calibration curve.

4) The suspension sampling apparatus consisted of several sampling devices and a vacuum pump. Each sampling device included four taps aligned vertically, as shown in Fig.4.3; the inner diameter of each tap was 3 mm. One end of each tap was connected by a long, flexible plastic tube to a set of 50 ml plastic jars located in a closed rectangular plastic box. In all, 30 jars were placed in the closed box for collecting the suspension samples from different locations and elevations during each test. The outlet of the closed box was connected to a vacuum pump.

4.1.3 Test Materials

Five kinds of sediment were used in the laboratory experiments at WES: 1) kaolinite, 2) silica flour, 3) flyash I, 4) flyash II, and 5) Vicksburg loess. The kaolinite was available commercially (Feldspar Coorporation, Edgar, Florida). The size distribution of the kaolinite is given in Fig.4.4. The median particle diameter was 1.2 μm. The cation exchange capacity was found to be approximately 6.0 milliequivalents per 100 grams (Parchure, 1983). Its specific gravity was 2.57 (Lott, 1986).

The particle size distribution of silica flour obtained by a Sedigraph Particle Size Analyzer, which uses an x-ray beam to detect

Figure 4.2. A Digital Electric Thermometer at WES.

Figure 4.3. Suspension Sampling Apparatus Deployed in the WES Flume.

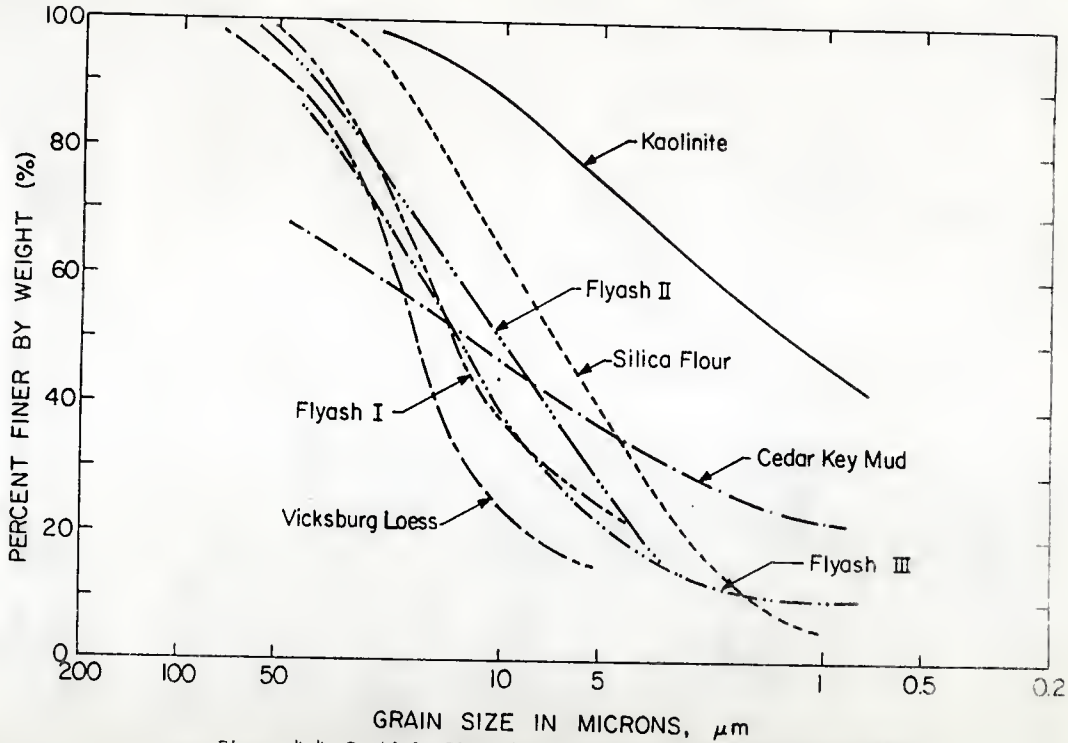

Figure 4.4. Particle Size Distributions of Fine-Grained Sediments

the concentration decrease due to settling in a sample cell, is shown in Fig.4.4. The median particle diameter was 7 μm. The specific gravity of the sediment was 2.65. No organic matter was found.

The particle size distribution of flyash I was obtained using the Sedigraph Analyzer and is shown in Fig.4.4. The median particle diameter was 14 μm. The specific gravity of the sediment was 2.45. Loss on ignition was found to be 3.7 percent.

The particle size distribution of flyash II was also obtained by the Sedigraph Analyzer and is shown in Fig.4.4. The median diameter was 10 μm. The specific gravity of the sediment was 2.37. Loss on ignition was found to be 1.0 percent.

The particle size distribution of the Vicksburg loess was obtained by Hydrometer analysis and is shown in Fig.4.4. The median particle diameter of the sediment was 18 μm. X-ray diffraction analysis was conducted at WES in order to identify the clay and nonclay minerals of the loess. It was found to consist of five clay minerals, which are chlorite, illite, kaolinite, montmorillonite, and vermiculite, as well as three major nonclay minerals, which are quartz, feldspar, and dolomite. The cation exchange capacity was found to be approximately 19 milliequivalents per 100 grams. The specific gravity was 2.68, and the organic content was found to be 0.6 percent.

As mentioned in Chapter 3, the settling velocities of raw fine sediments used in both WES and COEL flume tests were determined by settling column analysis. Two different sizes of settling column were used, as shown in Fig.4.5; one was 1.15 m high, 10 cm square, (designated as column no.1), and the other was 1.9 m high, 10 cm in diameter,

Figure 4.5. Two Different Size Settling Columns with a Mixing Pump.

(designated as column no.2). A mixing pump was used to help fully mix the water and fine sediment by passing air bubbles into the column prior to the beginning of a test. Inasmuch as the settling velocity is dependent upon sediment concentration for cohesive sediment, several tests were conducted with different initial concentrations for each sediment. The relationship of median settling velocity to the initial sediment concentration for each sediment is shown in Fig.4.6. A detailed description of the column test procedure is given by Lott (1986).

The chemical composition of water used in the tests at the WES flume is given in Table 4.1 (Dixit et al. 1982).

Table 4.1 Chemical Composition of a water sample from the 100 m flume (after Dixit et al. 1982)

Ions	ppm
Ca^{++}	1.9
Mg^{++}	0.7
Na^{+}	13.1
K^{+}	6.6
Mn^{++}	0.0
Fe^{+++}	0.0
Cl^{-}	18.3
Electrical Conductivity	0.19 mmho/cm
PH	7.8

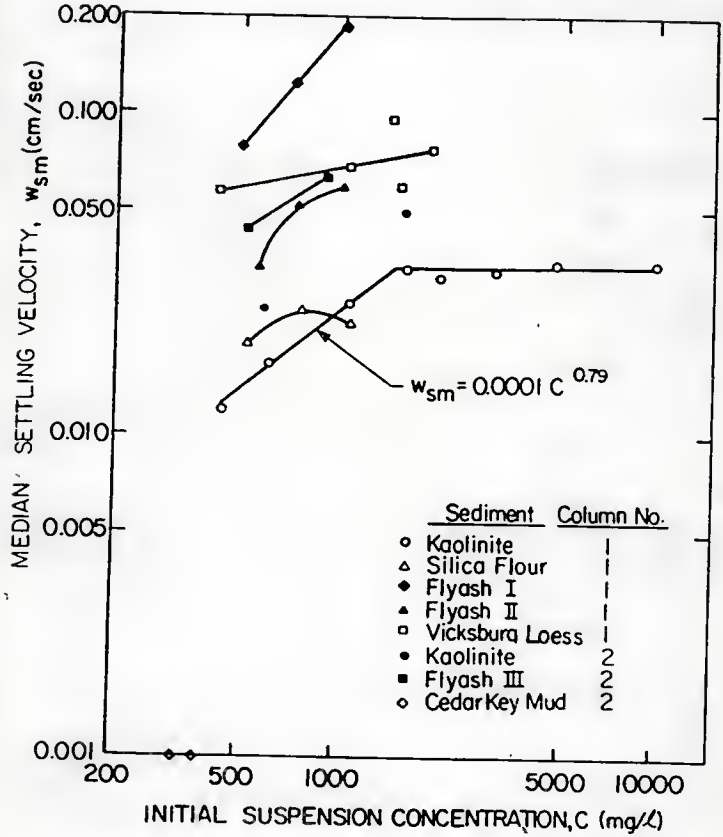

Figure 4.6. Median Settling Velocity vs. Concentration.

4.1.4 Experimental Procedure

1) The flow rate of fresh water to the headbay was adjusted until a calibrated reading of the venturi meter was attained. Thereafter, the flow was kept running for about 1.5 hours in order to establish a steady flow with a desired water depth and velocity in the main channel. Within the period of establishing the steady flow, the gate located at the entrance was kept open.
2) The appropriate amounts of test sediment and water were mixed in the slurry tank to obtain a desired slurry concentration. The mixing propellers and the pump started operating before the sediment was added to the tank. For easy observation of the movement of turbidity current in the closed-end channel, Rhodamine dye (red) was added to the slurry tank.
3) Fresh water from the water tank was pumped into the main channel through the injection hose at a flow rate equal to the slurry injection rate required. The injection flow rate was selected to obtain the desired suspension concentration in the flow of the main channel.
4) Until the flow in the main channel became stable, the gate of the closed-end channel was closed, a vertical velocity profile at the main channel, 1.5 m dowmstream from the entrance center of the closed-end channel, was obtained.
5) A quick action valve was switched to change the injection from fresh water to slurry, then the sediment slurry injection to the main channel was kept at the constant flow rate throughout the test.

6) With a constant flow rate of slurry in the main channel, the gate of the closed-end channel was removed allowing the sediment-laden water to intrude into the closed-end channel along the lower layer. The interface between the fresh water and the sediment front was traced several times during a test on transparencies, which were attached on the side wall with a scale reference.

7) Thirteen point gauges deployed in the main and closed-end channels are shown in Fig.4.7. The distance scale of the point gauge location is the same as the length scale of the closed-end channel. Water surface and bed elevations were measured using point gauges in the main and closed-end channels at three different times during a test, (i.e. during a constant flow rate of fresh water in the main channel with the entrance gate closed, a constant flow rate of fresh water in the main channel with the gate open, and a constant flow rate of sediment-laden water in the main channel with the gate open).

8) Three probes of digitalized electric thermometers were mounted on point gauge supports in the main and closed-end channels as shown in Fig.4.7. Vertical temperature profiles were taken periodically at all three locations.

9) A dye injection technique and floating tracer particles were used to measure vertical and lateral velocity profiles in the closed-end channel.

10) Seven suspension sampling devices were deployed in the main and closed-end channels as shown in Fig.4.7. The distance scale of the sampling device location was the same as the length scale of the

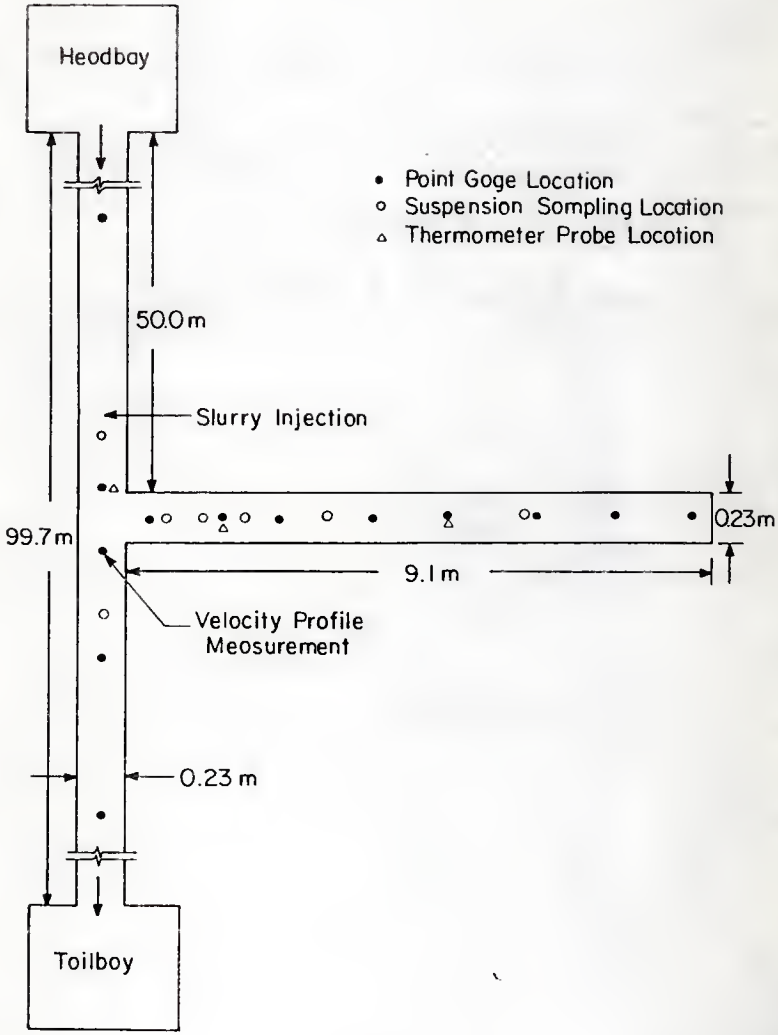

Figure 4.7. Locations of Measurements in WES Tests (Plan View).

closed-end channel. Suspension samples of the water-sediment mixture were withdrawn from all taps using a vacuum pump, towards the end of a test.

11) After the suspension samples were withdrawn, the gate of the closed-end channel was closed, but a slow release of water out of the channel was allowed without disturbing the deposited sediment in the closed-end channel.

12) In four out of thirteen tests, the deposits were collected at various subsections from the bed of the closed-end channel at approximate 24 hours after the test was completed.

A summary of test conditions for the thirteen tests at WES is given in Table 4.2.

4.2 Experiments at COEL

4.2.1 Experimental Set-up

A total of fourteen tests was performed at COEL in a T-shaped flume, which consisted of a closed-end channel orthogonally connected to a main channel at 2.83 m from the upstream end of the main channel. The closed-end channel was 14.7 m long, 0.1 m wide, 0.19 m deep, and was constructed of plexiglass of 1.3 cm thickness. The main channel was 4.26 m long, 0.16 m wide, 0.19 m deep, and was also made of plexiglass. A plexiglass gate was located at the junction of the closed-end channel with the main channel. In a total of the fourteen tests, twelve tests (Nos. 1-8 & 11-12 & 13-14) may be considered steady flow and two (Nos. 9 & 10) were tests with tidal effect. The hydraulic system components are shown in Fig.4.8.

Table 4.2. Summary of Test Conditions at WES.

Parameter	Test Number												
	1	2	3	4	5	6	7	8	9	10	11	12	13
Sediment	Kaolinite	Kaolinite	Kaolinite	Kaolinite	Kaolinite	Kaolinite	Kaolinite	Kaolinite	Silica flour	Flyash I	Flyash I	Flyash II	Vicksburg Loess
$\bar{C}_o$ - Depth-mean concentration in main channel (mg/l)	166	86	261	292	912	132	349	1878	203	58	365	1098	352
$\Delta\rho_o$ - Density difference in main channel. (g/cm^3)	0.000101	0.000053	0.000159	0.000178	0.000557	0.000081	0.000213	0.001187	0.000126	0.000038	0.000216	0.000635	0.000221
H - Total water depth, (cm)	12.7	7.9	7.9	8.4	9.2	8.4	8.2	5.0	8.8	8.6	8.8	6.0	5.7
$\bar{u}_o$ - Depth-mean velocity in main channel (cm/sec)	24.0	21.0	21.0	22.0	22.0	23.0	22.0	16.0	22.0	22.0	22.0	17.0	17.0
Minimum/Maximum water temperature in flume system during test (°C)	15.0/16.4	15.0/17.2	15.6/17.2	17.2/20.0	18.3/20.6	18.3/20.0	16.7/20.0	20.5/23.3	18.3/22.1	19.1/22.4	18.8/20.7	21.0/23.7	19.7/24.2
Mean water temperature, (°C)	15.7	16.1	16.4	18.6	19.5	19.2	18.4	21.9	20.2	20.8	19.8	22.4	22.0
Duration of test after gate opening, (minute)	—	234	104	90	48	100	158	175	187	175	215	168	276

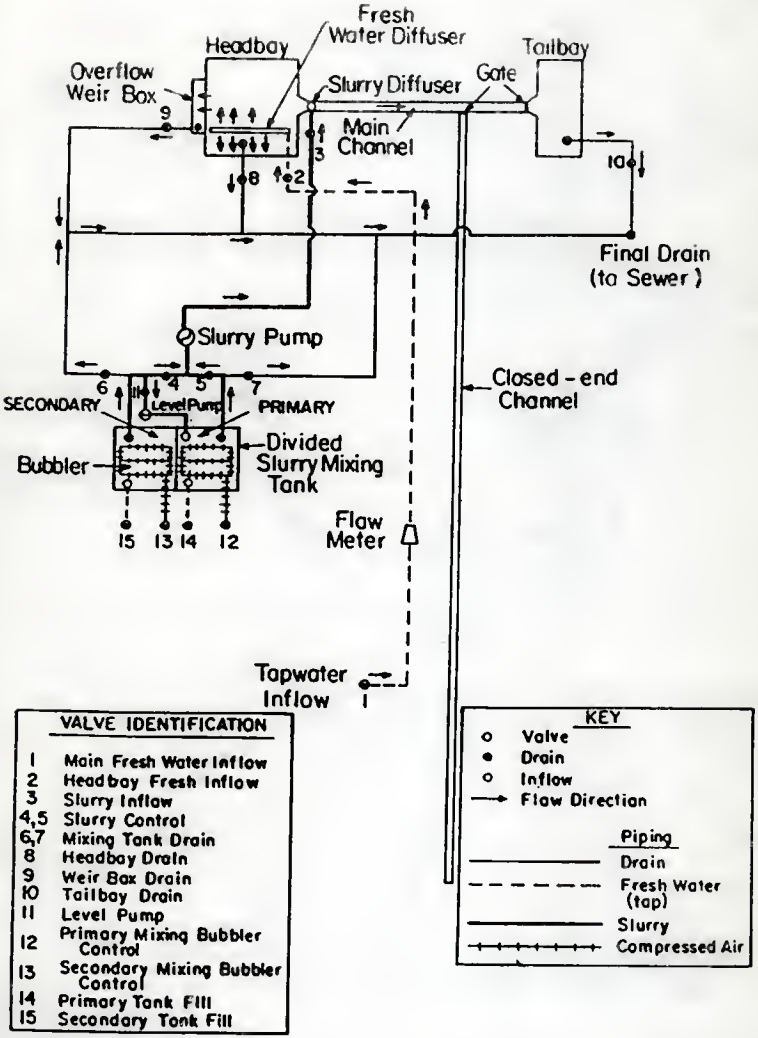

Figure 4.8. Schematic of Hydraulic System at COEL (Plan View).

The components of the experimental set-up for the steady flow tests and the tests with tidal effect comprised the following:

1) A 1.8 m square and 0.3 m in deep basin used as the headbay. An overflow weir structure was located on the upstream side wall of the headbay as shown in Fig.4.8. The elevation of the gate could be fixed, or varied continuously to simulate a sinusoidal tide using a variable-speed electric motor.
2) A fresh water diffuser lying on the bottom of the headbay. The diffuser was made of a section of perforated PVC pipe. Fresh water entered the headbay through either side of the diffuser so that water surface disturbances could be reduced to the minimum.
3) A rectangular basin, 1.83 by 0.89 m, used as the tailbay. A plexiglass tail gate constructed at the junction of the main channel with the tailbay could be adjusted to obtain the desired water depth and flow velocity in the main channel.
4) A mixing tank consisting of a primary tank and a secondary tank. Each tank was 1.21 m square, 1.82 m in deep and had an individually controlled air bubbler apparatus. The air bubbler consisted of steel piping perforated with holes so that rising air bubbles induced turbulence and mixing.
5) A slurry injection diffuser located at the head of the main channel. A slurry pump with variable speed control was connected with the outlet of the primary tank and with the slurry injection diffuser. The slurry pump was used to establish a desired flow rate from the primary tank to the main channel through the slurry injection diffuser.

6) A float switch/level control pump system consisting of a float switch in the primary tank and a level control pump. In order to obtain a constant flow rate of slurry out of the primary tank, a relatively constant water surface elevation in the primary tank had to be maintained. When the water surface elevation dropped below a preset level, the level control pump automatically turned on and began pumping the slurry from the secondary tank into the primary tank.

Detailed descriptions of the use of the control valves in the piping system, flow direction in the pipeline, and the design of the slurry injection diffuser are given by Lott (1986).

4.2.2 Auxiliary Equipment

1) The suspension sampling apparatus was deployed at eight locations as shown in Fig.4.9. At each location, seven taps, each of 3 mm diameter, were vertically and equally spaced along the side wall over a depth of 10.5 cm. Each tap was connected to a short length of a plastic tube. The plastic tubes were upheld by a tube holder when not used.

2) Two in-line flowmeters were installed in the fresh water pipeline and slurry injection pipeline, respectively. A device connected to each flowmeter converted the rotation frequency of the flowmeter impeller into an electrical signal. The output voltage read with a volt meter corresponded to the flow rate in the pipe.

3) An electric temperature probe/meter was used to obtain the water temperature at any desired depth and location.

4) Two point gauges were used for measuring the water surface and bed

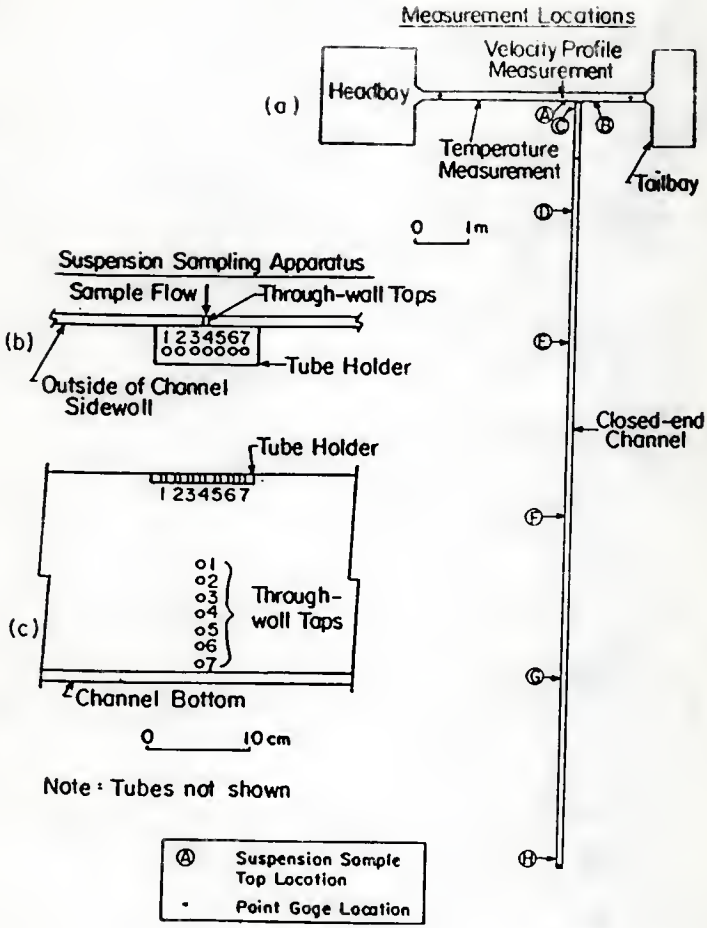

Figure 4.9. Locations of Measurements and Sampling Apparatus.
Measurement Locations (a) Plan.
Suspension Sampling Apparatus (b) Plan, (c) Elevation.

elevations at any desired location. The point gauge could read with a precision of 0.1 mm.

5) A 13 mm diameter electromagnetic current meter, mounted on a point gauge support shown in Fig.4.10, was used to measure vertical velocity profiles in the main channel.

6) Sony video equipment was used to measure front speed, observe front shape, and measure vertical velocity profiles in the closed-end channel. In order to have a scale reference in the picture whenever the video camera viewed through the closed-end channel, a plastic tape indicating the longitudinal distance, transparencies with a grid reference, and transparent metric rulers were deployed along the channel and on the side wall of the channel. The video equipment mainly consisted of a video camera, a tape recorder, a time/date generator, and a TV monitor. A dye injection technique in conjunction with the video equipment was used to obtain the vertical velocity profiles at the desired locations in the closed-end channel.

7) A vacuum pump was used to collect the deposited sediment from various bed subsections in the main and closed-end channels.

4.2.3 Test Materials

Three kinds of sediments were used in the tests at COEL: 1) kaolinite, 2) flyash III, and 3) Cedar Key mud. The kaolinite was the same as that used at WES.

The particle size distribution of flyash III was obtained using pipette analysis and is shown in Fig.4.4. The median particle diameter was 13.7 μm. The specific gravity of the sediment was 2.63.

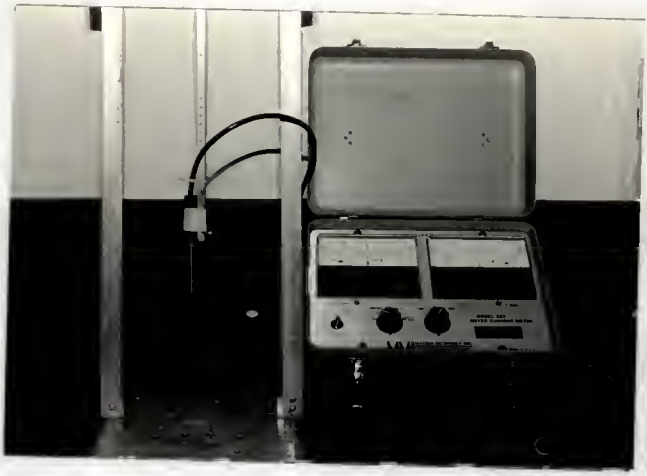

Figure 4.10. Electromagnetic Current Meter.

The particle size distribution of Cedar Key mud was obtained using pipette analysis and is shown in Fig.4.4. The dark soft mud was collected from Cedar Key on the Gulf Coast of Florida. The median particle diameter was 2.3 μm, and the specific gravity of the mud was 2.36.

A settling column analysis was also conducted for flyash 111 and Cedar Key mud, and the relationships of median settling velocity to the initial sediment concentration are shown in Fig.4.6.

Tap water was used as the fluid in these experiments, the chemical composition of this water is shown in Table 4.3 (Dixit, 1982).

4.2.4 Experimental Procedure

The procedure for the experiments at COEL was somewhat different from that at WES due to the different laboratory setup, equipment and measurement needs. The procedure at COEL was as follows.

Table 4.3

Chemical Composition of the Tap Water (after Dixit, 1982)

Cl	26 ppm
NO_3	0.07 ppm
Fe	0.5 ppm
K	1.4 ppm
Ca	25 ppm
Mg	16 ppm
Na	10 ppm
Total Salts	278 ppm
PH	8.5 ppm

Steady Flow tests. The experimental procedure described here is for the steady flow tests.

1) At the beginning, a steady flow with the desired flow rate and suspension concentration in the main channel was established. The operation involved adjustments of the tail gate at the main channel and overflow weir at headbay, as well as the controls of the water surface elevation in the channels and slurry concentration in the primary mixing tank in coordination with the in-line flowmeters and voltmeter. A detailed description of this operation is given by Lott (1986).

2) After the steady flow was established in the main channel, the gate of the closed-end channel was closed. Subsequently, the main channel velocity profile was measured using the electromagnetic current meter. The first set of suspension samples was withdrawn at tap locations A and B. The temperature of the flow in the main channel and of the water in the closed-end channel (with the gate closed) were recorded. All measurement locations can be seen in Fig.4.9.

3) Then as the gate at the entrance was removed, the slurry in the main channel was allowed to move into the closed-end channel. As the front of turbidity current moved down the channel, the video camera was moved alongside to continously record the travelling time, position, and shape of the front together with the nearby scale references.

4) The suspension samples were withdrawn from the taps immediately as the front passed each sampling location, so that the concentration

of the front could be determined.

5) At several times during the test, the interface between the clear water and the turbid water was traced on the transparencies, which were attached on the side wall of the closed-end channel.

6) During the test, two types of velocity measurements in the closed-end channel were made. One was surface velocity, which was obtained by measuring the required time for a dye parcel (methyl blue) to move over a known distance of 5 or 10 cm. At each location, the measurement was repeated several times in order to obtain a mean value. The other measurement was the vertical velocity profile, which was obtained by injecting a vertical streak of dye and recording its horizontal displacement either by the video camera or by tracing it on the transparency.

7) A set of suspension samples was withdrawn from all taps in the layer of the water-sediment mixture in the closed-end channel and the main channel at locations A and B, when the secondary mixing tank was almost empty.

8) Vertical temperature profiles were recorded periodically in the main and closed-end channels in order to monitor the temperature variation with time and space throughout the test.

9) If a test was of a comparatively long duration, the nearly empty secondary tank had to be refilled and well mixed with the appropriate amounts of tap water and the sediment. During the refilling, a measurable drop in the water level in the primary tank was observed.

10) Just before finishing a test, a set of suspension samples was

collected from all taps in the closed-end channel and the main channel at locations A and B.

11) At the end of a test, the gate of the closed-end channel and the tail gate in the main channel were closed. The water in the main channel and the closed-end was allowed to drain slowly through the sampling taps and the drain hole on the bottom of the headbay without disturbing the bottom deposits in the main and closed-end channels.

12) About 24 hours later, the main and closed-end channels were divided into several sections and the bottom deposit in each was pumped into a plastic jar using a vacuum pump.

Tests with tidal effect. The experimental procedure for steady flow tests was also valid for the tests with tidal effect. In addition, the water surface elevation at the main channel was changed by adjusting the elevation of the overflow weir to simulate the tidal effect on the movement of turbidity current and the associated sedimentation in the closed-end channel. In COEL-9 with "flood tide," the water surface elevation in main channel was increased twice (each increase by a step), then decreased twice (each decrease by a step), to return back to the original surface level. The magnitude of each surface elevation change and the corresponding time are given in Fig.4.11. In COEL-10 with "ebb tide," the water surface elevation in the main channel was dropped twice (each drop by a step), then increased twice (each increase by a step), and is shown in Fig.4.11. A summary of test conditions for the tests performed at COEL is given in Table 4.4.

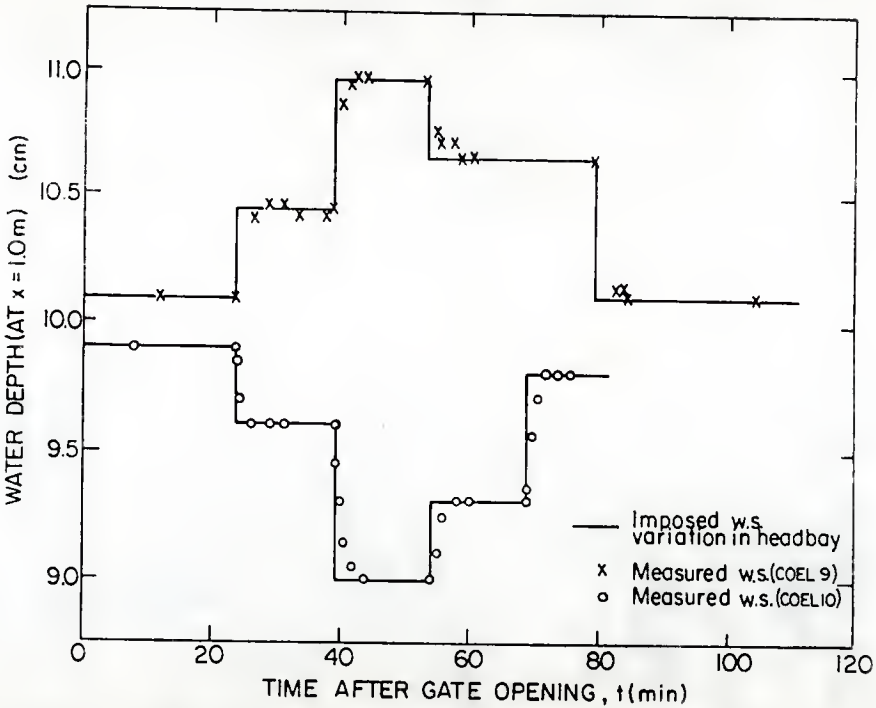

Figure 4.11. Water Surface Variation for Tide Effect Tests.

Table 4.4. Summary of Test Conditions at COEL.

Parameter	Test Number													
	1	2	3	4	5	6	7	8	9	10	11	12	13	14
Sediment	Kaolinite	Kaolinite	Kaolinite	Kaolinite	Kaolinite	flyash III	flyash III	flyash III	kaolinite	kaolinite	kaolinite	Cedar Key mud	kaolinite	kaolinite
$\bar{c}_0$ = Depth-mean concentration in main channel (mg/l)	313	3748	2248	1375	908	554	471	585	1926	1370	1547	250	1433	1692
$\Delta\rho_0$ = Density difference in main channel, (g/cm3)	0.000190	0.002290	0.001370	0.000840	0.000550	0.000340	0.00029	0.00036	0.00118	0.00084	0.00095	0.00014	0.00088	0.00103
H = Total water depth, (cm)	8.0	10.3	9.6	10.6	9.3	10.5	10.2	9.4	10.1 (initial)	9.9 (initial)	10.0	10.3	10.3	10.5
$\bar{u}_0$ = Depth-mean velocity in main channel (cm/sec)	30.5	7.3	12.8	11.3	15.4	11.0	14.3	16.6	16.2	19.8	18.8	18.7	19.5	18.6
Minimum/Maximum water temperature in flume system during test (°C)	—	26.5/26.9	26.2/26.9	26.2/26.8	25.8/26.0	25.8/26.0	25.2/25.5	24.2/24.7	23.9/24.7	22.2/23.1	22.1/22.4	18.6/19.1	19.5/19.7	19.6/20.0
Mean water temperature, (°C)	26.8	26.7	26.6	26.5	25.8	25.9	25.4	24.5	24.3	22.7	22.3	18.9	19.6	19.8
Duration of test after gate opening, (minute)	113	131	143	149	220	265	212	106	234	94	99	233	240	230

CHAPTER 5
RESULTS AND DISCUSSION

5.1 Typical Results

'Typical' refers to a representative format of the results, in that results given in this section generally represent directly measured experimental parameters and supplementary results generated using the numerical model and/or computed by analytically derived formulas. These results are from an individual test (COEL-5), which was also used to verify the calibrated numerical model. A complete set of typical results is presented to illustrate the fundamental mechanics of a turbidity front, a stationary sediment wedge, and associated sedimentation in a closed-end channel. In order to emphasize the magnitude of these physical quantities of concern, a dimensional format with arithmetic axes is chosen for the plots.

5.1.1 Main Channel

Vertical velocity profile. The purpose of establishing a steady flow in the main channel is to keep the suspension concentration unchanged throughout a test. The locations for measuring the vertical velocity profile and the procedure were presented in Chapter 4. Fig.5.1 exhibits a vertical velocity profile measured in the main channel in test COEL-5. The horizontal velocity in the main channel is denoted as u_o, and the depth-mean velocity, $\bar{u}_o$, is assumed to be identical to the horizontal velocity at the elevation $z = H/e$, where e

is the base of natural logarithm, based on the logarithmic velocity profile assumption. The ranges of $\bar{u}_o$ were 16.0-24.0 cm/sec in WES tests, and 7.3-19.8 cm/sec in COEL tests, respectively. The individual depth-mean velocity for each test is given in Table 4.2 and 4.4.

Vertical sediment concentration profile. The vertical distribution of suspended sediment concentration in the main channel near the entrance of the closed-end channel is the factor controlling the turbidity current and sedimentation in the closed-end channel. The suspension concentration, C_o, given in Fig.5.2 was taken from an arithmetic mean of concentrations at locations A and B over three withdrawal times. Fig.5.2 shows an approximately uniform vertical concentration profile in test COEL-5. The depth-mean concentrations in the main channel, denoted as $\bar{C}_o$, for all tests performed at WES and COEL are given in Tables 4.2 and 4.4.

5.1.2 Closed-End Channel

Time variation of front position. As mentioned in Chapter 2, three distinct phases (i.e. initial adjustment phase, inertial self-similar phase, and viscous self-similar phase) have been found in the front propagation of salinity-induced gravity current along a channel. A plot of front position, x_f, with the elapsed time, t, for test COEL-5 is given in Fig.5.3. Three distinct slopes on the curve are observed. Among them, two slopes at the early stage (slopes of 1 and 2/3) are identical to the characteristics of the initial adjustment phase and inertial self-similar phase, respectively, of sanility-induced gravity currents (Fig.2.3). During the phase of the initial adjustment, the turbidity front propagated with a constant speed, which was

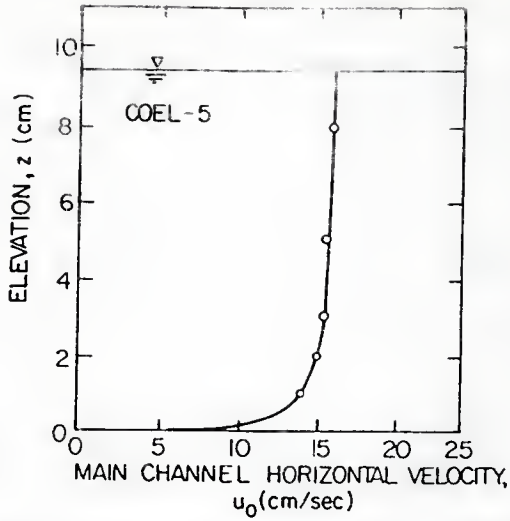

Figure 5.1. Main Channel Horizontal Velocity vs. Elevation.

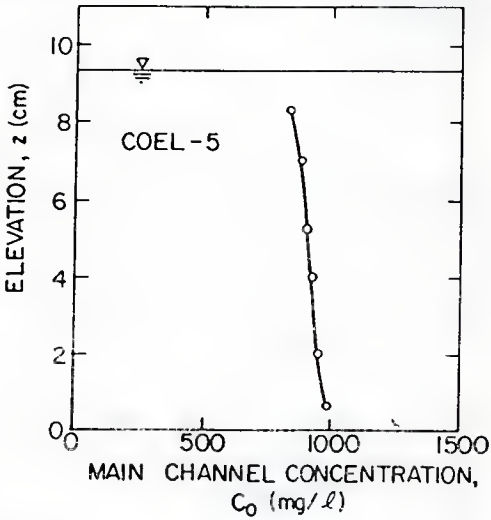

Figure 5.2. Main Channel Concentration vs. Elevation.

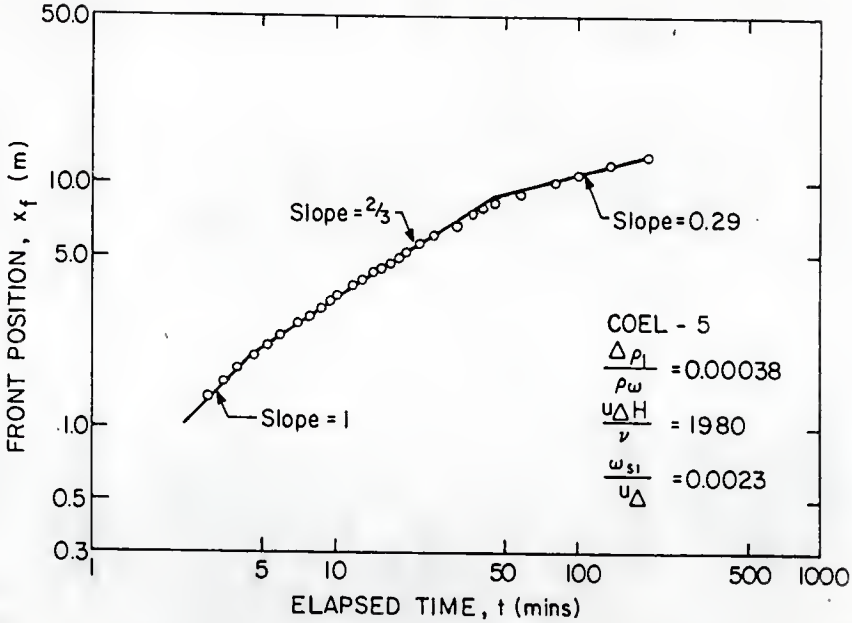

Figure 5.3. Front Position vs. Elapsed Time.

motivated by the initial density gradient between the main and closed-end channels. During the inertial self-similar phase, in which the force balance is dominated by inertia and gravity forces, the turbidity front proceeded at a speed proportional to $t^{-1/3}$, where t is the elapsed time. The third slope observed on the curve in Fig.5.3 has a value of 0.29, which is slightly higher than the slope of 1/5 (the characteristic value of the viscous self-similar phase for salinity current). It suggests that during this period, the front movement was not completely controlled by gravity and viscous forces, possibly due to an extra force introduced by a longitudinal temperature gradient, which was observed during the test.

Distance variation of front speed. The variation with distance of front velocity, u_f, obtained from measured travel interval and travel time, is plotted in Fig.5.4. The data show that the front velocity rapidly decreased as the front propagated farther downstream along the channel. The deceleration of front velocity is mainly induced by a drag force per unit width, which is against the front movement and equal to $0.5C_D\rho_w u_f^2 h_2$, where C_D is drag coefficient and h_2 is the front head height. Also, the motive force of front motion per unit width, $0.5\Delta\rho' g h_2^2$, decreased with distance from the entrance of the channel. The reduction of the motive force was mainly due to the decrease of front density by sediment deposition and interfacial mixing. Therefore, it would be expected that the rate of the decrease of front speed with distance of a turbidity current will be faster than that of a salinity-induced gravity current, in which the front density decreases due only to interfacial mixing.

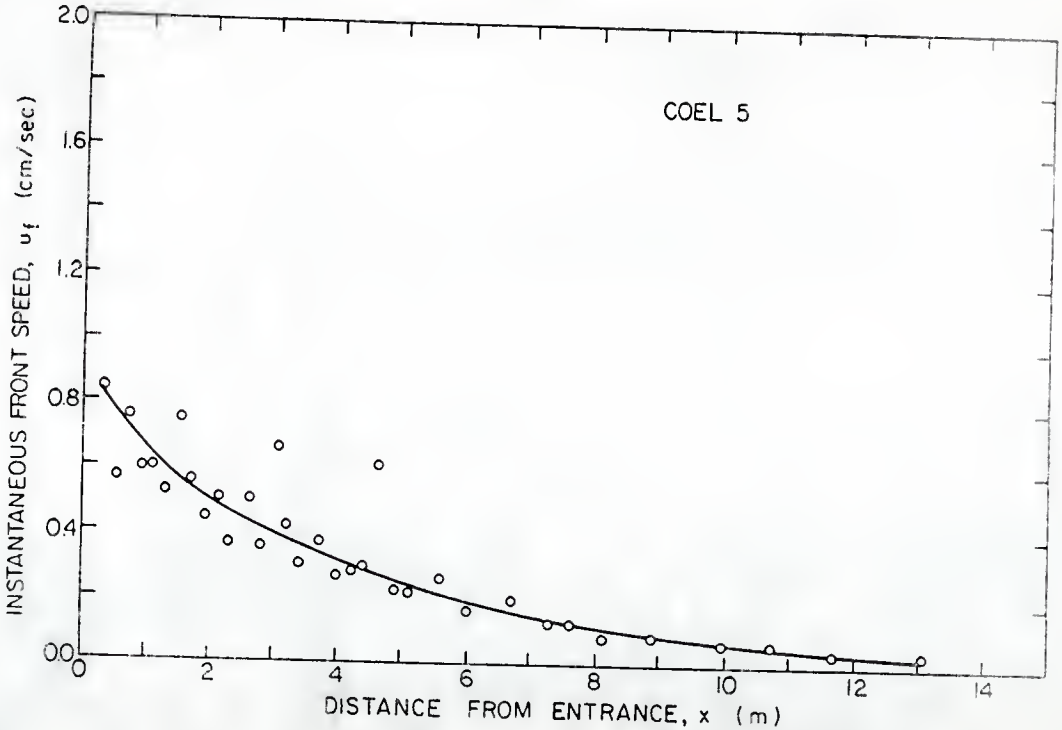

Figure 5.4. Instantaneous Front Speed vs. Distance From Entrance.

Time variation of horizontal velocity. The flow velocities in the closed-end channel generated in laboratory tests at WES and COEL were less than 1.0 cm/sec. For such small density currents, dye injection technique is often used by many investigators (e.g. Sturm & Kennedy, 1980; Brocard & Harleman, 1980) to measure the horizontal velocity profile over vertical. Unlike the density currents induced by salinity and temperature gradients, visibility in the turbidity current is low. Thus, for the velocity profile measurement in the present study, a vertical streak of dye was injected at a location approximately 1 cm away from the side wall, and the subsequent times of dye displacement were recorded. These measured magnitudes of horizontal velocity were smaller than the flow velocities occurring at the center of the channel due to side wall resistance (Lin & Mehta, 1986). In addition, due to the lack of several succesive measurements of the vertical velocity profile, the temporal and spatial variations of horizontal velocity in the channel are demonstrated by simulation results obtained using the numerical model.

The variation of the maximum horizontal velocity in the lower layer, at z = 2.5 cm, with the elapsed time for various locations in the channel is shown in Fig.5.5. The velocity was obtained using the calibrated numerical model with the given conditions of test COEL-5. In Fig.5.5, curves of horizontal velocity vs. time at x = 0.0 m and 2.0 m show that the horizontal velocity at 2.5 cm elevation increases from zero to a maximum value, then decreases and eventually reaches a steady value. It was observed experimentally that the maximum value (i.e. the peak of the curve) occurred at the moment when the turbidity front

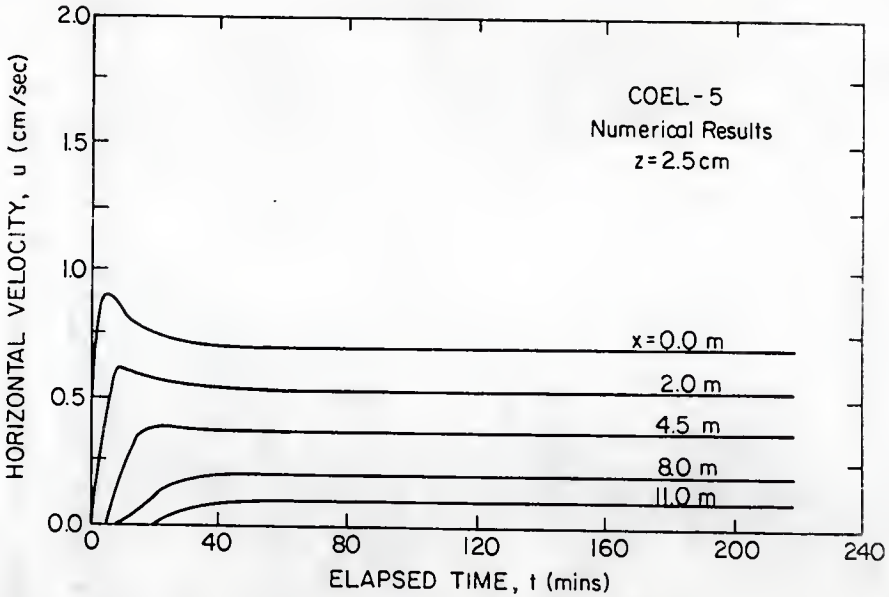

Figure 5.5.Horizontal Velocity at z=2.5 cm vs. Elapsed Time at Five Locations.

passed the observation point. Note that the time required for the establishment of a steady horizontal velocity after the passing of the front at a fixed location is relatively short.

Time variation of horizontal velocity profile. Fig.5.6 exhibits the vertical velocity profile, generated by using the calibrated numerical model, at x = 2.0 m for four different elapsed times. In the figure, positive velocity is identified as being towards the closed end. At times 60 minutes and 220 minutes after gate opening, the occurrence of identical velocity profile suggests that a steady horizontal velocity at x = 2.0 m has been established. Also, a decrease of the magnitude of horizontal velocity and an increase of the interface elevation of the velocity profile with increasing time are observed.

Distance variation of horizontal velocity profile. The distance variation of the steady state horizontal velocity profile is shown in Fig.5.7. These profiles were produced by the calibrated numerical model with the test conditions of COEL#5. It can been shown that the discharge in the layer below interface is equal to the discharge in the layer above interface at all three locations, which satisfies the condition of volumetric conservation of water at steady state. In addition, from the figure a decrease in the magnitude of the horizontal velocity and of the interface elevation with increasing x are observed. A contour plot of the steady state flow regime in the channel is given in Fig.5.8.

A comparison of the vertical velocity profile among experimental, numerical, and/or analytical results was made for test COEL#6 (not

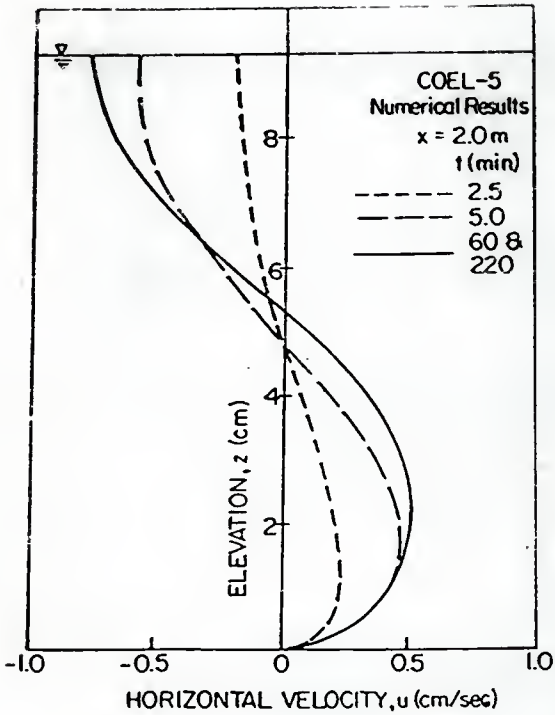

Figure 5.6. Horizontal Velocity vs. Elevation at Four different times After Gate Opening.

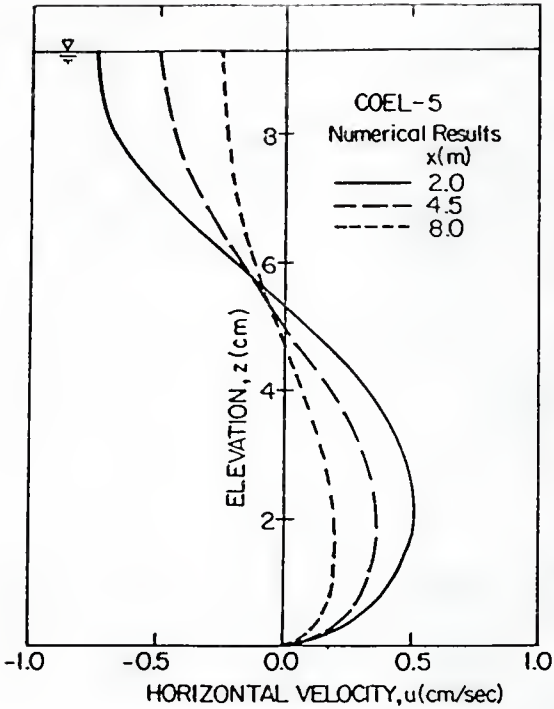

Figure 5.7. Horizontal Velocity at Steady State vs. Elevation for Three Locations.

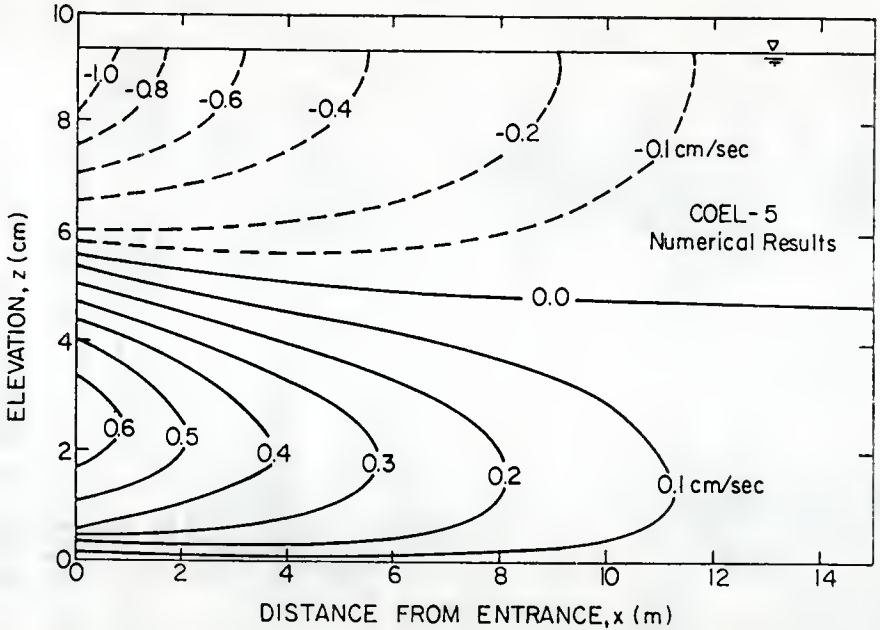

Figure 5.8. Horizontal Velocity Contours at Steady State in Closed-End Channel.

sufficient measured data of horizontal velocity in COEL-5 test). These rerults are presented in a dimensionless format and discussed in Appendix B.3.

Time variation of suspension concentration. As mentioned in section 3.2.4, test COEL-4 was selected as a calibration test to calibrate five unknown coefficients (i.e., horizontal and vertical momentum and mass diffusion coefficients e_x, e_z, ε_x, ε_z, and Manning's n), in the numerical model. After comparing the numerical results with the corresponding measurements in COEL-4, these calibrated values for the best-fitting comparisons were found to be the following: $e_x = \varepsilon_x = 5.0 \times 10^{-3}$ m^2/sec, $e_z = \varepsilon_z = 10^{-6}$ m^2/sec, and n = 0.03. Also as noted, the values of $\Delta x = 0.5$ m, $\Delta z = 1.0$ cm, and $\Delta t = 0.15$ sec, were adopted in the numerical simulation. Fig.5.9 shows the calibration result of the time variation of suspension concentration at z = 0.7 cm for various locations in the closed-end channel. In each test, the suspension concentration profile at each sampling location was generally measured at three different times, and the first of the three measurements was taken during the passage of the turbidity front. The symbols given in Fig.5.9 represent the measured data at different times and various locations, while the lines represent the calculations by using the numerical model with the aforementioned coefficients.

The calibrated numerical model was verified using the measured data of COEL-5, and the verification result is shown in Fig.5.10. In Fig.5.10, the variation of bottom suspension concentration (at z = 0.7 cm) with elapsed time at various locations in the channel is given. The symbols in Fig.5.10 are measurements at different times and various

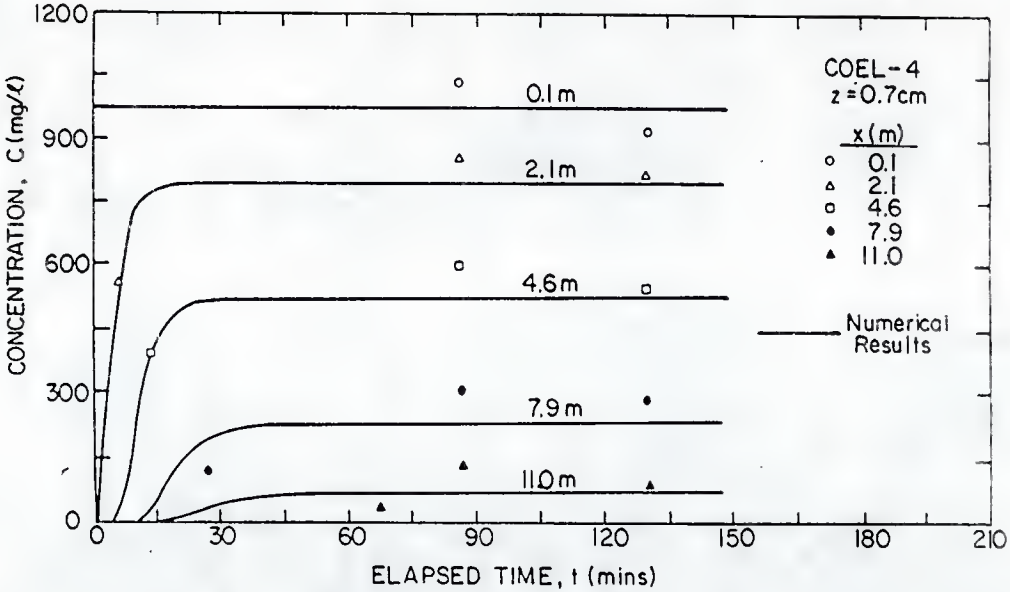

Figure 5.9. Concentration at z= 0.7 cm vs. Elapsed Time for Five Locations. (Calibration Results)

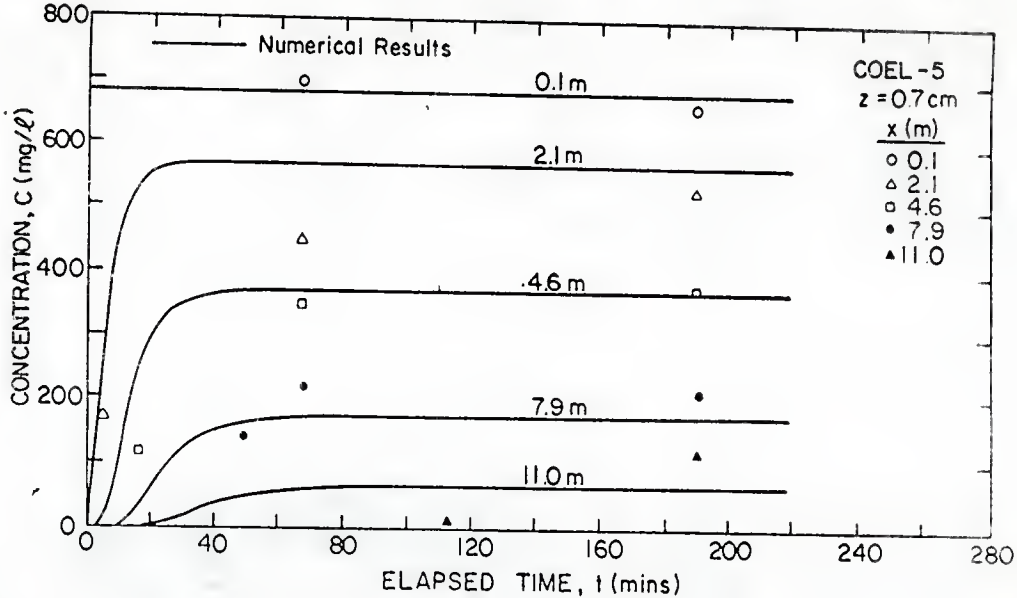

Figure 5.10. Concentration at z = 0.7 cm vs. Elapsed Time for Five Locations. (Verification Results)

locations, and the lines indicate predicted results using the calibrated numerical model at the corresponding locations. A reasonable agreement between the measured data and numerical results is observed. It is also noted that the suspension concentration at a particular location during the front passage was lower than that at the steady state.

Distance variation of concentration profile. Fig.5.11 shows the calibration result of the distance variation of the vertical concentration profile in the channel for test COEL-4. The vertical concentration profiles measured at 86 minutes and 130 minutes after gate opening at various sampling locations as well as profiles generated by the numerical model (with the calibrated coefficients) at the corresponding times and locations are shown in Fig.5.11.

Fig.5.12 shows model verification of the distance variation of vertical concentration profile in the channel for COEL-5. The vertical concentration profiles measured at 67 minutes and 190 minutes after gate opening at various sampling locations, as well as the corresponding numerical results, are shown in Fig.5.12. A good agreement between the measured concentration profile and numerical prediction is observed for the locations of x = 0.1, 2.1, and 4.6 m. But, at locations x = 7.9 and 11.0 m, the numerical results are observed to give slightly lower values than those of measured data. This discrepancy may be induced by using relatively high settling velocity in the numerical model for the location near the end of the channel, where the sediment settling velocity could be smaller due to the sediment sorting effect of a non-uniform flow regime, as well as measurement errors involved

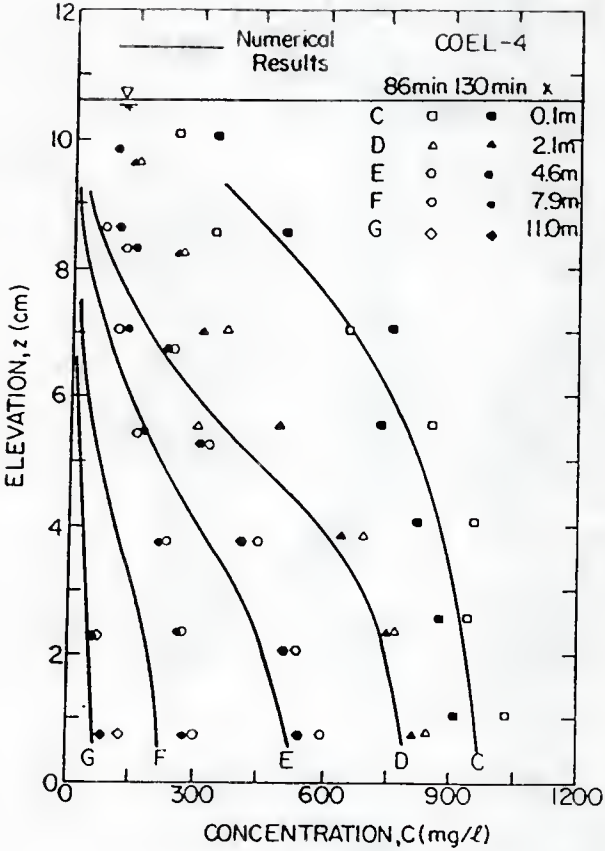

Figure 5.11. Concentration at Steady State vs. Elevation at Five Locations. (Calibration Results)

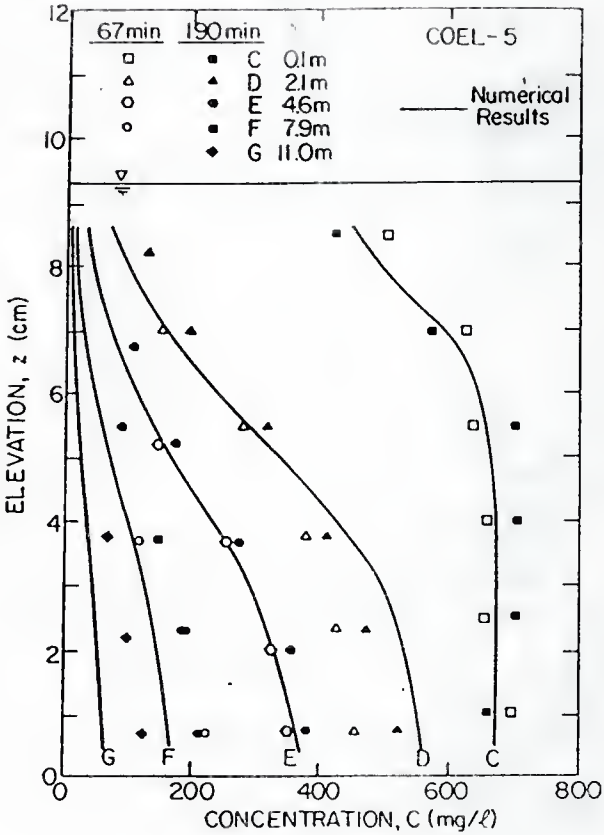

Figure 5.12. Concentration at Steady State vs. Elevation for Five Locations. (Verification Results)

in the gravimetric procedure for low sediment concentration. The concentration profiles at times 67 minutes and 190 minutes obtained by using the numerical model are identical at various locations, suggesting that the steady state concentration profile has been established 67 minutes after the gate opened. Yet, the measured concentration profiles at the time 67 minutes and 190 minutes are not identical, as shown in Fig.5.12. This is mainly due to a slightly higher boundary concentration at main channel introduced during the period between 67 minutes and 190 minutes after gate opening and due as well to the analysis errors of the collected liquid samples.

Distance variation of concentration at front head. As mentioned before, the decrease of the sediment concentration at the turbidity front with distance is induced by sediment deposition and to some extent by interfacial mixing. Fig.5.13 shows the distance variation of sediment concentration at front head in COEL-5. The data point in the figure represents the suspension concentration at z = 0.7 cm (i.e. the elevation of the lowest tap at each sampling location), during the passage of the turbidity front. Note that no front concentration was taken from section C (the sampling location at x = 0.1 m of the channel), because, there, the turbidity intrusion from the main channel was driven by shear-induced circulation (within the gyre zone as shown in Fig.1.1). According to Keulegan's (1957) investigation on the lock exchange flows of saline water, front dilution is more pronounced in the lock flows having relatively small Reynolds number. Nevertheless, there are no adequate experimental data from his investigation that can be used to compare with the result shown in Fig.5.13. Since the front

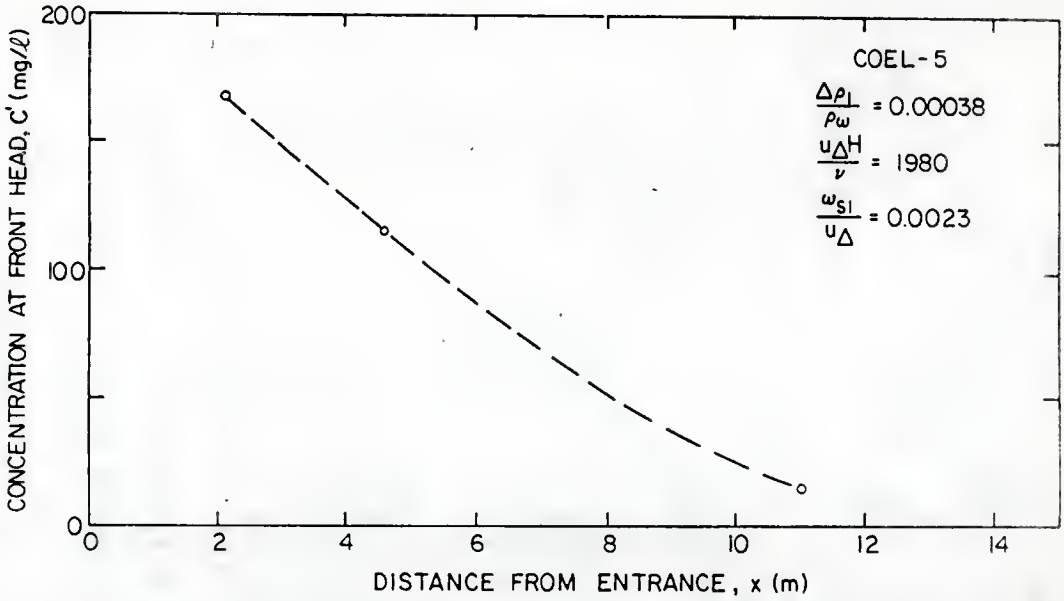

Figure 5.13. Concentration at Front Head vs. Distance From Entrance.

dilution of salinity-induced density current is only affected by interfacial mixing, it should be expected that the decrease of front density with distance at the turbidity front will be faster than that of a salinity front under the same initial conditions. Fig.5.13 exhibits a rapid decrease of suspension concentration at the turbidity front with distance.

Distance variation of mean concentration below interface. Under a steady state, longitudinal variations of mean concentration below the interface, $\overline{C}_b$, is given in Fig.5.14 and Fig.5.15, where the interface is defined as the zero-velocity elevation. Fig.5.14 shows the calibration result, including measured data and numerical results for COEL-4. The measured mean concentration below the interface at the sampling location was obtained by averaging the mean concentration below the interface at 86 minutes and 130 minutes after gate opening. Fig.5.15 shows the verification result by comparing the measured data and the corresponding numerical result for COEL-5, and in addition, includes analytical result obtained by using eq.3.52. It can be seen from Fig.5.15 that the measured mean concentration below the interface (obtained by averaging the concentrations at times 67 minutes and 190 minutes) exponentially decreases with distance from the entrance. The decrease of mean concentration below the interface along the channel resulted from the deposition of suspended sediment and the interfacial mixing of the sediment through the interface. Also, the rapidly decreasing concentration suggests that the assumption of constant sediment concentration along the channel, made by McDowell (1971) in his theoretical study on the settling solids-induced currents, may be

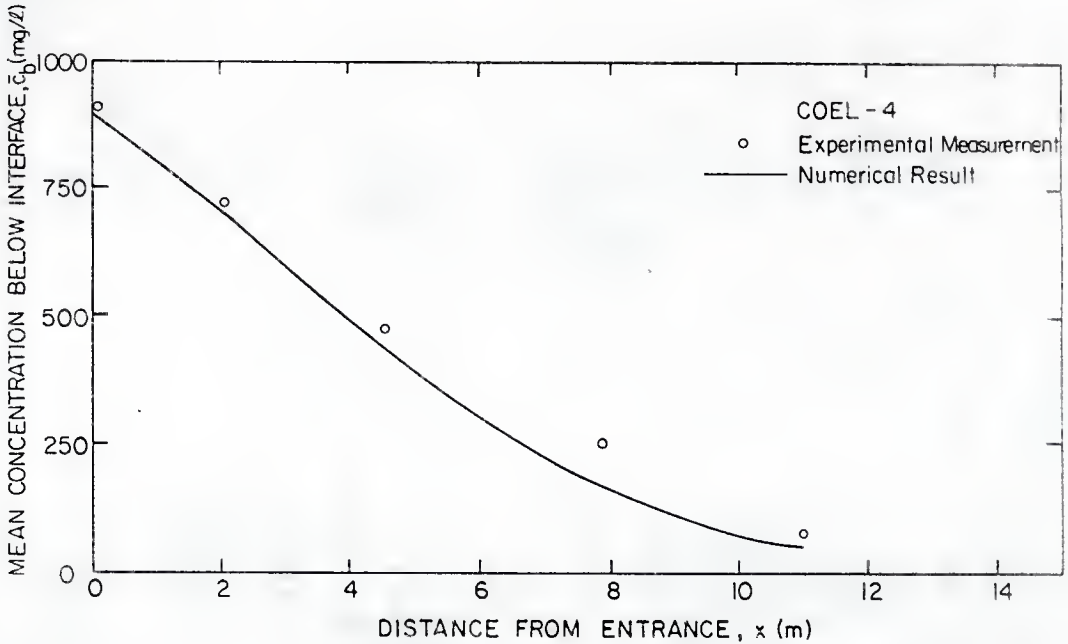

Figure 5.14. Mean Concentration Below Interface vs. Distance From Entrance. (Calibration Results)

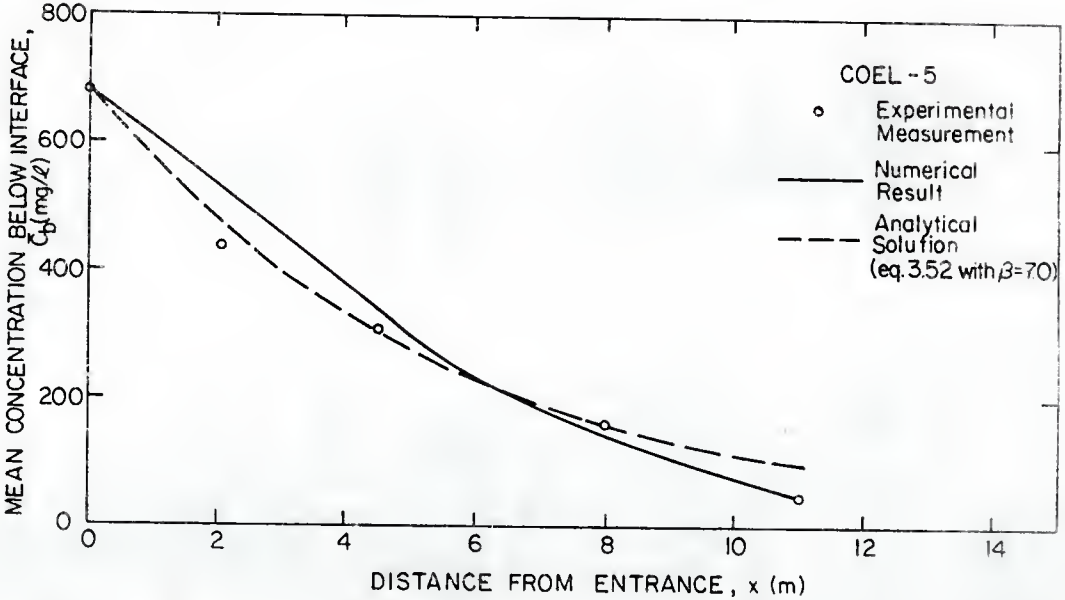

Figure 5.15. Mean Concentration Below Interface vs. Distance From Entrance. (Verification Results)

inappropriate for solids having high settling velocity. The longitudinal distribution of mean concentration below the interface obtained by the numerical model and the analytical approach are also shown in Fig.5.15. The calibrated coefficient $\beta = 7.0$ in eq.3.52 indicates that the stationary sediment wedge had a velocity at entrance $u_1 = 0.57\ u_{f1}$, which is close to the experimental result, $u_1 = 0.70\ u_{f1}$, found by Gole et al. (1973). Comparison shows a good agreement between the numerical and theoretical results with the measured data. In addition, a plot of concentration contour, obtained from the results of numerical simulation, for test COEL-5 at steady state is shown in Fig.5.16.

Longitudinal variation of water surface. The longitudinal variation of the water surface in the channel discussed in this section is represented by the elevation difference, $\Delta H(x)$, between local water depth and the water depth at the entrance. Since the magnitude of ΔH was on the order of 0.01 mm in all tests, the measurement of ΔH using a point gauge was out of the question. Instead, the longitudinal variations of ΔH in the channel for COEL-5 were simulated using the numerical model, as shown in Fig.5.17. The longitudinal variations of ΔH at 5 minutes and 15 minutes may be referred to as the unsteady cases, and at times 90 minutes and 180 minutes (identical curve) may be considered as the steady state case. During unsteady state, the propagation of small surface waves, induced by the intrusion of dense fluid into the clear water, can be seen in the figure. At steady state, the water surface rises from the entrance towards the closed end, and reaches a horizontal level at the location beyond the toe of a stationary sediment wedge.

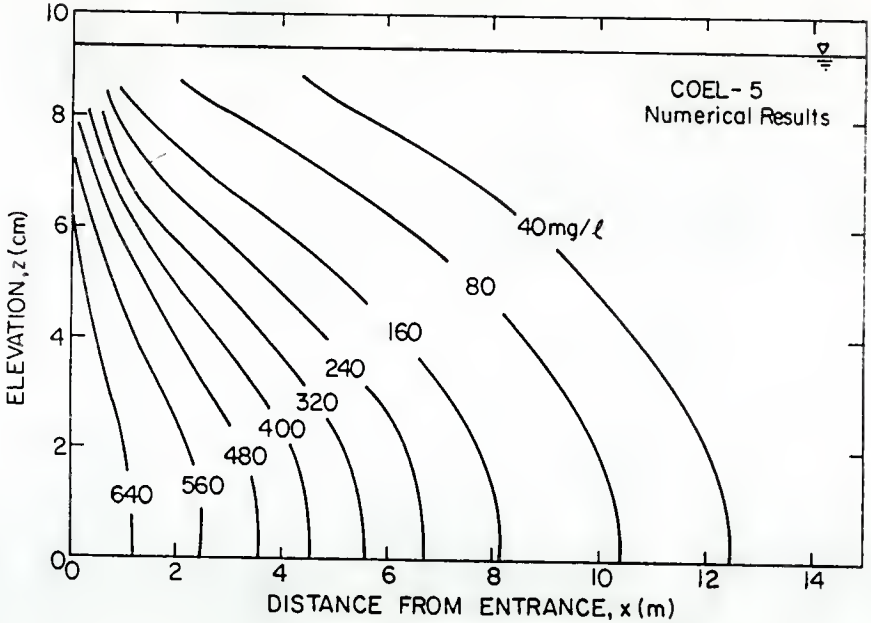

Figure 5.16. Concentration Contours at Steady State in Closed-End Channel.

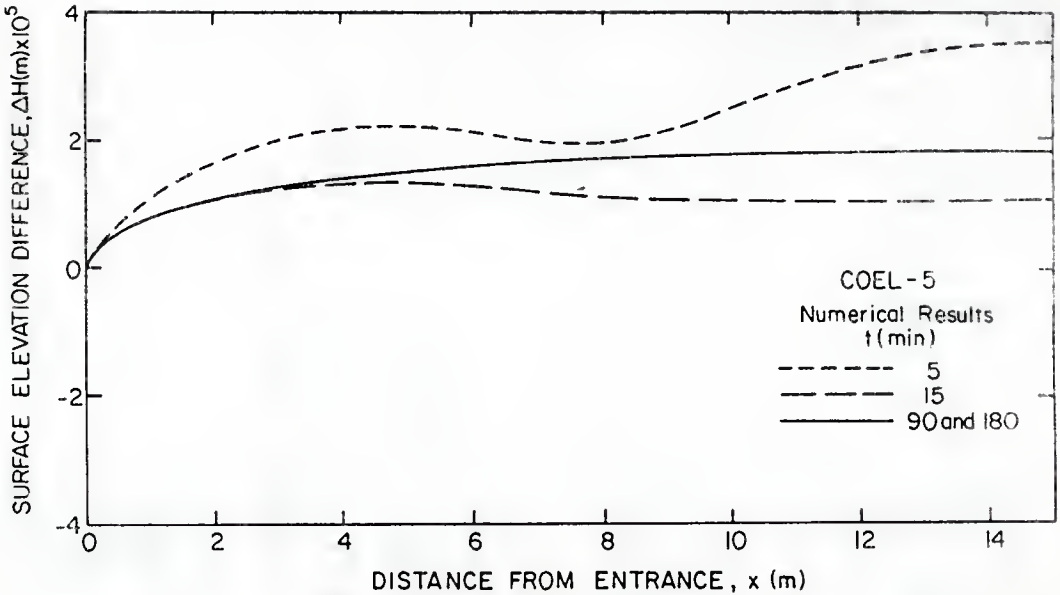

Figure 5.17. Surface Elevation Difference vs. Distance From Entrance.

The maximum rise of water surface, ΔH_{max}, can be computed according to the analytical derivation (eq.3.64) with given data on H, ρ_w, and $\rho_1(z)$. In test COEL-5, H=9.3 cm, ρ_w = 0.996836 g/cm^3, and $\rho_1(z)$, the density profile at entrance, was measured. Substituting these known values into eq.3.64, ΔH_{max} is found to be 0.024 mm, which is close to the numerical result of 0.018 mm. The good agreement between the theoretical and numerical results of ΔH_{max} confirms that a stationary sediment wedge can be established in a closed-end channel in the steady state if provided the entrance boundary conditions remain unchanged. Detailed calculation of ΔH_{max} using eq.3.64 for COEL-5 is given in Appendix C.

Distance variation of deposition rate. At about 24 hours after the end of each test, the bed deposit collected from each subsection (of selected length depending upon the total length over which measurable sediment mass was deposited) was analyzed for the deposited mass and particle size distribution. Mean sediment deposition rate was computed by dividing the deposited mass by the subsection area and effective duration. Fig.5.18 shows the calibration result of longitudinal distribution of mean sediment deposition rate. The dashed line in Fig.5.18 represents the distance variation of mean sediment deposition rate, which was obtained from test COEL-4. The solid line in Fig.5.18 shows the corresponding deposition rate distribution using the numerical model.

The verification result of the numerical model is shown in Fig.5.19. In this figure, the dashed line shows the distance variation of mean sediment deposition rate of COEL-5. Typically, there was

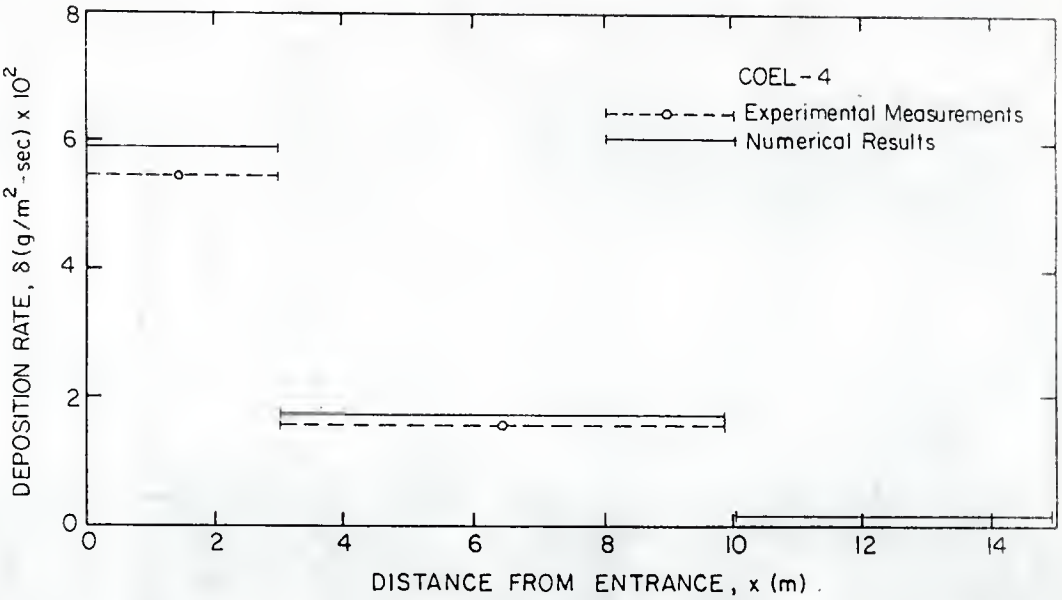

Figure 5.18. Sediment Deposition Rate vs. Distance From Entrance. (Calibration Results)

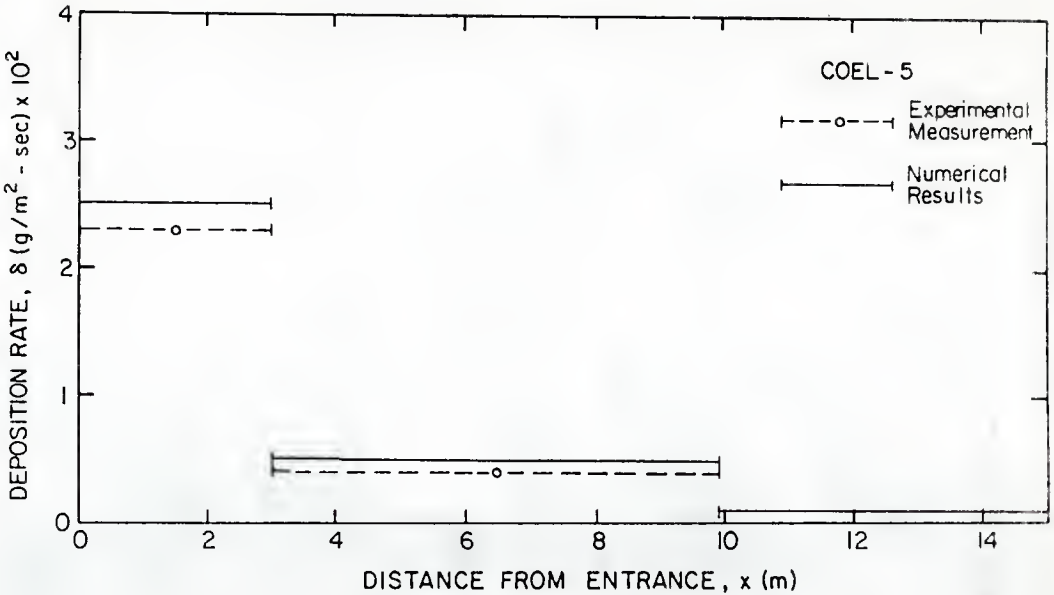

Figure 5.19. Sediment Deposition Rate vs. Distance From Entrance. (Verification Results)

relatively very high deposition in the zone inside the entrance, followed by an approximately exponential-type decrease of deposition proceeding farther along the channel. The heavy deposition in the zone near the entrance occurred when suspended particles, which were aggregated under a relatively strong turbulent flow in the main channel, moved into the relatively quiescent closed-end channel (most of them being heavier than the current could carry), and deposited on the bed almost immediately. The solid line in Fig.5.19 shows the prediction of mean sediment deposition rate of COEL-5 using the numerical model. A reasonable agreement between the numerical simulation with the experimental results is observed.

Dispersed particle size distribution of deposit. Fig.5.20 shows the distance variation of the dispersed particle size distribution of the deposit. The particle size distribution was obtained by hydrometer analysis for each bed deposit sample. The dispersed particle size shown in the figure actually represents the primary particle size, i.e., particles from which flocs are formed during aggregation. Therefore, the particle sizes in the figure should not be interpreted as the size of flocs depositing from suspension during the test.

In Fig.5.20, it can be seen that the median particle diameter of deposit decreased with distance from the entrance. Note that the deposit sample in the main channel had the maximum median particle diameter, d_m = 3.9 μm. Three particle size distribution curves shown in the figure are more or less parallel to each other. A modified sorting coefficient , which may be defined as $(d_{85}/d_m)^{1/2}$ for the present study, can be used as an index representing the degree of

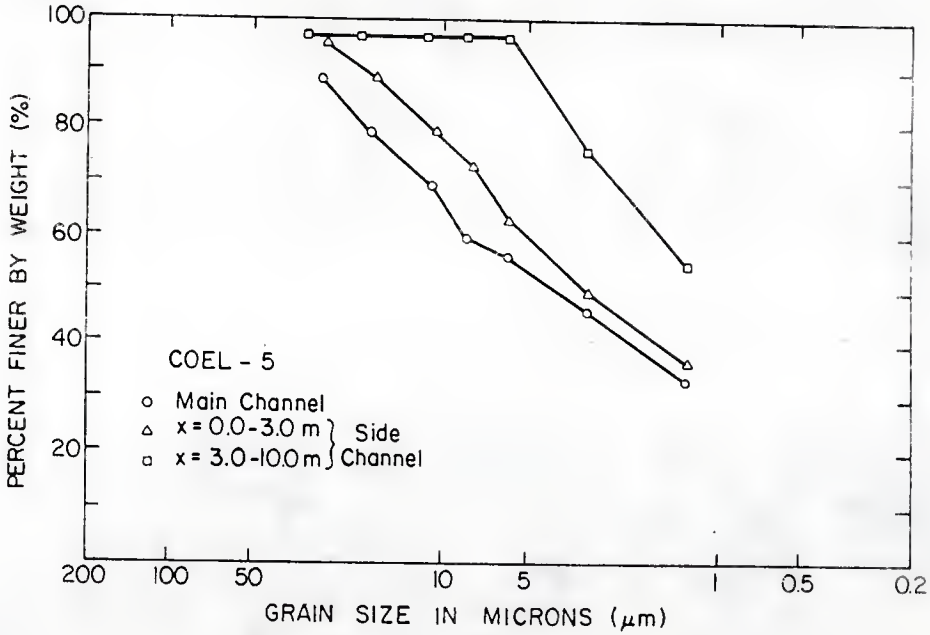

Figure 5.20. Particle Size Distributions of Deposits at Three Locations.

uniformity of particle size distribution of the deposit. The modified sorting coefficients for all three curves towards the smallest particle size shown in Fig.5.20 are 2.4, 2.2 and 1.9, respectively. This trend of relatively constant sorting coefficients was found to be generally true for all the tests. The median dispersed particle size of the deposit and the modified sorting coefficient of each particle size distribution for all COEL tests are given in Appendix D.

5.2 Characteristic Test Parameters

Tables 5.1 and 5.2 summarize the characteristic parameters for all of the tests performed at WES and COEL, respectively. The parameters included in these tables are either characteristic in the sense that they are representative factors in a physical sense of a test, or characteristic in the sense that they are frequently used for computing or normalizing the variables of interest in the subsequent sections of this chapter.

5.3 Characteristic Results

The results of steady flow tests represented in this section are considered to be characteristic because they generally include the data from WES and COEL tests. Most study results are presented in a dimensionless or normalized format, while some results, in which the characteristics of significant physical factors are examined, are presented in a dimensional format. The results of tidal effect tests conducted at COEL are included and discussed in the subsequent section.

Table 5.1. Basic Test Parameters for WES Tests.

Parameter	Test Number												
	1	2	3	4	5	6	7	8	9	10	11	12	13
$\bar{C}_1$ – Depth-mean concentration at entrance (mg/l)	44	81	166	180	532	52	182	1206	72	27[illegible]	229	348	199
$\Delta\rho_1$ – Density difference at entrance (g/cm^3)	0.000027	0.000050	0.000101	0.000110	0.000325	0.000032	0.000111	0.000737	0.000045	0.000016	0.000136	0.00020[illegible]	0.00012[illegible]
u_{f1} – Initial front speed (cm/sec)	—	0.33	0.36	0.33	0.64	—	—	0.67	0.23	—	0.28	0.34	0.40
$\bar{u}_{f1}$ – Mean of local front speeds between x=0.35-1.25 m (cm/sec)	—	0.31	0.30	0.33	0.64	—	—	0.72	0.23	—	0.28	0.34	0.35
w_{s1} – Settling velocity at entrance (cm/sec)	—	—	—	—	—	—	—	0.001	—	—	0.015	0.007[illegible]	0.025
d_{m1} – Median dispersed particle size of deposit at entrance (μm)	—	—	—	—	—	—	—	4.3	—	—	27.0	14.0	17.0
$\dot{\delta}_1$ – Mean deposition rate per unit bed area at entrance (g/m^2-min)	—	—	—	—	—	—	—	0.71	—	—	2.28	1.60	3.03
u_Δ – Densimetric velocity (cm/sec)	1.12	0.64	1.11	1.21	2.24	0.82	1.31	2.37	1.04	0.54	1.37	1.94	1.11
Re_Δ – Densimetric Reynolds number	658	442	640	768	1548	418	746	990	546	324	942	690	500
w_{s1}/u_Δ – Relative settling velocity ratio	—	—	—	—	—	—	—	0.0005	—	—	0.0139	0.0064	0.0298
M – Total dry mass of deposit in side channel during test (g)	—	—	—	—	—	—	—	220	—	—	116	117	171
S – Sediment flux into side channel through entrance (g/m^2-min)	—	—	—	—	—	—	—	220	—	—	54	102	94

Table 5.2. Basic Test Parameters for COEL Tests.

Parameter	Test Number												
	2	3	4	5	6	7	8	9	10	11	12	13	14
$\bar{C}_1$ - Depth-mean concentration at entrance (mg/l)	1657	748	724	628	250	193	269	957	870	895	202	1005	1093
$\Delta\rho_1$ - Density difference at entrance (g/cm3)	0.00101	0.00046	0.00044	0.00038	0.00015	0.00012	0.00017	0.00058	0.00053	0.00055	0.00012	0.00061	0.00067
u_{f1} - Initial front speed (cm/sec)	1.73	1.10	—	0.76	0.63	0.47	0.33	1.31	0.93	0.76	0.49	1.05	1.52
$\bar{u}_{f1}$ - Mean of local front speeds between x=0.4-2.0 m (cm/sec)	1.73	1.10	—	0.60	0.67	0.53	0.25	1.09	0.85	0.91	0.45	1.01	0.58
w_{s1} - Settling velocity at entrance (cm/sec)	0.0478	0.0302	0.0071	0.0043	0.0121	0.0189	0.0261	0.0069	—	—	0.0016	0.0081	0.0089
d_{m1} - Median dispersed particle size of deposit at entrance (μm)	1.5	2.2	2.8	2.9	12.4	13.4	14.2	1.7	—	—	9.7	1.4	1.7
δ_1 - Mean deposition rate per unit bed area at entrance (g/m^2-min)	34.2	11.0	3.2	1.4	1.4	1.6	2.3	5.0	—	—	0.1	4.3	5.9
u_Δ - Densimetric velocity (cm/sec)	3.20	2.08	2.14	1.86	1.25	1.10	1.25	2.40	2.27	2.33	1.10	2.48	2.63
Re_Δ - Densimetric Reynolds number	3830	2320	2630	1980	1490	1260	1300	2670	2390	2450	1100	2520	2740
w_{s1}/u_Δ - Relative settling velocity ratio	0.0149	0.0145	0.0033	0.0023	0.0097	0.0172	0.0208	0.0029	—	—	0.0015	0.0033	0.0034
M - Total dry mass of deposit in side channel during test (g)	1178	530	225	119	89	61	47	583	—	—	16	247	253
S - Sediment flux into side channel through entrance (g/m^2-min)	1746	772	284	116	64	56	94	494	—	—	13	200	210

5.3.1 Front Behavior

Front nose height to head height ratio. According to dimensional analysis (eq.3.2), the ratio of front nose height to head height, h_1/h_2, may be dependent upon the local head Reynolds number, $u_f h_2/\nu$, and the fraction depth, h_2/H. However, it has been pointed out by Lawson (1971) that h_1/h_2 is independent of the fraction depth h_2/H. In order to compare with previous investigation results, the effect of the local head Reynolds number, $Re_h = u_f h_2/\nu$, on h_1/h_2 is examined and shown in Fig.5.21, even though both examining dimensionless parameters $u_f h_2/\nu$ and h_1/h_2 include the same parameter h_2. The data points of present study are obtained from all COEL tests. A trend of decreasing h_1/h_2 with increasing Re_h is evident. The result indicates that with higher relative viscous force in the flow (i.e. low Re_h value), the ratio of h_1/h_2 will be higher, as expected. In Fig.5.21, in addition to the results from the present study, the data deduced from Braucher (1950), Keulegan (1958), Wood (1965), Lawson (1971), and Simpson (1972) are included. The atmospheric results obtained by Lawson (1971) show considerable scatter, and only the upper and lower bounds of the data points are shown in the figure. The consistent trend given by all of the results suggests that the relationship between h_1/h_2 and Re_h shown in this figure is valid for all types of gravity currents.

Front head height to neck height ratio. According to dimensional analysis (eq.3.5), the ratio offff front head height to neck height, h_2/h_3, may be dependent upon the local neck Reynolds number, $Re_n = u_f h_3/\nu$, the fraction depth, h_3/H, and the local relative settling velocity, w_s/u_f. Fig.5.22 represents the effects of the local neck

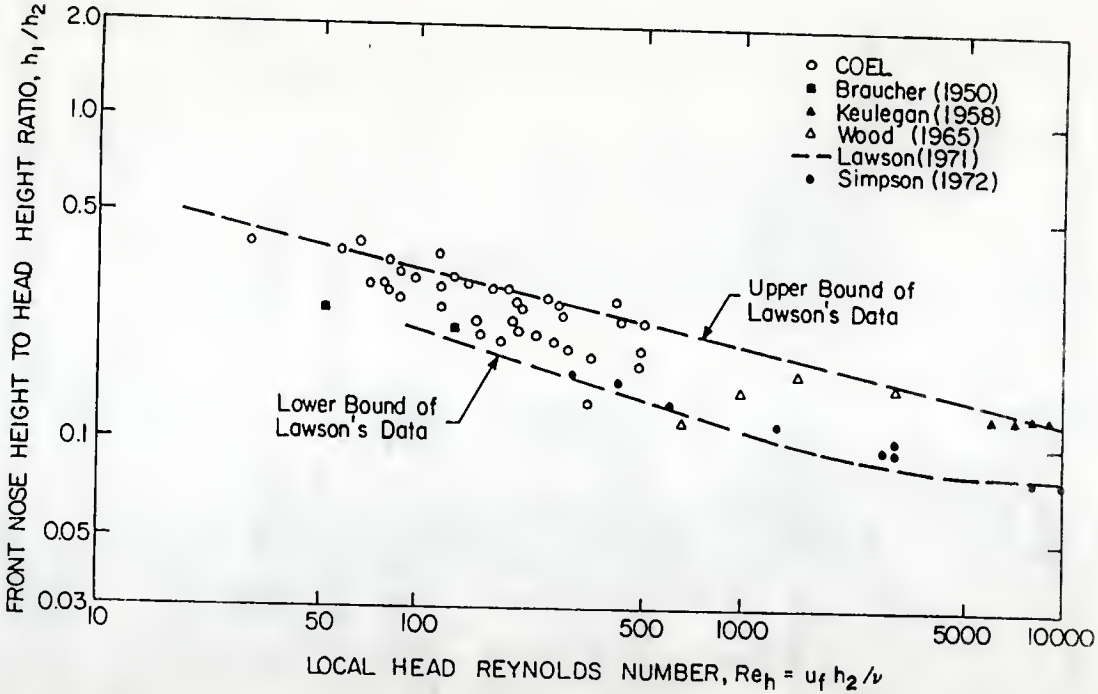

Figure 5.21. Front Nose Height to Head Height Ratio vs. Local Head Reynolds Number.

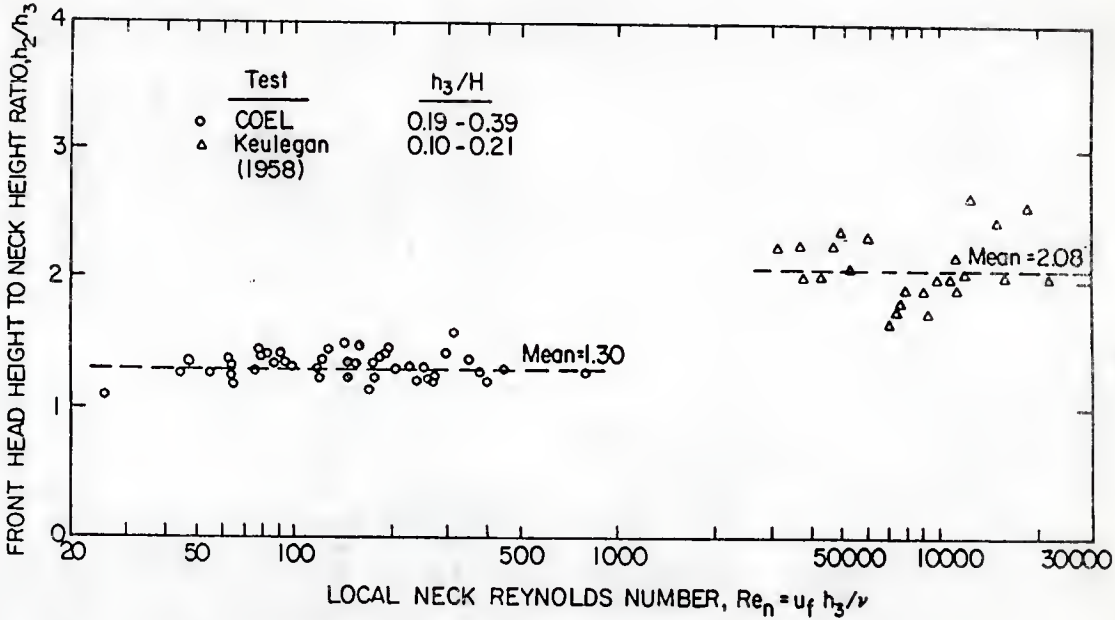

Figure 5.22. Front Head Height to Neck Height Ratio vs. Local Neck Reynolds Number.

Reynolds number, Re_n, and the fraction depth, h_3/H, on the ratio of h_2/h_3. The data under consideration here were obtained from all COEL tests over the ranges of Re_n = 20~1,000 and the fraction depth, h_3/H = 0.19~0.39. A relatively constant value of h_2/h_3, with an arithmetic mean of 1.3, is obtained over the entire Re_n range. Keulegan (1958) also found a relatively constant value of h_2/h_3, with an arithmetic mean 2.08, over ranges of Re_n = 3,000~30,000 and h_3/H = 0.1~0.21. Based on experimental observations, Simpson and Britter (1979) found that the ratio of h_2/h_3 decreases with increasing fraction depth h_3/H. Therefore, the different constant values of h_2/h_3, as shown in Figure 5.22, obtained in the present study and by Keulegan (1958), should have resulted from different fraction depth in both studies. For a constant h_3/H, the ratio of h_2/h_3 is nearly independent of the local neck Reynolds number Re_n. Finally, the relatively constant ratio of h_2/h_3 in the present study suggests h_2/h_3 is independent of the relative settling velocity, w_s/u_f.

Dimensionless initial front speed. According to the results of dimensional analysis (eq.3.8), the ratio of initial front speed to densimetric velocity, u_{f1}/u_Δ, may be dependent upon the densimetric Reynolds number, $Re_\Delta = u_\Delta H/\nu$, and the width-to-depth ratio, B/H. Fig.5.23 shows the effect of the densimetric Reynolds number, $Re_\Delta = u_\Delta H/\nu$, and the width-to-depth ratio, B/H, on the ratio of u_{f1}/u_Δ. The data points from the tests of WES and COEL are distinguished by using different symbols. The width-to-depth ratio, B/H, of WES tests varied from 2.5 to 4.6, and the B/H of COEL test was approximately 1.0. There exists a relatively great scatter of data points, which is believed to

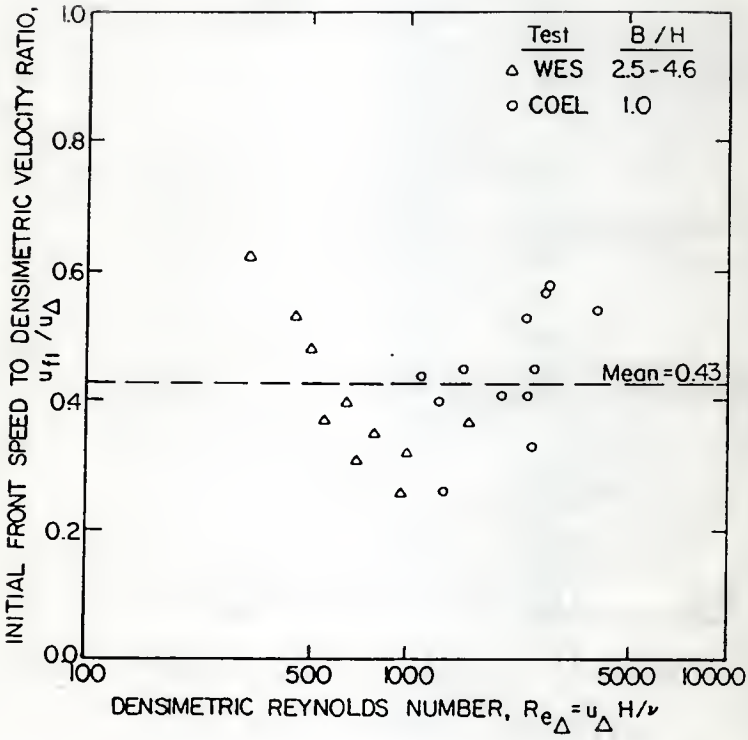

Figure 5.23. Initial Front Speed to Densimetric Velocity Ratio vs. Densimetric Reynolds Number.

be due to the presence of shear-induced gyre at the entrance. The gyre length in x direction was in the range of 0.2~0.4 m in WES tests and 0.1~0.2 m in COEL tests. The measured front speed at x = 1.0 m for WES tests, and x = 0.75 m for COEL tests was taken as the initial front speed, which was defined as the front velocity induced due to the initial density gradient. The initial front speed of each test is listed in Tables 5.1 and 5.2.

From Fig.5.23, no measurable difference between the dimensionless initial front speeds obtained from WES and from COEL tests is observed. This result may suggest that the ratio of u_{f1}/u_{Δ} is independent of the width-to-depth ratio, B/H. The arithmetic mean value of 0.43 for u_{f1}/u_{Δ} is obtained from all data points and is shown as a dashed line. Due to the relatively large data scatter, it is difficult to conclude whether or not a clear trend with respect to Re_{Δ} or B/H exists. In previous investigations on the lock exchange flow, the ratio of u_{f1}/u_{Δ} was found to be independent of the densimetric Reynolds number and the width-to-depth ratio, and equal to 0.5 from theoretical development by Yih (1965). Keulegan (1957) obtained an approximately constant experimental value of 0.46 for u_{f1}/u_{Δ} over the range of Re_{Δ} = 400~20,000 and B/H = 0.44~4.0. Comparing the ratio, u_{f1}/u_{Δ}, of 0.43 obtained from the present study with keulegan's 0.46, the agreement, notwithstanding the presence of the gyre at the entrance of the closed-end channel, suggests that the front motion beyond x = 1.0 m in the WES channel and x = 0.75 m in the COEL channel towards the closed end of the channels was mainly controlled by the turbidity gradient with the unchanged concentration source in the main channel.

Distance variation of normalized front speed. According to the result of dimensional analysis (eq.3.10), the dimensionless front speed, u_f/u_Δ, was found to be dependent upon the front position, x/H, the width-to-depth ratio, B/H, the densimetric Reynolds number, $Re_\Delta = u_\Delta H/\nu$, and relative settling velocity, w_s/u_Δ. Keulegan (1957, 1958) examined the effects of Re_Δ and B/H on the distance variation of dimensionless front speed in lock exchange flow. He proposed the following relationship between u_f/u_Δ and x/H

$$\frac{u_\Delta}{u_f} = \frac{u_\Delta}{u_{f1}} + \gamma \frac{x}{H} \qquad (5.1)$$

where the parameter γ is a function of Re_Δ and B/H. The relationship between u_f/u_Δ and x/H given in eq.5.1 for the salinity-induced density current was found not to be valid for turbidity current due to the influence of the local relative settling velocity, w_s/u_Δ. According to the results of a large-scale flume study, Barr (1967) suggested that front movement of gravity current is independent of Re_Δ if $Re_\Delta > 1{,}000$.

In the present study, a normalized front speed, $u_f/\bar{u}_{f1}$, was adopted insteady of u_f/u_Δ, while noting that the other influential dimensionless parameters should be the same. Here, $\bar{u}_{f1}$ is the average front speed over a distance 0.4-2.0 m from the entrance of the channel for COEL tests, (within x = 0.0-0.4 m, the front speed was influenced by shear-induced circulation). Also, because the settling velocity of suspension is a distance-varying parameter, the settling velocity of suspension at the entrance of the closed-end channel, w_{s1}, may be used as the reference parameter in the present and subsequent discussions.

Fig.5.24 shows the longitudinal variation of dimensionle s front speed, $u_f/\bar{u}_{f1}$, with reference to the values of w_{s1}/u_Δ and Re_Δ. It can be seen that the Re_Δ values of all five tests shown in the figure are greater than 1,000. Accordingly, the distance variation of front speed shown in Fig.5.24 is independent of Re_Δ based on Barr's finding. The curves in the figure represent smoothed trend lines, which are obtained from the corresponding dimensionless plot for each test.

Dimensional analysis indicates the relative settling velocity, w_{s1}/u_Δ, is another significant parameter influencing the front speed of turbidity current (eq.3.10). However, the parameter w_{s1}/u_Δ, a reference value at the entrance, cannot uniquely describe the local relative settling velocity, w_s/u_Δ, for different types of sediments (cohesionless and cohesive sediments), due to different compositions of the settling particles of cohesionless and cohesive sediments. Therefore, at present, the examination of the variation of curve slope with the influencing parameter, w_{s1}/u_Δ, must be considered separately for cohesive kaolinite (COEL#2, 3, and 5) and cohesionless flyash Ill (COEL#6 & 7). For each sediment, the slope of the curve in Fig.5.24 becomes steeper as the relative settling velocity increases, as could be expected. The break in slope observed in the curves of COEL#2, 3 and 6, is believed to be due to the phase shift from inertial self#similar phase to viscous self#similar phase.

<u>Local densimetric Froude number</u>. According to the dimensional analysis (eq.3.14), the local densimetric Froude number, $Fr_\Delta = u_f/[(\Delta\rho'/\rho_w)gh_3]^{1/2}$, could be expected to be a function of local neck Reynolds number, $Re_n = u_f h_3/\nu$, internal stratification of concentration

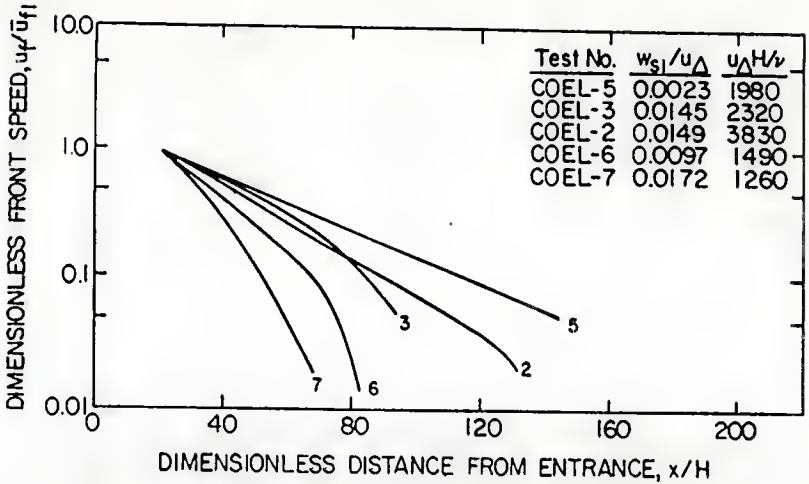

Figure 5.24. Dimensionless Front Speed vs. Dimensionless Distance From Entrance.

at the front, fraction depth, h_3/H, and width-to-depth ratio, B/H. For all COEL tests, B/H was kept approximately at 1.0. Also, the fraction depth, h_3/H, of data selected for examining the trend of Fr_Δ was in the range between 0.19~0.39, which has but little effect on Fr_Δ according to Simpson and Britter (1979). Therefore, an examination of the effect of Re_n only on Fr_Δ may be made.

Fig.5.25 shows the effect of local neck Reynolds number, $Re_n = u_f h_3/\nu$, on local densimetric Froude number, Fr_Δ. The data points shown in the figure are from all COEL tests. Although there is considerable data scatter, a trend of increasing Fr_Δ with increasing Re_n in the range of Re_n = 25~320 is evident. Keulegan (1958) investigated similar variables for experiments with a saline water front in lock exchange flow and found that $Fr_\Delta = 0.22\ Re_n^{0.25}$, for $Re_n < 400$ and $Fr_\Delta = 1.05$ for $Re_n > 400$, which is plotted as a solid line in the figure. The local densimetric Froude number in the present study is slightly lower than that obtained by Keulegan (1957) for the same Re_n value. This may be due either to the concentration stratification effect of the front, or to the use of sediment concentration at the lowest tap (at z = 0.7 cm) of the sampling location to represent the mean concentration in the front. Either of these effects will result in the smaller Fr_Δ values. In fact, the ratio of u_{f1}/u_Δ noted in Fig.5.23 is the densimetric Froude number at the entrance and is a special value of Fr_Δ, as dicussed above.

<u>Dimensionless front position</u>. Based on dimensional analysis (eq.3.16), the dimensionless front position, x_f/H, was found to be dependent upon the width-to-depth ratio, B/H, relative settling

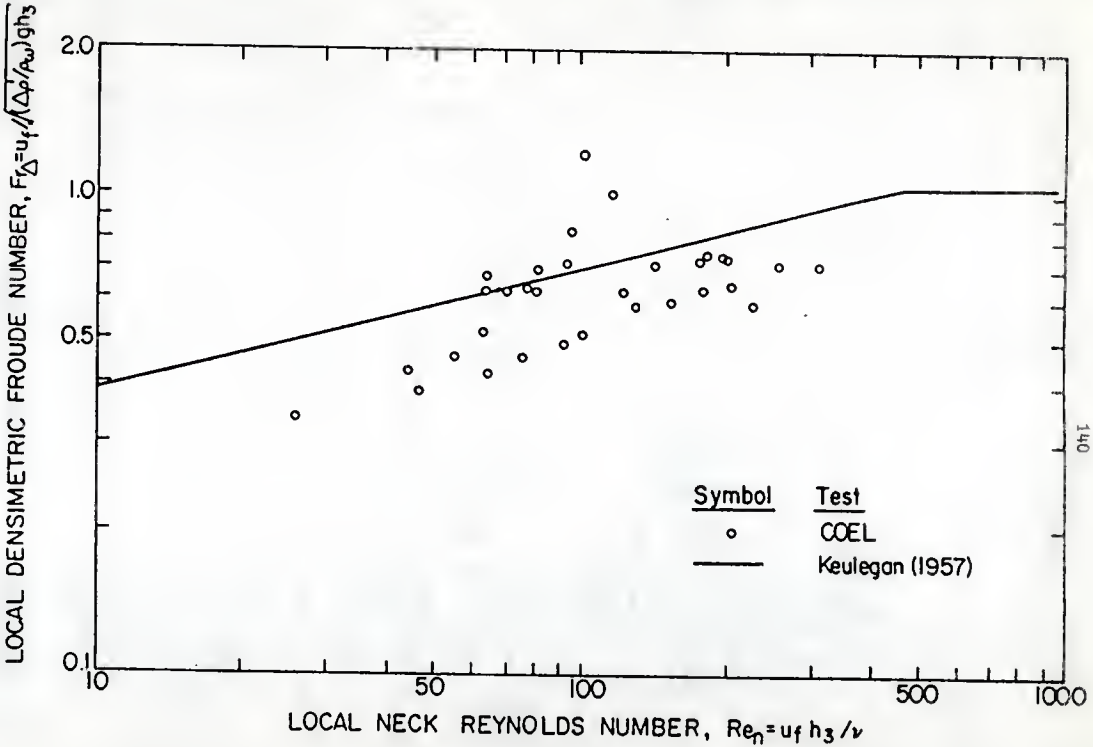

Figure 5.25. Local Densimetric Froude Number vs. Local Neck Reynolds Number.

velocity, w_s/u_Δ, densimetric Reynolds number, $Re_\Delta = u_\Delta H/\nu$, and dimensionless elapsed time, $u_\Delta t/H$. In Barr's (1967) large-scale flume study of lock exchange flow, he found that the front movement of gravity current was strongly dependent on Re_Δ when $Re_\Delta < 1{,}000$, and was almost independent of Re_Δ when $Re_\Delta > 1{,}000$. For all COEL tests, Re_Δ of each test was greater than 1,000 (which can be seen in Table 5.2). Thus the front movement for each test would be expected to be independent of Re_Δ. Also, all COEL tests had approximately the same width-to-depth ratio, B/H. Fig.5.26 shows the variation of x_f/H with $u_\Delta t/H$ for the steady COEL tests with given reference parameter, w_{s1}/u_Δ. For tests using kaolinite, (COEL#2, 3, 5, and 11), although there exists considerable data scatter, a trend curve, which comprises three distinct slopes of 1, 2/3, and 1/5, can be discerned in the figure. However, for flyash III tests (COEL# 6, 7, and 8), there are only two slopes (2/3 and 1/5) in the trend curve of each test. The scatter of data points from kaolinite tests may be due to different w_{s1}/u_Δ, but, as evident, the dependence of x_f/H versus $u_\Delta t/H$ relationship within inertial self-similar and viscous self-similar phases on w_{s1}/u_Δ seems to be slight. Also, it is observed that the duration of front propagation in the initial adjustment phase seems longer for the front with smaller w_{s1}/u_Δ than for that with higher w_{s1}/u_Δ. For flyash III tests, no initial adjustment phase (in which the front propagates at a constant speed) was found due to the high w_{s1}/u_Δ values. Also, the duration of front propagation in the inertial self-similar phase (slope = 2/3) was longer for the front with smaller w_{s1}/u_Δ than for that with greater w_{s1}/u_Δ.

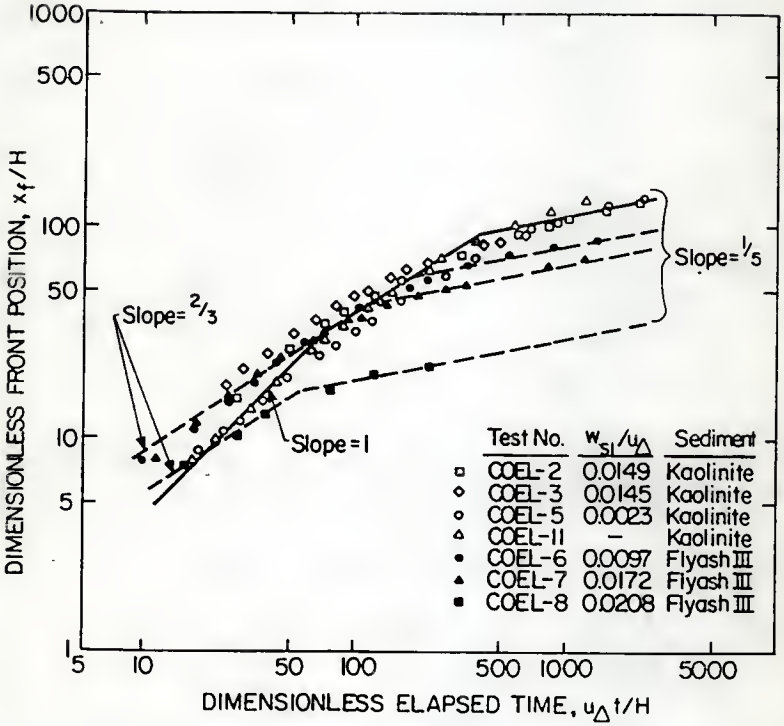

Figure 5.26. Dimensionless Front Position vs. Dimensionless Elapsed Time.

Distance variation of normalized excess front density. Fig.5.27 shows the distance variation of the normalized excess front density, $\Delta\rho'/\Delta\rho_d$, where $\Delta\rho'$ and $\Delta\rho_d$ are the excess front densities at z= 0.7 cm at each sampling location and x=2.1 m , respectively. It can be seen that $\Delta\rho'/\Delta\rho_d$ of each test decreased approximately exponentially with distance from the location of x/H = 20. It has been pointed out by Keulegan (1957) that the front dilution of salinity-induced density current through interfacial mixing is faster in lock flows having relatively small Reynolds numbers. Due to the decrease of front density of turbidity current with distance depending on both sediment deposition and interfacial mixing, the change of the curve slopes shown in Fig.5.27 may be examined with respect to two dimensionless parameters, w_{s1}/u_Δ and $u_\Delta H/\nu$. The ranges of w_{s1}/u_Δ and $u_\Delta H/\nu$ of these tests shown in the figure were 0.0023~0.0172 and 1,260~2,630, respectively. It is observed that the change of curve slope is consistent with the change of w_{s1}/u_Δ, which suggests that the dependence of the decrease of excess front density with distance on the sediment settling is greater than on interfacial mixing under the specific ranges of w_{s1}/u_Δ and $u_\Delta H/\nu$. Also, the slopes of the curves in Fig.5.27 become steeper with increasing w_{s1}/u_Δ, as one would expect.

Distance variation of mean concentration below interface. Figures 5.28(a) and (b) show the longitudinal distribution of dimensionless mean concentration below the interface for kaolinite and flyash, respectively. Test number, the dimensionless relative settling velocity, w_{s1}/u_Δ, and sediment in each test are given in the figure. In general, it can be seen that the dimensionless mean concentration

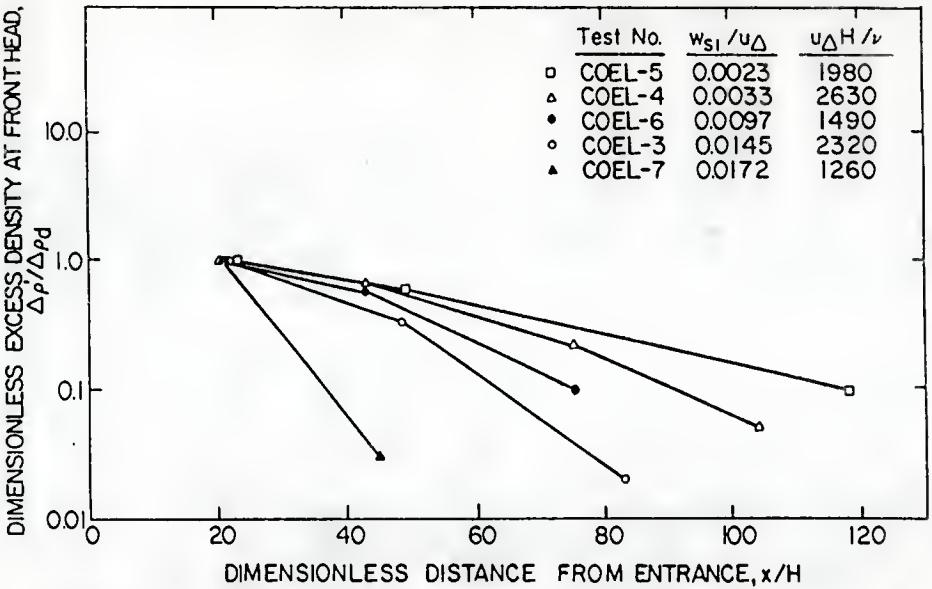

Figure 5.27. Dimensionless Excess Density at Front Head vs. Dimensionless Distance From Entrance.

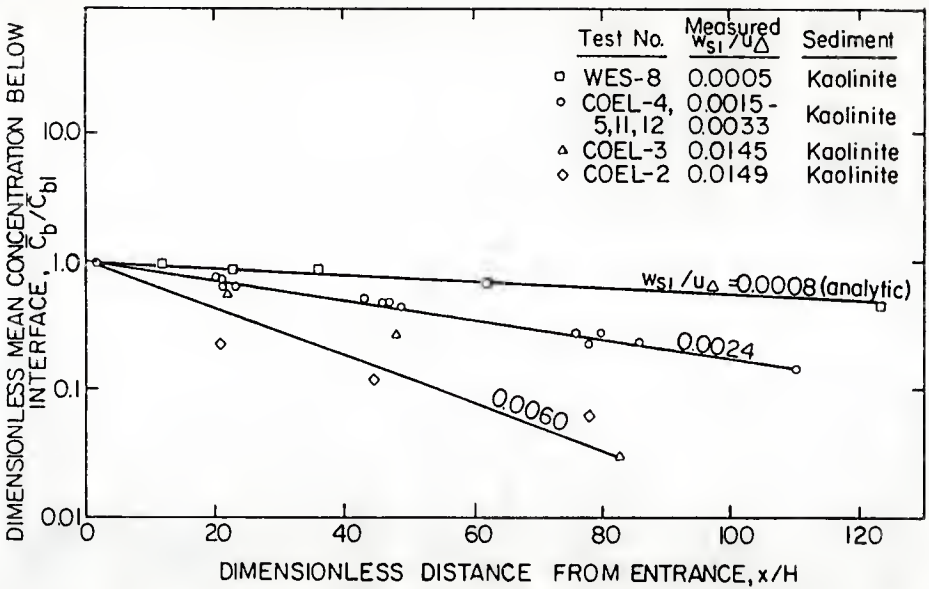

Figure 5.28.(a) Dimensionless Mean Concentration Below Interface vs. Dimensionless Distance From Entrance for Kaolinite Tests.

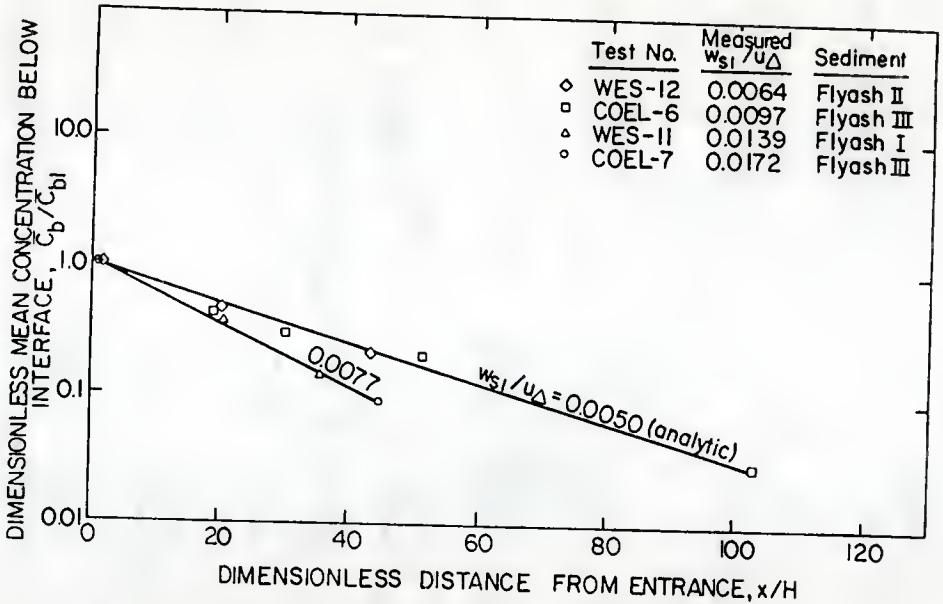

Figure 5.28.(b) Dimensionless Mean Concentration Below Interface vs. Dimensionless Distance From Entrance for Flyash Tests.

below interface, $\bar{C}_b/\bar{C}_{b_1}$, decreases exponentially with distance from the entrance. A best-fitting straight line for one test or a group of tests is given in both figures. It is observed that the slopes of these straight lines become steeper with increasing w_{s1}/u_Δ, regardless of the type of sediment. Furthermore, the numerical value given for each straight line is the value of w_{s1}/u_Δ computed by using eq.3.52 with $\beta = 7.0$ (the value used for the analytic prediction in Fig.5.15). Comparing the analytically computed w_{s1}/u_Δ value with experimental w_{s1}/u_Δ value, a good agreement is obtained for smaller experimental ratios of w_{s1}/u_Δ. However, when w_{s1}/u_Δ becomes greater, the discrepancy between the analytic and experimental results becomes larger. It can be interpreted that with high ratio of w_{s1}/u_Δ, the local relative settling velocity, w_s/u, will become much different from the ratio of relative settling velocity at the entrance, w_{s1}/u_1, where u and u_1 are the local and entrance particle velocities of the fluid, respectively. Consequently, the term of $\exp[(\beta_2-\beta_1)x]$ in eq.3.51 cannot be reduced to be $[1+(\beta_2-\beta_1)x]$, as was done, due to the significant truncation error introduced by omitting the higher order expansion terms.

5.3.2 Deposition Related Characteristics

Median column settling velocity. The results of tests for obtaining median settling velocities, w_{sm}, of raw sediments in settling columns are discussed in this section. Fig.4.6 shows that the settling velocities of flyashes I, II, III, and silica flour were not entirely independent of the initial column concentration, C, but slightly increased with increasing concentration. A similar trend was found for

Vicksburg loess. The median settling velocity of Cedar Key mud was found to be 0.001 cm/sec for C = 323-373 mg/l.

Settling column tests w re performed for kaolinite with the initial suspension concentration varing from 443 mg/l to 10,027 mg/l. Two distinct relationships for the median settling velocity with initial column concentration were found. In the range of C = 443-1,500 mg/l, w_{sm} of kaolinite increased with increasing C, according to

$$w_{sm} = 0.0001\ C^{0.79} \qquad (5.2)$$

where w_{sm} is in cm/sec, and C is in mg/l. With reference to eq.2.4, eq.5.2 indicates $k_1 = 0.0001$, and $n_1 = 0.79$. In the range of C = 1,500-10,027 mg/l, w_{sm} remained unchanged, equal to 0.033 cm/sec.

Longitudinal variation of suspended sediment settling velocity. Figs.5.29(a) and (b) show the distance distribution of dimensionless settling velocity of suspended sediment, w_s/w_{s1}. Because of the complexity involved in directly measuring the settling velocity of settling flocs (for cohesive sediment), an indirect method was adopted to compute the settling velocity using the mass balance equation, i.e. eq.2.6. For all WES and COEL experimental tests, the ratio τ_b/τ_{cd} was on the order of 0.01 due to the small velocity in the closed-end channel. Therefore, the probability of a particle sticking to the bed, $1-\tau_b/\tau_{cd}$, in the mass balance equation was assumed to be unity. Also, the deposition rate per unit bed area, dm/dt, can be computed using the deposited mass divided by the effective duration (i.e. the period from the passage of the front at the location of interest until the end of the test), and collection area. In addition, the spatially interpo-

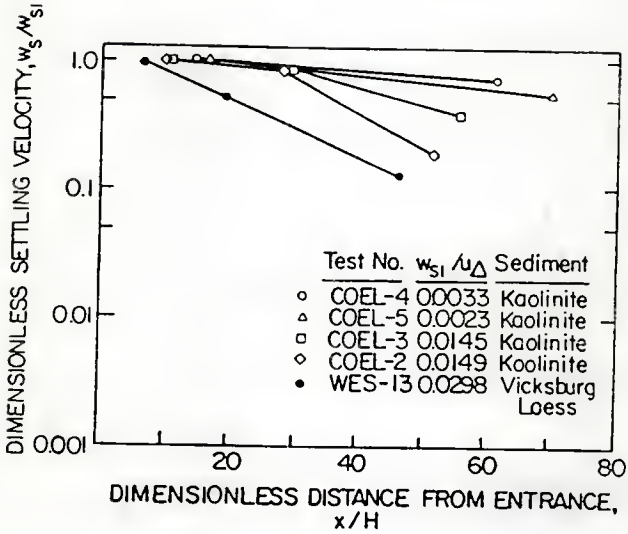

Figure 5.29.(a) Dimensionless Settling Velocity vs. Dimensionless Distance From Entrance for Cohesive Sediments.

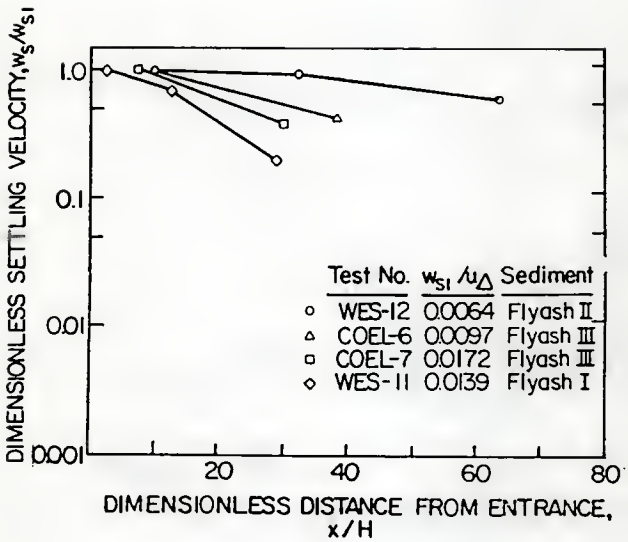

Figure 5.29.(b) Dimensionless Settling Velocity vs. Dimensionless Distance From Entrance for Cohesionless Sediments.

lated mean concentration below interface, $\bar{C}_b$, was used for C in the mass balance equation. The settling velocity of suspended sediment was calculated under these assumptions.

Due to the distinct characteristics of cohesionless and cohesive sediments, examination of the distance variation of dimensionless settling velocity for cohesive sediment, which included kaolinite and Vicksburg loess, may be considered separately from cohesionless sediment, which included flyash I, II, and III. As seen in Figs.5.29 (a) and (b), in general, w_s/w_{s1} decreased with increasing x/H. In addition, the slope of the curve may be related to w_{s1}/u_Δ, which was found to be a significant parameter for all of the deposition-related characteristics. From Figs.5.29(a) and (b), it is observed that for both cohesive and cohesionless sediments, the slope of the lines became steeper with increasing w_{s1}/u_Δ.

Longitudinal variation of dispersed particle size of deposit. Fig.5.30 shows the distance variation of dimensionless median dispersed particle size of the deposit, d_m/d_{m1}, where d_{m1} is the median dispersed particle size of the deposit at the entrance. As mentioned in section 5.1.3, the dispersed particle size represents the primary particle size from which flocs are formed. There is a trend for d_m/d_{m1} to decrease with distance from the entrance.

The dependence of the rate of the decrease of d_m/d_{m_1} with distance on w_{s1}/u_Δ may be examined using the results of COEL test. According to the plot, the rate of decrease of d_m/d_{m_1} with distance is approximately the same for all of four kaolinite tests, but is different from two other tests with flyash III. In order to explain why d_m/d_{m_1} decreased

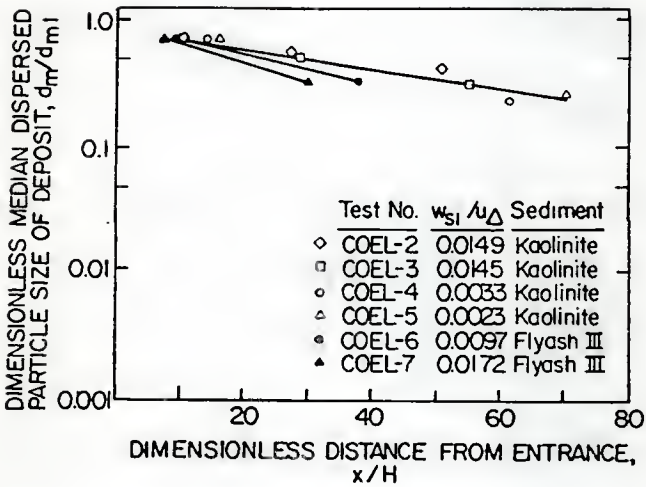

Figure 5.30. Dimensionless Median Dispersed Particle Size of Deposit vs. Dimensionless Distance From Entrance.

with distance at the same rate for all four kaolinite tests, one significant feature of cohesive sediment must be noted; in the case of a cohesive sediment such as kaolinite, the settling units or flocs are composed of primary particles. Oftentimes, faster settling flocs are composed of finer particles (Dixit et al., 1982). On the other hand weakly aggregated flocs composed of larger primary particles tend to have lower settling velocities and travel further than flocs composed of finer particles. There is therefore no unique correlation between the settling velocity of a floc and the primary constitutive particles.

For cohesionless sediment, such as flyash III, no significant particle aggregation is involved. Accordingly, the trend of the slope of the curves in Fig.5.30 becoming steeper with increasing w_{s1}/u_{Δ} could be expected.

<u>Variations of settling velocity and dispersed particle size with main channel concentration</u>. Fig.5.31 shows the variations of sediment settling velocity, w_s, and median dispersed particle size of deposit, d_m (mean values for all deposits located in the region x = 0.08-3.0 m in the closed-end channel), with the corresponding mean main channel concentration, $\overline{C}_o$. The purpose of this figure is to examine the influence of main channel concentration on settling velocity and dispersed particle size at the area near the entrance. It is believed that most of the deposited flocs (for cohesive sediment) in the entrance area were formed in the main channel under turbulent conditions, and deposited immediately when they moved into the closed-end channel, where the flow velocity was much lower.

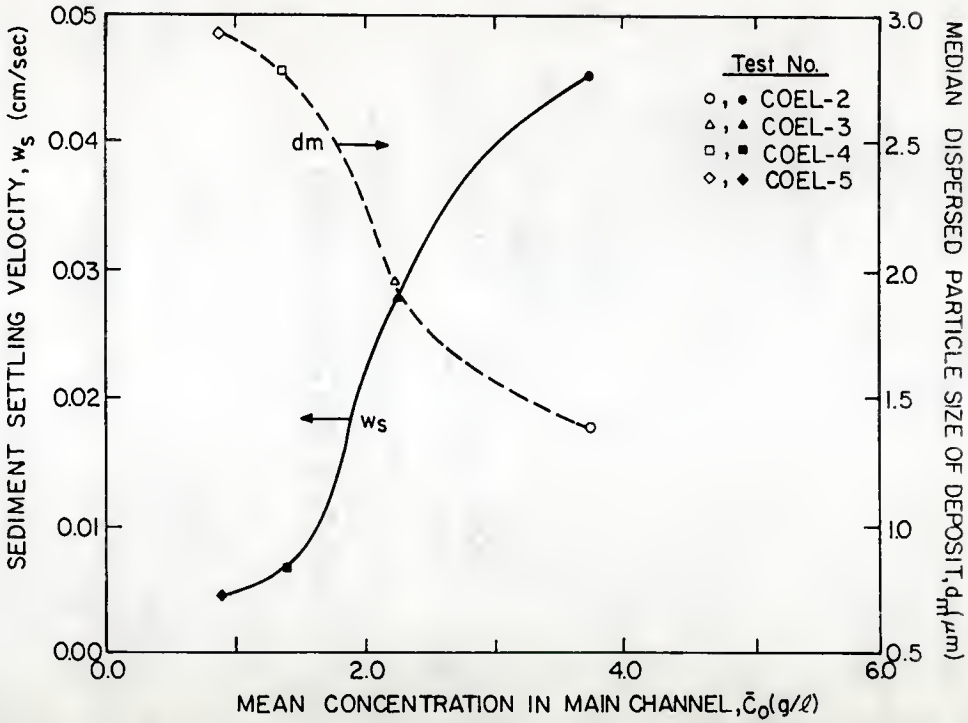

Figure 5.31 Settling Velocity and Median Dispersed Particle Size vs. Main Channel Concentration

It can be seen from Fig.5.31 that w_s increased rapidly with increasing $\bar{C}_o$ as $\bar{C}_o > 1,400$ mg/l, while d_m decreased with increasing $\bar{C}_o$. Since one would expect that greater aggregation of cohesive sediment would occur under conditions of higher concentration and turbulent flow, it is not surprising that Fig.5.31 shows that the flocs formed under higher suspension concentration possessed higher settling velocities and were composed of smaller primary particles, as was also noted previously.

Critical deposition shear stress. Table 5.3 gives values of the critical deposition shear stress, τ_{cd}, of kaolinite. τ_{cd} is defined as the shear stress below which all initially suspended sediment eventually deposits. The purpose of computing τ_{cd} of kaolinite in the present study was to explore the depositional property of kaolinite, and to provide an input value required for the application of the mathematical model. The determination of τ_{cd} was based on the mass balance equation with measured deposition rate, dm/dt, mean concentration, $\bar{C}_o$, settling velocity, w_s, and mean flow velocity, $\bar{u}_o$, in the main channel. Here, the settling velocities of suspended sediments in main channel are assumed to be the same as the ones obtained by settling column analysis, even though the flow conditions were quite different in the two cases. The bed shear stress, τ_b, was calculated using the formula, $\tau_b = f_o \rho_w \bar{u}_o^2/8$, where the friction factor, f_o, was determined using a Moody diagram (Daily & Harleman, 1966) based on the Reynolds number, $4R\bar{u}_o/\nu$, where R is the hydraulic radius. The mean τ_{cd} of kaolinite from tests COEL-3, 5, 9, 13, and 14 is equal to 0.13 N/m^2, which compares well with 0.15 N/m^2 obtained by Mehta (1973).

Table 5.3 Critical Deposition Shear Stress of Kaolinite

Test Number (COEL)	3	5	9	13	14
dm/dt $(g/cm^2\text{-}sec) \times 10^5$	2.8	1.1	1.9	1.4	1.7
$\overline{C}_o$ (mg/l)	2,248	908	1,926	1,433	1,692
w_{sm} (cm/sec)	0.032	0.022	0.032	0.031	0.032
τ_b (N/m^2)	0.049	0.072	0.075	0.110	0.097
τ_b/τ_{cd}	0.61	0.45	0.69	0.68	0.69
τ_{cd} (N/m^2)	0.08	0.16	0.11	0.16	0.14

Distance variation of flocculation factor. Fig.5.32 shows the longitudinal distribution of the flocculation factor, F, defined as the ratio of the median settling velocity of the flocs, w_s, to the settling velocity of the primary particle sizes, w_{sd}, from which the flocs are formed. The data represented in the figure include all steady COEL tests for kaolinite except COEL-11, in which deposition-related data were not obtained. It can be seen from this figure that three distinct trends of flocculation factor varying with distance appear and correspond to different suspension concentrations in the main channel. The reason for increasing flocculation factor (in COEL-2 & 3) between x = 0.0-1.5 m is that most suspended flocs from the main channel were deposited at x = 1.5-2.0 m by the convective transport of the shear-induced gyre at the entrance. It was previously mentioned that deposits of cohesive sediment can consist of two parts: individual or

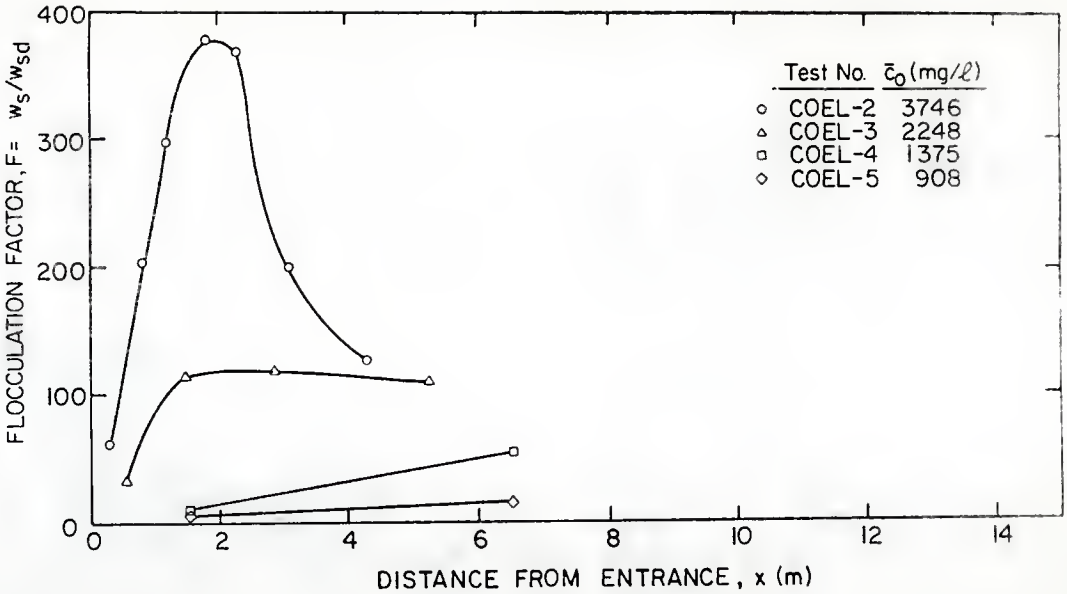

Figure 5.32. Flocculation Factor vs. Distance From Entrance.

weakly aggregated particles and relatively large flocs formed by finer primary particles. The peak of the COEL-2 curve indicates that the particles with a relatively high degree of aggregation, formed in main channel under high suspension concentration, dominated the deposit at x = 1.5~2.0 m. Beyond this location, F could be expected to decrease with x because most large flocs had already settled out. The relatively constant F values between x = 1.5~5.2 m observed in the curve of COEL-3 suggest that at moderate main channel concentrations, approximately the same amounts of individual particles and flocs had deposited in the closed-end channel. At low concentrations in the main channel (COEL-4 & 5), small F values at x = 1.5 m indicate that the larger (weakly aggregated) individual particles dominated the deposit, and thereafter, F increased gradually with increasing x due to the settling of the flocs with a lower degree of aggregation, which were formed in the main channel under low suspension concentration.

Flocculation factor variation with dispersed particle size. Fig.5.33 shows the flocculation factor variation with median dispersed particle size, which was obtained from both the WES and COEL tests. It can be seen from the figure that, in general, F increased with decreasing median dispersed particle size, d_m. Note that for kaolinite tests, higher suspension concentration in the main channel, $\overline{C}_o$, seems to have generated flocs with larger flocculation factor formed by the same d_m. The flocculation factors of flyash I, flyash II, and flyash III are observed to be very low, indicating very weak cohesion. Also, the low flocculation factor for Vicksburg loess was found under low suspension concentration. There is a reasonable agreement with the

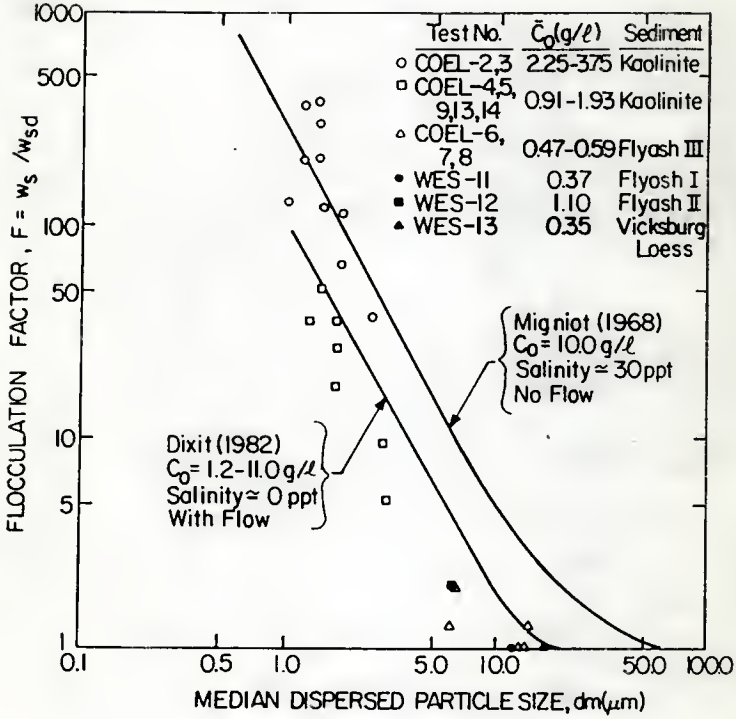

Figure 5.33. Flocculation Factor vs. Median Dispersed Particle Size.

results obtained by Migniot (1968) and Dixit (1982), notwithstanding the somewhat different test conditions among the three studies.

Longitudinal variation of deposition rate. According to dimensional analysis (eq.3.19), the normalized deposition rate, δ/δ_1, was found to be dependent upon the dimensionless distance, x/H, the width-to-depth ratio, B/H, the relative settling velocity, w_s/u_Δ, and the density difference at the entrance, $\Delta\rho_1/\rho_w$. Due to insufficient data for examining the effects of all of these dimensionless parameters on δ/δ_1, only the effect of the major influencing parameter, w_{s1}/u_Δ, on δ/δ_1 is examined in this section by assuming that the dependence of δ/δ_1 on B/H and on $\Delta\rho_1/\rho_w$ are relatively small under the specific test conditions.

Figs.5.34(a) and (b) show the longitudinal variation δ/δ_1 for cohesive and cohesionless sediments, respectively. In each test, it is observed that δ/δ_1 decreased with increasing x/H from the entrance. Once again, the relative settling velocity parameter, w_{s1}/u_Δ, should be important for examining the slopes of the curves (i.e. rate of decrease of dimensionless deposition rate in the x direction). Due to the deposited samples being collected at different locations near the entrance for each test, it is somewhat difficult to examine the slopes of the curves on a comparative basis, since these start from different locations. Yet, in general, the trend of the slope of the curves becoming steeper with increasing w_{s1}/u_Δ can be easily seen from both figures. Note that the slope trends of the curves for δ/δ_1 are similar to those of curves shown in Figs.5.29(a) and (b) for the dimensionless settling velocity.

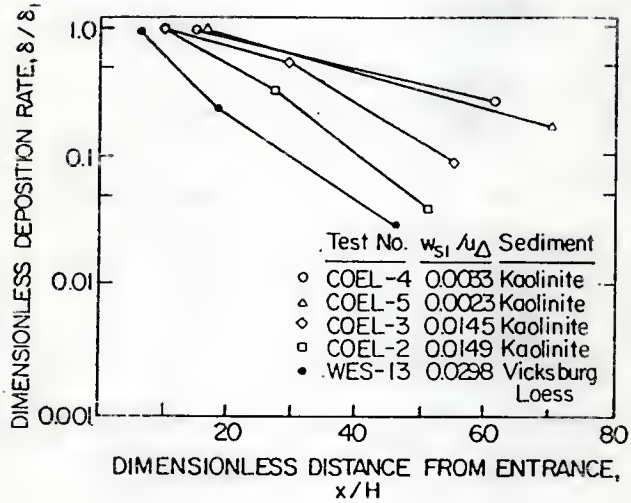

Figure 5.34.(a) Dimensionless Deposition Rate vs. Dimensionless Distance From Entrance for Cohesive Sediments.

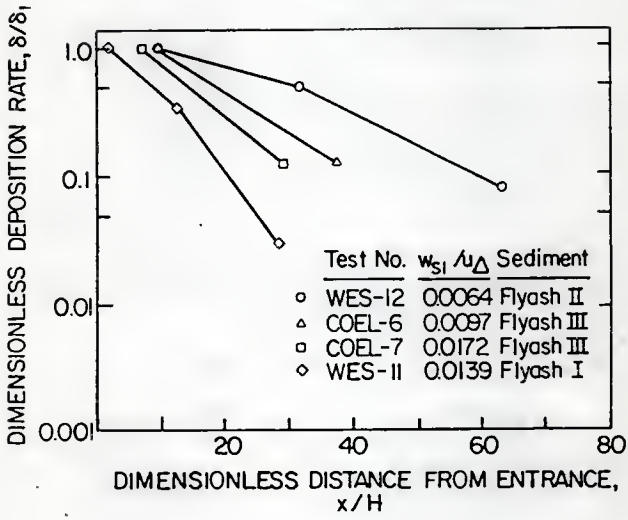

Figure 5.34.(b) Dimensionless Deposition Rate vs. Dimensionless Distance From Entrance for Cohesionless Sediments.

Relationship between sediment flux and suspension concentration at entrance. Fig.5.35 presents the results of an attempt to provide a relationship of some practical value for predicting sedimentation in closed-end channels of the type examined in the present study under similar conditions. The data points shown in the figure are obtained from all st eady tests at WES and COEL except COEL-11, in which no deposited sediment samples were obtained. The mean sediment flux, S, was computed by dividing the total deposit mass by test duration and the area of the lower half cross section at entrance. The analytical derivation of eq.3.61 provides a way to predict the sediment flux through the lower layer into the channel, given the boundary concentration, $\overline{C}_1$, at the entrance, water depth H, and specific gravity of sediment G_s. Arithmetic mean values of H and G_s were computed for 12 tests included in Fig.5.35 and are equal to 8.8 cm and 2.55, respectively. Also, an experimental result that the surface outflow velocity at the entrance of the closed-end channel at steady state is about 30% lower than the initial front speed, found by Gole et al. (1973), is used to obtain α value (α = 0.35) in eq.3.61. Accordingly, eq.3.61 can be reduced to

$$S = 0.015\ \overline{C}_1^{1.5} \qquad (5.3)$$

where the sediment flux, S, is in g/m^2-minute and $\overline{C}_1$ is the depth-averaged concentration at the entrance in mg/l. The straight line representing eq.5.3 is plotted against corresponding data points on log-log axes, and shows a good agreement between prediction and the experimental results.

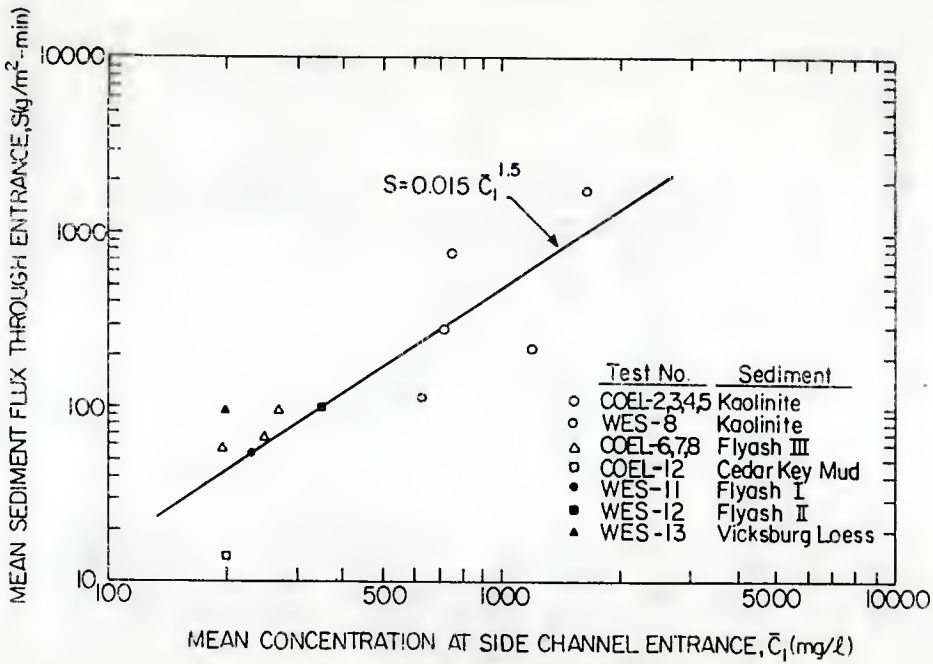

Figure 5.35. Mean Sediment Flux into the Closed-end Channel Through Entrance vs. Mean Sediment Concentration at Entrance.

Equation 3.61 should be applicable not only for prototype closed-end channels, but also for prototype open-ended ones, as long as the flow field in the channel is quiescent and the sediment transport mechanism is dominated by a turbidity gradient. Nonetheless, for basins with short lengths, such as a marina, all suspended sediment transported by turbidity current may not deposit before it reaches the closed end of the basin. As a consequence, a turbidity current reflected from the closed end will occur. Such reflected turbidity fronts propagating towards the entrance were observed during the tests performed at WES. For that particular case, the use of eq.3.61 to predict the sediment flux into a basin needs further study.

5.4 Results of Tidal Effect Tests

In coastal regions, tidal motion is an important factor in the transport of fluid and sediment. The study of tidal effect on turbidity current and associated sediment transport noted in this section is preliminary, as it is based on only two tests (COEL-9 & 10) and one reference test (COEL-11), i.e. test without imposed water surface variation in the main channel. The effects of water surface variation on front speed of turbidity current, phases of front propagation, and mean sediment concentration below the interface are described. An example of the contribution of tide-induced deposition in a closed-end channel, relative to contribution from turbidity current-induced deposition, is given.

5.4.1 Longitudinal Variation of Front Speed

Figure 5.36 shows the distance variation of the dimensionless front speed in the two tidal effect tests and in the reference test.

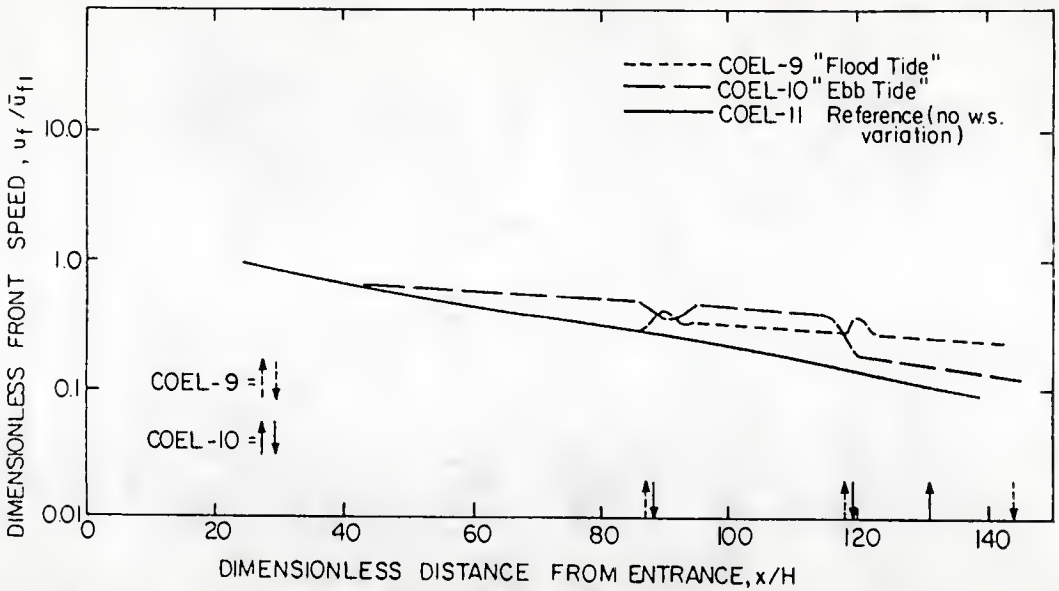

Figure 5.36. Dimensionless Front Speed vs. Dimensionless Distance From Entrance for Tide Effect Tests.

Arrows shown along the horizontal axis indicate the direction of water surface variation imposed in the headbay (upward and downward arrows of dashed line indicate, respectively, rise and fall of water surface in test COEL#9; while the corresponding arrows of the solid line indicate, respectively, rise and fall of water surface in COEL#10), and the approximate front position at the time of water surface change in the headbay. The imposed variation of water surface with the elapsed time during the tests can be seen in Fig.4.11.

From the curves of COEL#9 and 10, the response on front speed to the first pair of changes in water level can be seen. It appears that at the distance of x/H = 85#95, the effect of an increase of water level in COEL#9 was a lessening of the slope of the curve; however, no effect on the curve slope of COEL#10 by decreasing water level is observed. In the range of x/H = 115#125, no effect on the curve slope of COEL#9 by increasing water level is observed; however the effect of a decrease of water level in COEL#10 was a steepening of the curve slope. A comparison between the curves of COEL#9 and 11 reveals that an increase of water level in the main channel seems to have prevented the front speed from decreasing. However, due to a lower main channel concentration in COEL#10, its dimensionless front speed was higher than that of reference test COEL#11 before any change of water level was imposed. Therefore, it is probably unjustified to make any comparison of the effect of imposed water surface variation for this case, with the reference test.

5.4.2 Front Position Variation with Elapsed Time

As shown in Fig.5.26, three characteristic phases (i.e. initial adjustment phase, inertial self-similar phase, and viscous self-similar phase) were found in the front propagation in the steady COEL tests. The effect of water surface variation on the phase change during front propagation may be examined. Fig.5.37 shows the variation of dimensionless front position, x_f/H, with dimensionless elapsed time, $u_\Delta t/H$, for two tidal effect tests and for the reference test. Again, the arrows shown at the horizontal axis indicate the direction of water surface variation imposed in the headbay and the corresponding dimensionless elapsed time at the time of change of water level in the headbay.

It can be seen from Fig.5.37 that the front motion in all three tests started from the initial adjustment phase (slope = 1), and entered the inertial self-similar phase (slope = 2/3) at approximately the same time of $u_\Delta t/H = 57$. Subsequently, the curve slope of reference test COEL#11 started decreasing from the slope of 2/3 at $u_\Delta t/H = 400$, and eventually became 1/5 (the slope for viscous self-similar phase) at $u_\Delta t/H = 850$. However, for both the tidal effect tests, in which the water surface variation imposed in the headbay started at about $u_\Delta t/H = 330$, the curve slope of COEL#10 ("ebb tide") did not decrease from the inertial self-similar phase until $u_\Delta t/H = 580$. However, the front in COEL#9 ("flood tide") still propagated within the inertial self-similar phase when it reached the closed end (at $u_\Delta t/H = 800$). Based on these observations, a preliminary conclusion can be drawn that water surface variation in main channel, regardless of

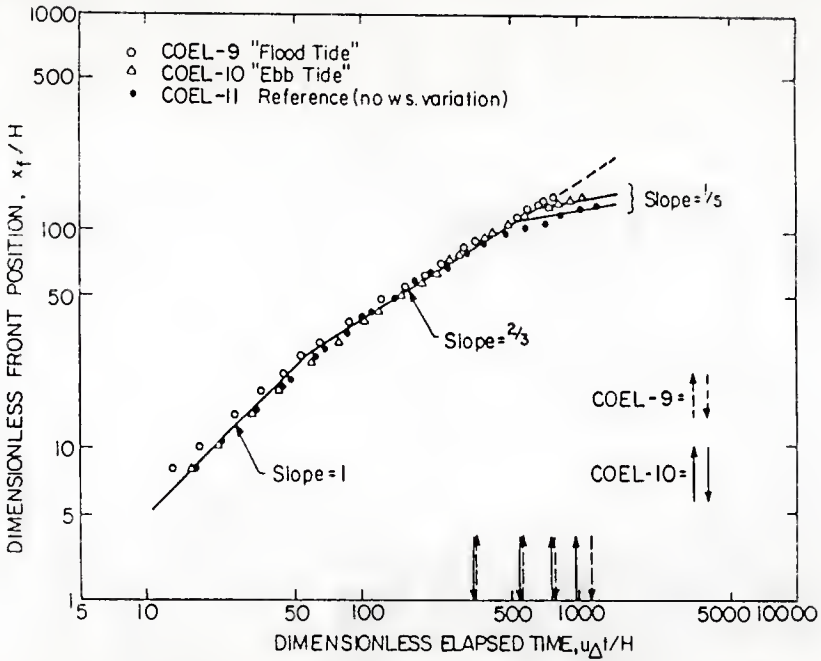

Figure 5.37. Dimensionless Front Position vs. Dimensionless Elapsed Time for Tide Effect Tests.

increasing or decreasing water level, will extend the duration of front propagation within the inertial self-similar phase. The reason may be that the oscillation in the flow, generated by water surface change, provides extra inertial force to the propagating front.

5.4.3 Longitudinal Variation of Mean Concentration below Interface

Fig.5.38 shows the distance variation of dimensionless mean concentration below interface for the two tidal effect tests and the reference test. It can be seen that the imposed water surface variations in both tests had no significant effect on the longitudinal distribution of mean concentration below the interface at steady state. Possibly, there were also no significant effects on the amount of sediment deposited in the channel.

Note that the changes of water surface in COEL-9 and 10 are not a realistic simulation of astronomical tide. Astronomical tide simulation requires a periodic variation of water surface, with tidal amplitude and period scaled appropriately to represent similarity with prototype tide. To evaluate the tidal effect on the mechanics of front propagation and associated sediment deposition, further investigation is required.

5.4.4 Tide-Induced to Turbidity Current-Induced Deposition Ratio

In section 3.3.5, the relationship between tide-induced and turbidity current-induced deposition in closed-end channels has been considered (eq.3.67). According to this relationship, the ratio of tide-induced to turbidity current-induced deposition mass, M_T/M_D, can be obtained if the excess density at the channel entrance, $\Delta\rho_1/\rho_w$,

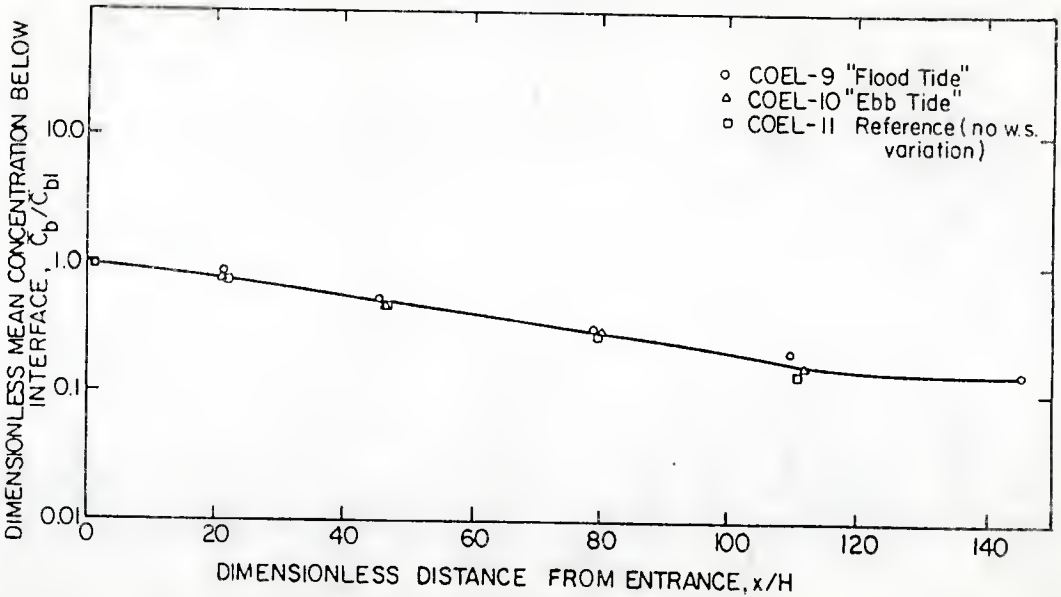

Figure 5.38. Dimensionless Mean Concentration Below Interface vs. Dimensionless Distance From Entrance for Tide Effect Tests.

relative tidal amplitude, a_o/H, and channel length to tidal wave length ratio, L/L', are known.

In order to examine the deposition contributed by tidal motions as percentage of that by turbidity current in prototype scale channels and tidal conditions, one typical example is sufficient. Consider a 1,000 m long and 5 m deep closed-end channel, under the influence of tide having a 0.5 m amplitude and a 12 hours period, with a relative density gradient at the entrance, $\Delta\rho_1/\rho_w = 0.001$. The local tidal wave length can be computed as $L' = (gH)^{1/2}T = 302{,}400$ m. Hence the tide-induced to turbidity current-induced deposition mass ratio is

$$\frac{M_T}{M_D} = 11.42 \left(\frac{\Delta\rho_1}{\rho_w}\right)^{-1/2} \left(\frac{a_o}{H}\right) \left(\frac{L}{L'}\right) = 0.12 \qquad (5.4)$$

The result indicates the deposition mass induced by tidal motions is approximately 12% of that induced by turbidity currents. It can be seen from the formula that the contribution of tide-induced deposition becomes important when the area of water suface in the channel and tidal range are large, or, the channel is shallow and the density gradient is small.

CHAPTER 6
CONCLUSIONS AND RECOMMENDATIONS

6.1 Summary of Investigation

In order to explore the distinction between low Reynolds number front behavior of a turbidity current and a non-settling gravity current (e.g. salinity or temperature-induced density current), two sets of laboratory experiments were conducted in specially designed flume systems. Characteristic results are described. These results have been discussed on the basis of significant dimensionless parameters obtained from dimensional analyses. Discussed physical aspects of front behavior include front nose height to head height ratio, front head height to neck height ratio, dimensionless initial front speed, dimensionless instantaneous front speed, local densimetric Froude number, dimensionless front position, dimensionless excess front density, and, most important, relative settling velocity.

Typical results of the flow regime in the channel, obtained by simulation using a specially developed and calibrated numerical model, include time variation of horizontal velocity, and time and distance variations of vertical velocity profile. An attempt at deriving analytical solutions for the horizontal velocity profile at steady state was made. Also, typical results related to suspension concentration obtained from both experimental measurement and numerical model simulation are given. These include time variation of suspension

concentration, and distance variation of the vertical concentration profile. The longitudinal distribution of mean concentration below the interface at steady state was examined using experimental, numerical, and analytical results.

Deposition-related characteristic results, which were mainly obtained from experimental measurements, include the longitudinal distributions of settling velocity, median dispersed particle diameter, flocculation factor, and deposition rate. Formulations for estimating turbidity driven sediment flux into the channel, and the ratio of tide-induced to turbidity current-induced deposition have been discussed.

Finally, the effect of water surface variations in the main channel on instantaneous front speed, duration of each characteristic phase in front propagation, and mean concentration below the interface were examined.

6.2 Conclusions

The groupings of dimensionless parameters derived from dimensional analysis for front nose height, front head height, initial front speed, instantaneous front speed, front position, and deposition rate in section 3.1 have provided an appropriate framework for discussing and presenting experimental results. Also, some results of dimensionless analysis have been confirmed by comparing present experimental results with those obtained by other investigators.

In accordance with calibration and verification results of the developed numerical model, this two-dimensional, explicit, finite-difference model is shown to have a good capability of simulating flow

regime, concentration distribution, and sediment deposition in a closed-end channel. In the model, the effect of cohesive sediment aggregation, buoyancy effect due to fluid stratification, and tidal effect have been taken into account.

Experimental facilities, specially designed for keeping flow velocity and suspension concentration in the main channel unchanged throughout a test, effectively established a stable flow regime and kept concentration constant for finer sediments (e.g. kaolinite). For sediments having high settling velocities (e.g. flyash I), mixers in the slurry mixing tanks were not capable of preventing the material from settling in the tank. It should be noted that turbulent flows in the main channel affect the behavior of turbidity current in the closed-end channel by changing the vertical concentration profile at the main channel, the degree of aggregation of suspended particles, and the length of mixing gyre at the entrance of the closed-end channel.

Due to the difficulty of measuring the vertical velocity profiles in the slow moving and turbid waters, the temporal and spatial variations of horizontal velocity in the channel were examined by using numerical simulation results. It was observed that the horizontal velocity at 2.5 cm elevation at a fixed location increased from zero to the maximum, then decreased and reached a steady value as time proceeded. The maximum velocity occurred at the moment when the front passed the point of interest. A steady velocity was attained even though the front continued to propagate farther downstream in the channel. It was also found that the interface elevation of the velocity profile at a fixed location increased with time, and that the velocity magnitude and

interface elevation decreased with distance from the channel entrance. At steady state, the magnitudes of flow discharge in the layers above and below the interface were equal, satisfying volumetric conservation of the fluid.

The suspension concentration at a fixed position increased rapidly from zero to a certain value (when the front was passing the location of interest), then continued increasing and eventually reached a steady value. It appears that the propagating front has little effect on concentration distribution upstream. Measured vertical concentration profiles revealed that water in the layer above the interface is not completely free of sediment. This suggests that a part of the finer particles has been transported upward by diffusion and convection. However, the characteristics of the vertical concentration profile, including relatively small concentrations in the upper layer, the elevation of maximum concentration gradient located at approximately zero-velocity elevation and relatively uniform concentration in the lower layer all suggest that a two-layered model with clear upper layer is adequate for theoretical development. The shape of the vertical concentration profile was similar at various locations in the channel, but the magnitude decreased with distance from the entrance.

In view of the good agreement for concentration distributions between experimental results and numerical simulation, the settling velocity computed from the mass balance equation, and used as input data in the numerical simulation, can be considered to appropriately represent the settling velocity of suspended particles in the channel under specific flow conditions.

Small propagating surface waves, which result from the elevated water surface during the intrusion of dense fluid, were observed in numerical simulation results. When a stationary sediment wedge is established, the water surface rises from the entrance towards the wedge toe, then continues horizontally to the end of the channel. Momentum conservation principle over the channel reach from the entrance to the wedge toe was demonstrated by the good agreement of ΔH_{max} (the maximum surface rise), obtained by an analytic approach and by numerical simulation.

Front nose height to head height ratio, h_1/h_2, was found to be strongly influenced by bottom friction, and was found to decrease with increasing local head Reynolds number, $Re_h = u_f h_2/\nu$. The consistent trend of h_1/h_2 vs. Re_h obtained from various investigations suggests that the relationship between h_1/h_2 and Re_h shown in Fig.5.21 is valid for all types of gravity currents.

An approximately constant value of the ratio of front head height to neck height, h_2/h_3, over the ranges of local neck Reynolds number, $Re_n = u_f h_3/\nu = 20$~$1,000$, and fraction depth, $h_3/H = 0.19$~0.39 was observed. The arithmetic mean of all data points for this ratio is equal to 1.3. The difference between h_2/h_3 obtained in the present study and that of Keulegan (1958), who found $h_2/h_3 = 2.0$, resulted from different ranges of h_3/H in the two studies. This observation can be supported by the finding of Simpson and Britter (1979) that h_2/h_3 should decrease with increasing the fraction depth, h_3/H. It should furthermore be noted that h_2/h_3 was found to be nearly independent of the relative settling velocity, w_s/u_f.

Dimensionless initial front speed, u_{f1}/u_{Δ}, was found to be independent of the densimetric Reynolds number, Re_{Δ}, and the width-to-depth ratio, B/H. The arithmetic mean of u_{f1}/u_{Δ} was 0.43, which is close to 0.46 obtained in Keulegan's (1957) investigation of lock exchange flow of saline water. This observation is indicative of the dynamic similarity between turbidity current and salinity-driven current during the initial stages of front propagation.

An exponential-type decrease of the dimensionless front speed $u_f/\bar{u}_{f1}$ with distance observed in the present study was due to drag force against front motion, and the reduction of motive force by sediment settling and interfacial mixing. Also, the ratio of $u_f/\bar{u}_{f1}$ was found to be strongly dependent upon the relative settling velocity, w_{s1}/u_{Δ}, for both of kaolinite and flyash III. The dimensionless front speed, $u_f/\bar{u}_{f1}$, decreased faster with distance as the relative settling velocity, w_{s1}/u_{Δ}, increased. For turbidity current, the rate of the decrease of the front speed with distance is faster than that of salinity-induced gravity current, in which the front density decreases with distance only by interfacial mixing.

Local densimetric Froude number, Fr_{Δ}, was found to increase with increasing local neck Reynolds number, Re_n, in the range of Re_n = 25-320. The values of Fr_{Δ} obtained in the present study were slightly lower than what Keulegan (1958) found, which might result from the effect of concentration stratification at the front and the use of bottom concentration for representing the mean concentration at the front.

Three distinct phases (initial adjustment phase, inertial self-similar phase, and viscous self-similar phase) found in the front propagation of salinity-induced gravity current, were also found in the front propagation of turbidity current. All three characteristic curve slopes (slope = 1, 2/3, and 1/5) corresponding to three phases were observed in tests with kaolinite. The duration of front propagation in the initial adjustment phase, in which the front proceeds at a constant speed, lasted longer for the front with smaller w_{s1}/u_{Δ}. Yet, the w_{s1}/u_{Δ} had little effect on the durations of propagation in the inertial self-similar and viscous self-similar phases. In flyash III tests, only two characteristic curve slopes (slope = 2/3, and 1/5), corresponding to the last two phases, were observed due to the high relative settling velocity, w_{s1}/u_{Δ}. In addition, the duration of front propagation in the inertial self-similar phase (slope=2/3) was longer for the front having the smaller w_{s1}/u_{Δ}.

Keulegan (1957) has pointed out that the front dilution of salinity-induced density current through interfacial mixing is faster in lock flows at relatively small Reynolds numbers. In the present study, an exponential-type decrease of dimensionless excess front density, $\Delta\rho'/\Delta\rho_d$, with distance from the entrance was observed. In this case, the decrease is due to the combined effect of sediment settling and interfacial mixing. The rate of the decrease was found to increase with increasing relative settling velocity, w_{s1}/u_{Δ}.

An exponential-type decrease with distance of mean concentration below the interface at steady state was also observed. Accordingly, the assumption of a constant mean concentration below the interface

made by many investigators for the purpose of theoretical development is inappropriate. In all tests, the rate of the decrease of dimensionless mean concentration below the interface, $\overline{C}_b/\overline{C}_{b_1}$, with distance became greater as w_{s1}/u_Δ increased. The ability of the numerical model for simulating the longitudinal distribution of mean concentration below the interface was good. The analytic derivation, eq.3.52, for the longitudinal distribution of mean concentration below the interface was found to be only good for relatively small w_{s1}/u_Δ values. Also, the discrepancy between analytic and experimental results became greater with increasing values of w_{s1}/u_Δ.

The variation of settling velocity with concentration for fine-grained sediments used was investigated by using settling column tests. It was found that the median settling velocities, w_{sm}, of flyash I, II, III, and silica flour were not completely independent of the initial column concentration, C, but increased slightly with increasing concentration. The median settling velocity of Vicksburg loess was also found to slowly increase with increasing C, over the range of C = 423-1,939 mg/l, and w_{sm} of Cedar Key mud was equal to 0.001 cm/sec for C = 323-373 mg/l. The median settling velocity of kaolinite was found to be concentration-dependent over the range of C = 443-1,500 mg/l, and could be expressed as

$$w_{sm} = 0.0001\ C^{0.79} \qquad (6.1)$$

where w_{sm} is in cm/sec, and C is in mg/l. In the range of C = 1,500-10,027 mg/l, w_{sm} of kaolinite was found to be independent of C.

As mentioned above, the settling velocity of the deposit computed from the mass balance equation was found to adequately represent the local settling velocity of suspended sediment in the channel. The settling velocity of the deposit was found to decrease with distance from the entrance in both kaolinite and flyash III tests. The rate of decrease of the dimensionless settling velocity, w_s/w_{s1}, with distance became greater as the relative settling velocity, w_{s1}/u_Δ, increased.

The uniformity of particle size distribution of the deposit was examined using a modified sorting coefficient, $(d_{85}/d_m)^{1/2}$. This coefficient was found to be approximately the same everywhere in the channel for both kaolinite and flyash III tests. The modified sorting coefficient in all steady tests using kaolinite ranged from 1.9 to 2.5, while in flyash III tests it ranged from 1.3 to 1.6. This result suggests that the particle size distribution of kaolinite deposit was more uniform than that of flyash III. Again, the median dispersed particle size of the deposit was found to decrease with distance from the entrance because of sorting effect. Because there is no unique correlation between the settling velocity of a floc and the primary constitutive particles size, as mentioned above, the dependence of distance variation of the dimensionless median dispersed particle size, d_m/d_{m1}, on w_{s1}/u_Δ in kaolinite tests was not found to be significant. In flyash III tests, the rate of the decrease of d_m/d_{m1} with distance became greater as w_{s1}/u_Δ increased.

Under turbulent flow conditions ($Re = 4R\bar{u}_o/\nu = 12{,}965 \sim 27{,}350$) in the main channel, it was found that the settling velocity of kaolinite, w_s, increased rapidly from 0.0071 cm/sec at suspension concentration $\bar{C}_o$

= 1,375 mg/l to w_s = 0.045 cm/sec at $\overline{C}_o$ = 3,746 mg/l. On the other hand, the median dispersed particle size, d_m, from which the flocs were formed, decreased from 2.78 μm at $\overline{C}_o$ = 1,375 mg/l to 1.39 μm at $\overline{C}_o$ = 3,746 mg/l. The critical deposition shear stress of kaolinite, τ_{cd}, which is defined as the shear stress below which all initially suspended sediment eventually deposits, was found to be 0.13 N/m^2, very close to 0.15 N/m^2 obtained by Mehta (1973).

A trend of flocculation factor, F, increasing with decreasing median dispersed particle size, d_m, was observed, similar to the findings by Migniot (1968) and Dixit et al. (1982). Also, that primary particles at higher concentrations tend to form relatively large flocs was observed. Three typical trends of longitudinal distribution of the flocculation factor with respect to different ranges of concentration were identified. The flocculation factor increased from entrance to x = 1.5 m due to shear-induced circulation, and at x = 1.5-2.0 m, F was large, corresponding to a high main channel concentration. At locations beyond x = 2.0 m, F rapidly decreased with distance in the test having the highest main channel concentration, $\overline{C}_o$ = 3,746 mg/l, remained unchanged with distance in the test having $\overline{C}_o$ = 2,248 mg/l, and increased slowly with distance in the tests having $\overline{C}_o$ = 908-1,375 mg/l.

Typically, there was significant sediment deposition in the zone near the entrance, followed by an approximately exponential-type decrease of deposition farther along the channel. This was the case because most particles with relatively high settling velocities kept suspended in the main channel deposited immediately due to quiescent

water in the channel. The rate of the decrease of dimensionless deposition rate, δ/δ_1, with distance consistently increased as the relative settling velocity, w_{s1}/u_Δ, increased, regardless of sediment type. The numerical model was shown to have good capability for simulating the deposition rate in the channel.

The relationship derived for predicting the sediment flux, S, into the closed-end channel by turbidity currents was

$$S = \alpha \left[\frac{gH}{\rho_w} \left(1 - \frac{1}{G_s} \right) \right]^{1/2} \bar{C}_1^{3/2} \qquad (6.2)$$

This relationship is valid not only for the closed-end channels, but also for the open-ended channels, as long as the flow condition in the channel is quiescent. Here, H is the water depth, G_s is the specific gravity of sediment, and $\bar{C}_1$ is the depth-mean concentration at the entrance. Note that the sediment flux is proportional to $H^{1/2}$ and $\bar{C}_1^{3/2}$, but is independent of sediment settling velocity.

The tide-induced to turbidity current-induced deposited mass ratio was derived as

$$\frac{M_T}{M_D} = 11.42 \left(\frac{\Delta\rho_1}{\rho_w}\right)^{-1/2} \left(\frac{a_o}{H}\right) \left(\frac{L}{L'}\right) \qquad (6.3)$$

where M_T, M_D are tide-induced and turbidity current-induced deposited sediment mass over a tidal cycle, respectively, a_o is the tidal amplitude, and L' is the tidal wave length in shallow water. The significance of tide-induced deposition becomes obvious when the area

of water surface in the channel is large, tidal range is high, the channel is shallow, and the density gradient at the entrance is low.

Based on the results of two tidal effect tests, a preliminary conclusion was drawn that water surface variations imposed in the main channel, regardless of whether the level is increasing or decreasing, will extend the duration of front propagation within the inertial self-similar phase, in which the front proceeds at a speed proportional to $t^{-1/3}$. Water surface variation had no significant effects on the longitudinal distribution of mean concentration below the interface at steady state.

6.3 Recommendations for Future Study

Although the two-dimensional, explicit, finite diffence numerical model realistically simulates the vertical movement of the free-surface and hence the propagation of surface waves, the numerical time step is severely restricted by the time required for the surface wave to propagate a distance of approximately one spatial grid. It should however be noted that the amplitude of the surface wave generated by the bottom density current is much smaller than the total water depth, and thus is not physically of concern. Using a rigid-lid model (Sheng, 1986) instead of a free-surface model for simulating the physics associated with density currents may save much computer time, and still achieve the same results.

In numerical simulation there must be temporally and spatially continuous distributions of physical quantities to keep the numerical scheme stable; therefore the suspension concentration at the sharp front was stretched out in the longitudinal direction during simula-

tion. Accordingly, this mathematical model is not applicable to detailed studies of front shape and front speed of gravity currents. For investigators interested in the front behavior of such currents, a special treatment which adopts a higher order difference approximation of a Hermite interpolation function in the convective-diffusion formulation, as suggested by Fischer (1976), can be used to improve the numerical stability and reduce numerical errors in the concentration prediction at the sharp front.

Most experiments conducted in the present study generated low Reynolds number turbidity currents (Re_Δ = 324-3,830), and the physics associated with such currents is Reynolds number-dependent. However, prototype turbidity currents typically have much higher Reynolds numbers. Thus, more realistic prototype phenomena at higher Reynolds number turbidity currents, in which the physics of concern is Reynolds number-independent, should be laboratory tested.

The method of settling column analysis is a good alternative to determine the settling velocity distribution of fine-grained sediments. A problem encountered when conducting the analysis is the significant drop of water surface in the column during suspension sample withdrawals. A minimum of 30 ml of liquid sample is needed for determining sample concentration by the gravimetric procedure. One possible way to reduce water surface reduction in the settling column, and thus improve accuracy, is by using a turbidimeter for which only a few ml of sample is required per withdrawal.

Three physical phases were identified in the front propagation of gravity currents by Huppert (1982) and Rottman and Simpson (1983).

In each phase, front propagation is dominated by specific forces, and the front position is a specific function of the elapsed time. But no unique functions were found to describe front movement from the instant of gate opening to when it reaches the closed end. In future research, if one can examine the front movement of gravity currents by looking at the net forces acting on the front, i.e. $\sum F_i = m_f(du_f/dt)$, where F_i is the component force acting on the front, and m_f is the front mass, it may be possible to find a unique relation between front speed and elapsed time.

APPENDIX A
SPATIAL GRID SYSTEM, FLOW CHART,
AND STABILITY CONDITION FOR NUMERICAL MODELING

A.1 Spatial Grid System for Numerical Modeling

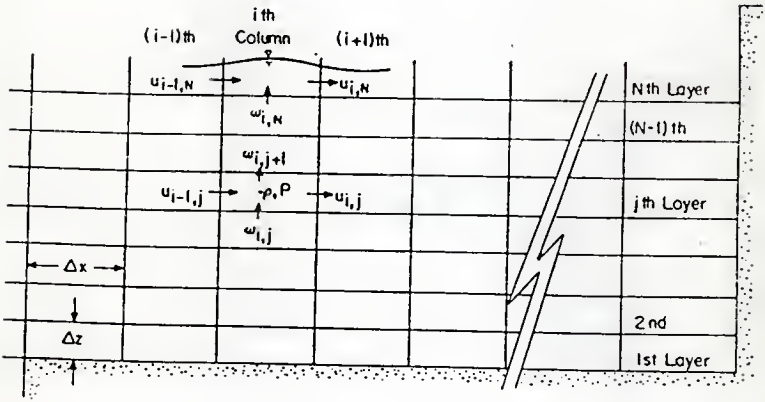

Fig.A.1. Spatial Grid System for Numerical Modeling

A.2 Flow Chart for Numerical Calculation

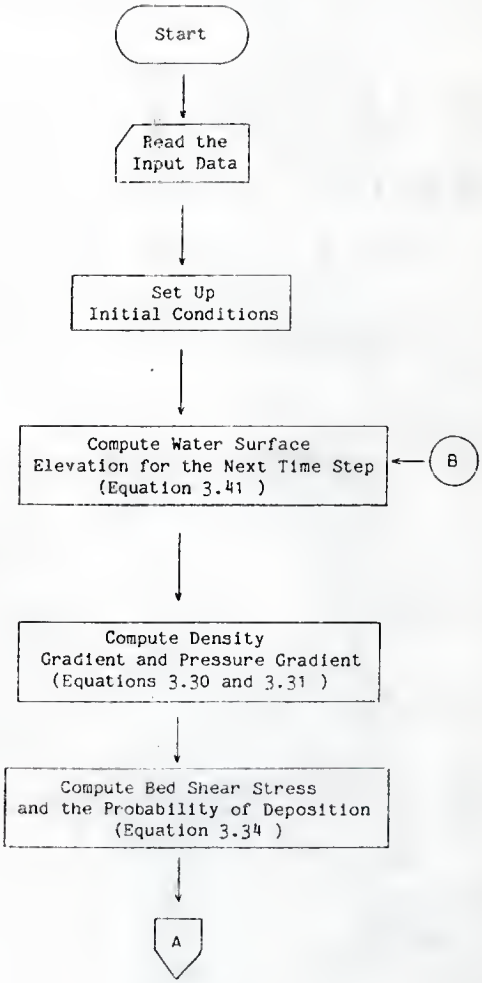

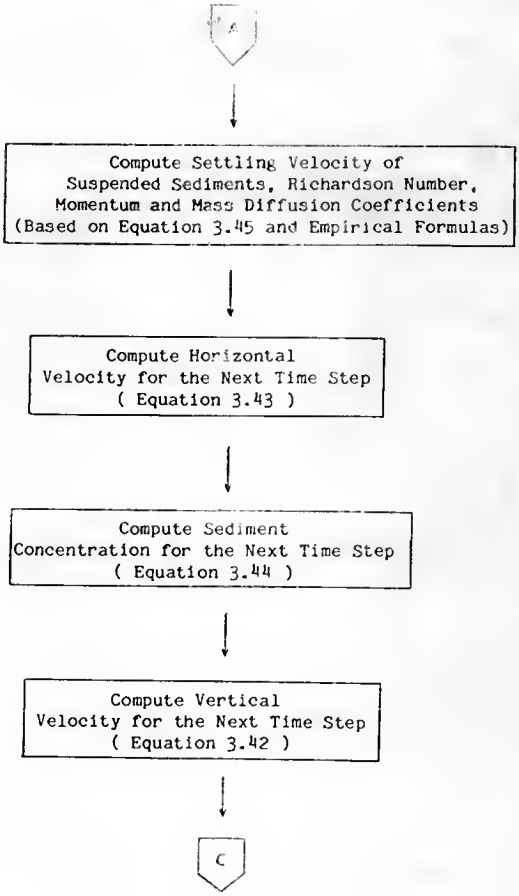
A
Compute Settling Velocity of
Suspended Sediments, Richardson Number,
Momentum and Mass Diffusion Coefficients
(Based on Equation 3.45 and Empirical Formulas)
Compute Horizontal
Velocity for the Next Time Step
(Equation 3.43)
Compute Sediment
Concentration for the Next Time Step
(Equation 3.44)
Compute Vertical
Velocity for the Next Time Step
(Equation 3.42)
C

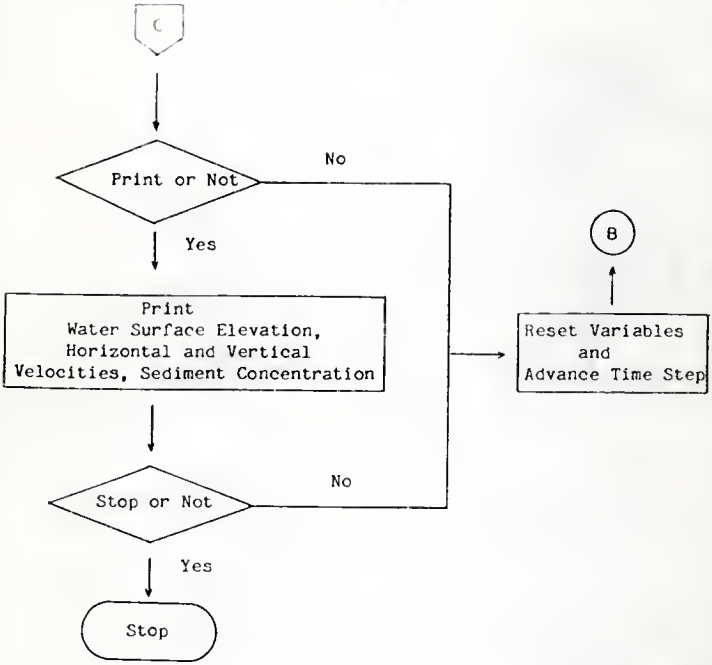
C
Print or Not
No
Yes
Print
Water Surface Elevation,
Horizontal and Vertical
Velocities, Sediment Concentration
Stop or Not
No
Yes
Stop
Reset Variables
and
Advance Time Step
B

A.3 Derivation of Numerical Stability Condition

To investigate the linear stability of eq.3.47, the continuous function f(x) can be expressed as a form of complex Fourier series (Abbott, 1979), i.e.

$$f_j^n = \sum_k F_k^n \exp\left(i \frac{2\pi k}{\lambda} j \Delta x \right) \qquad (A.1)$$

where λ is the spatial interval of periodicity. Using the same complex Fourier series expression for subsequent continuous functions

$$f_j^{n+1} = \sum_k F_k^{n+1} \exp\left(i \frac{2\pi k}{\lambda} j \Delta x \right) \qquad (A.2)$$

$$f_j^{n-1} = \sum_k F_k^{n-1} \exp\left(i \frac{2\pi k}{\lambda} j \Delta x \right) \qquad (A.3)$$

$$f_{j+1}^{n-1} = \sum_k F_k^{n-1} \exp\left[i \frac{2\pi k}{\lambda} (j+1) \Delta x \right] \qquad (A.4)$$

$$f_{j-1}^{n-1} = \sum_k F_k^{n-1} \exp\left[i \frac{2\pi k}{\lambda} (j-1) \Delta x \right] \qquad (A.5)$$

and substituting these expressions into eq.3.47, this equation will become

$$\sum_k F_k^{n+1} \exp\left(i \frac{2\pi k}{\lambda} j\Delta x\right) - \sum_k F_k^{n-1} \exp\left(i \frac{2\pi k}{\lambda} j\Delta x\right) = \frac{A(2\Delta t)}{(\Delta x)^2} \left\{ \sum_k F_k^{n-1} \exp\left[i \frac{2\pi k}{\lambda} (j+1)\Delta x\right] \right.$$

$$\left. - 2 \sum_k F_k^{n-1} \exp\left(i \frac{2\pi k}{\lambda} j\Delta x\right) + \sum_k F_k^{n-1} \exp\left[i \frac{2\pi k}{\lambda} (j-1)\Delta x\right] \right\} \qquad (A.6)$$

Next, eq.A.2 is divided by the term $\exp(i2\pi kj\Delta x/\lambda)$, and then reduced to

$$F_k^{n+1} - F_k^{n-1} = \frac{2A\Delta t}{(\Delta x)^2} \{ F_k^{n-1} \exp\left(i\frac{2\pi k}{\lambda}\Delta x\right) - 2F_k^{n-1} + F_k^{n-1} \exp\left(-i\frac{2\pi k}{\lambda}\Delta x\right) \} \qquad (A.7)$$

From eq.A.3, an "amplification factor" R_k for each K can be obtained as follows

$$R_k^2 = \frac{F_k^{n+1}}{F_k^{n-1}} = 1 + \frac{2A\Delta t}{(\Delta x)^2} [2i \sin(\pi k\Delta x/\lambda)]^2 \qquad (A.8)$$

then,

$$R_k = \pm \{ 1 - \frac{8A\Delta t}{(\Delta x)^2} \sin^2(\pi k\Delta x/\lambda) \}^{1/2} \qquad (A.9)$$

Since $\sin^2(\pi k\Delta x/\lambda)$ is always positive and less than or equal to one, the requirement that $|R_k| < 1$ is

$$0 < \frac{8A\Delta t}{(\Delta x)^2} < 2 \qquad (A.10)$$

Because A representing momentum or mass diffusion coefficent is positive, $A\Delta t/(\Delta x)^2$ is always greater than zero. Consequently,

$$\frac{A\Delta t}{(\Delta x)^2} < \frac{1}{4} \qquad (A.11)$$

APPENDIX B
FLOW REGIME IN A CLOSED-END CHANNEL

B.1 Relationship Between Suspension Concentration and Density

In the present study, the suspension concentration, C, is defined as the sediment mass contained in a unit volume of water-sediment mixture. The relationship between C and ρ can be derived as follows:

$$\rho = \frac{M_a}{\forall_o} \qquad (B.1)$$

where M_a is total mass of the water-sediment mixture, and $\forall_o$ is total volume of the mixture. However, the total mass M_a, includes the mass of fresh water, M_w, and the mass of sediment, M_s. Then, eq.B.1 becomes

$$\rho = \frac{M_w + M_s}{\forall_o} = \frac{\rho_w(\forall_o - \forall_s) + \rho_s \forall_s}{\forall_o} \qquad (B.2)$$

where $\forall_s$ is the volume of sediment contained in the mixture. The term on the right hand side, $\rho_s \forall_s / \forall_o$, is equivalent to the suspension concentration, C, i.e. $\rho_s \forall_s / \forall_o = C$. Accordingly, the proportion of volume occupied by sediment in the mixture is $\forall_s / \forall_o = C/\rho_s = C/\rho_w G_s$. Consequently, eq.B.2 can be expressed as

$$\rho = \rho_w + C \left(1 - \frac{1}{G_s} \right) \qquad (B.3)$$

or the density difference, $\Delta\rho$, between the water-sediment mixture and fresh water becomes

$$\Delta\rho = \rho - \rho_w = C\left(1 - \frac{1}{G_s}\right) \qquad (B.4)$$

B.2 Derivation of Steady State Horizontal Velocity

Equations 3.55 and 3.56 can be further reduced to

$$e_z \frac{\partial^2 u}{\partial z^2} = g \frac{\partial h}{\partial x} \qquad \eta < z < h \qquad (B.5)$$

$$e_z \frac{\partial^2 u}{\partial z_2} = g\left(\frac{\rho_w}{\rho}\right)\frac{\partial h}{\partial x} + \left(1 - \frac{1}{G_s}\right)\frac{g}{\rho}\int_z^\eta \frac{\partial C}{\partial x}\, dz \qquad 0 < z < \eta \qquad (B.6)$$

The integration in eq.B.6 can be carried out by substituting the solution of eq.3.52 into the suspension concentration C

$$\int_z^\eta \frac{\partial C}{\partial x}\, dz = \int_z^\eta \frac{\partial}{\partial x}\left\{C_1 \exp\left[-\beta\left(\frac{w_{s1}}{u_\Delta}\right)\left(\frac{x}{H}\right)\right]\right\} dz = -\beta \frac{w_{s1}}{u_\Delta H}(\eta - z)\, C \qquad (B.7)$$

Accordingly, eq.B.6 becomes

$$e_z \frac{\partial^2 u}{\partial z^2} = g\left(\frac{\rho_w}{\rho}\right)\frac{\partial h}{\partial x} + g\frac{\Delta\rho}{\rho}\left(-\beta \frac{w_{s1}}{u_\Delta H}\right)(\eta - z) \qquad (B.8)$$

where $\Delta\rho = \rho - \rho_w$. The terms on the right hand side of eq.B.5 and eq.B.8 are not functions of z, hence both equations can be integrated twice with respect to z to obtain

$$u = \theta_o + \theta_1 z + \frac{g s_o}{e_z} \frac{z^2}{2} \qquad \eta < z < h \qquad (B.9)$$

and $$u = \theta_2 + \theta_3 z + (\theta_4 + \eta\theta_5)\frac{z^2}{2} - \frac{\theta_5}{6} z^3 \qquad 0 < z < \eta \qquad (B.10)$$

where s_o is the slope of free water surface $= \partial h/\partial x$, $\theta_4 = g\rho_w s_o/(e_z\rho)$, $\theta_5 = \beta g\Delta\rho w_{s1}/(\rho u_\Delta H e_z)$, and all of θ_o, θ_1, θ_2, θ_3 are integral constants.

Applying the boundary condition of zero shear stress at water surface (i.e. $\partial u/\partial x = 0$) and the noslip boundary condition at the bed (i.e. $u = 0$) to eqs.B.9 and B.10, two integral constants of θ_1 and θ_2 can be found as $\theta_1 = -g s_o h/e_z$ and $\theta_2 = 0$. Consequently, equations B.9 and B.10 can be further reduced to

$$u = \frac{g s_o}{e_z} \left(\frac{z^2}{2} - hz \right) + \theta_o \qquad \eta < z < h \qquad (B.11)$$

and $$u = \theta_3 z + (\theta_4 + \eta\theta_5) \frac{z^2}{2} - \frac{\theta_5}{6} z^3 \qquad 0 < z < \eta \qquad (B.12)$$

Again, two other boundary conditions at the interface are utilized. These are: 1) the horizontal velocity at the interface is continuous (i.e. $u|_{\eta^+} = u|_{\eta^-}$), and 2) the slope of vertical velocity profile at the interface is continuous (i.e. $\partial u/\partial x|_{\eta^+} = \partial u/\partial x|_{\eta^-}$). Accordingly, the integral constants, θ_o and θ_3, in eqs.B.11 and B.12 can be determined as

$$\theta_o = -\frac{\theta_5}{6} \eta^3 + \left(\frac{g s_o}{e_z} - \theta_4 \right) \frac{\eta^2}{2} \qquad (B.13)$$

and $$\theta_3 = -\frac{gs_o}{e_z} h + \left(\frac{gs_o}{e_z} - \theta_4\right) \eta - \frac{\theta_5}{2} \eta^2 \qquad (B.14)$$

Finally, volumetric conservation requires that the net volumetric flow at any cross section in the channel must be equal to zero (i.e. $\int_0^h u dz = 0$). This is used to determine θ_5. Therefore θ_5 is found as

$$\theta_5 = -\frac{2gs_o}{h\xi^3(1 - 0.25\xi)e_z} \qquad (B.15)$$

where ξ is the dimensionless interface elevation = η/h.

Substituting θ_o, θ_3, and θ_5 into eqs. B.11 and B.12, the solutions for horizontal velocity in upper and lower layers, respectively, are obtained as follows:

$$u = \frac{gs_oH^2}{e_z}\left[0.5\zeta^2 - \zeta + \frac{1}{3(1 - 0.25\xi)} \right] \qquad \xi < \zeta < 1 \qquad (B.16)$$

$$u = \frac{gs_oH^2}{e_z}\left[\frac{\zeta^3}{3\xi^3(1-0.25\xi)} + \left[0.5-\frac{1}{\xi^2(1-0.25\xi)}\right]\zeta^2 + \left[-1+\frac{1}{\xi(1-0.25\xi)}\right]\zeta \right\}$$

$$0 < \zeta < \xi \qquad (B.17)$$

According to eq.B.16, the surface velocity, u_s, i.e. $\zeta = 1$, is

$$u_s = \frac{gs_oH}{e_z}\left[-0.5 + \frac{1}{3(1 - 0.25\xi)}\right] \qquad (B.18)$$

u_s is used to normalize eqs.B.16 and B.17. Eqs.B.16 and B.17 then become

$$\frac{u}{u_s} = \frac{(1.5-0.375\xi)\,\zeta^2 - (3-0.75\xi)\,\zeta + 1}{-0.5 + 0.375\,\xi} \qquad \xi < \zeta < 1 \qquad (B.19)$$

$$\frac{u}{u_s} = \frac{(\zeta/\xi)^3+(-3+1.5\xi^2-0.375\xi^3)(\zeta/\xi)^2+(3-3\xi+0.75\xi^2)(\xi/\zeta)}{-0.5 + 0.375\,\xi} \qquad 0 < \zeta < \xi$$

$$(B.20)$$

B.3 Comparison of Vertical Velocity Profiles

A comparison of vertical velocity profile between experimental, numerical, and/or analytical results is made in this section. As mentioned before, the vertical velocity profile was measured by injecting a vertical streak of dye at locations approximately 1 cm away from the side wall of the channel. Numerical predictions of the horizonal velocity were obtained from model simulation, which did not include the side wall resistance effect. Analytical solutions of steady state flow regime were obtained from eqs.B.19 and B.20. Figs.B.1(a) and (b) show the comparison of vertical velocity profiles between measured data and numerical predictions for COEL-6 test under unsteady conditions. The horizontal velocity is normalized by $|u_s|$, where u_s is the surface outflow velocity. In Fig.B.1(a), at x = 1.8 m and t = 40 minutes, u_s obtained from experimental measurement and numerical simulation are equal to -0.36 cm/sec and -0.53 cm/sec, respectively. In Fig.B.1(b), at x = 4.0 m and t = 40 minutes, experimental and numerical u_s are equal to -0.26 cm/sec and -0.25 cm/sec, respectively.

Figs.B.2(a) and (b) show the comparison of vertical velocity profiles between experimental, numerical, and analytical results

for COEL-6 test at steady state. In Fig.B.2(a), at x = 1.8 m, u_s obtained from experimental measurement and numerical prediction are equal to -0.18 cm/sec and -0.53 cm/sec, respectively. u_s of analytical solution can not be computed from the analytical formulas because of the involvement of the water surface slope, s_o, which is a very small value and not easily measurable. In Fig.B.2(b), at x = 4.0 m, the experimental and the numerical u_s are equal to -0.11 cm/sec and -0.25 cm/sec, respectively.

It is observed from all the plots mentioned above, that the shapes of vertical velocity profiles obtained from experimental, numerical, and analytical results are fairly similar. However, the magnitude of the horizontal velocity obtained from laboratory measurement was smaller than that from numerical prediction, which would be expected due to the boundary effect of the side wall.

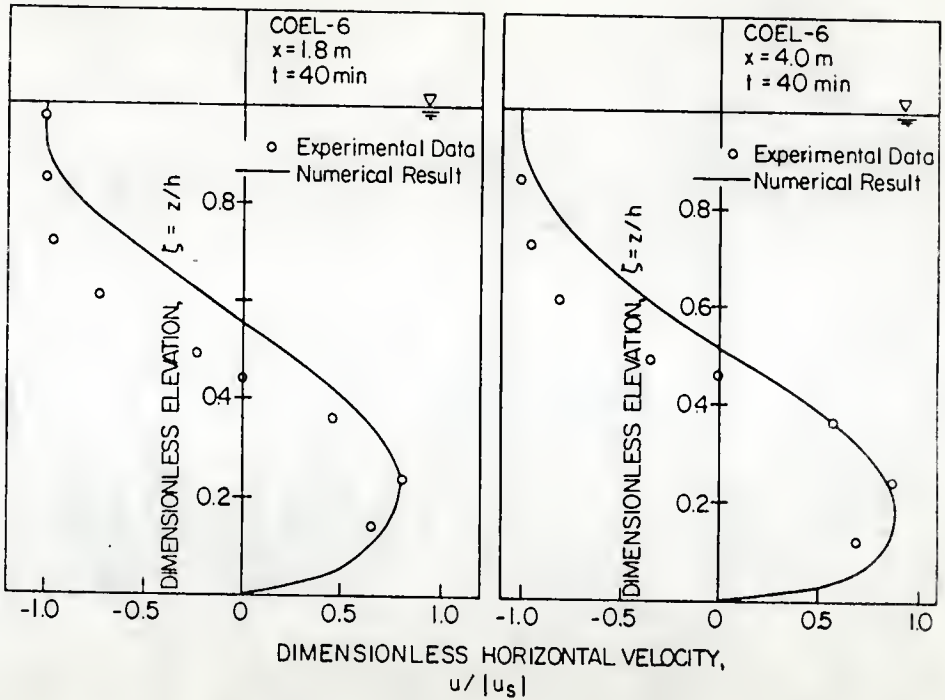

Figure B.1. Dimensionless Vertical Velocity Profiles (a) at x = 1.8 m, (b) at x = 4.0 m. (Unsteady State)

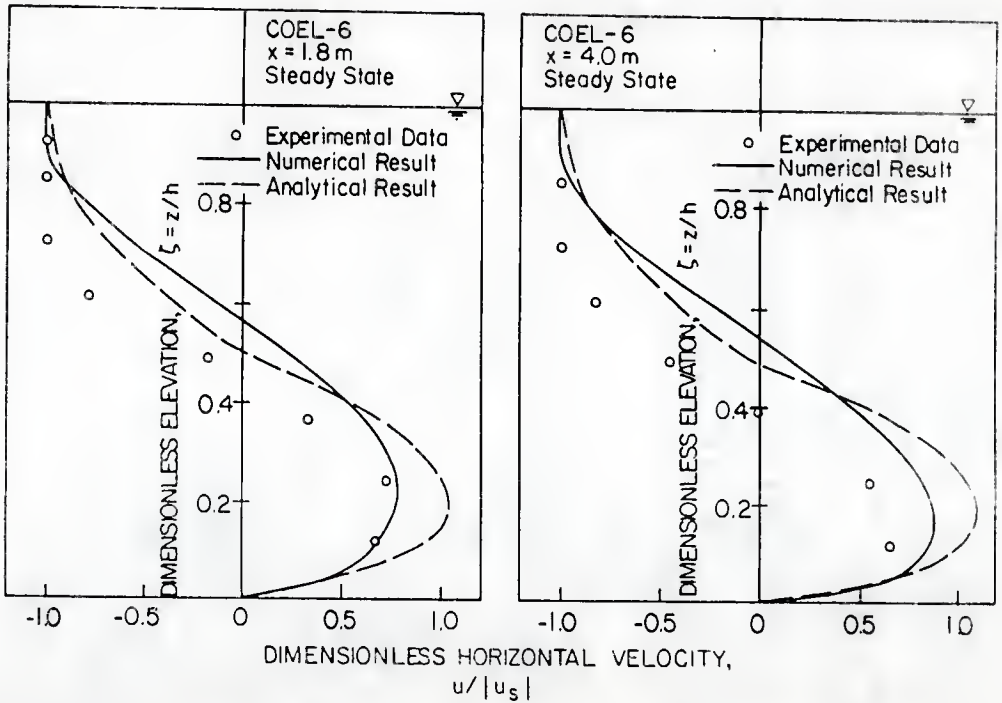

Figure B.2. Dimensionless Vertical Velocity Profiles (a) at x = 1.8 m, (b) at x = 4.0 m. (Steady State)

APPENDIX C
COMPUTATION OF MAXIMUM SURFACE RISE

When a stationary sediment wedge is established, the maximum rise of water surface in the closed-end channel can be computed using eq.3.62, which is

$$\Delta H_{max} = \frac{1}{H} \{ \frac{1}{\rho_w} \int_0^H [\int_z^H \rho_1(z)\, dz - \frac{H^2}{2}] \qquad (3.64)$$

In test COEL-5, the water depth at entrance, H=9.3 cm, the density of water, ρ_w = 0.996836 g/cm^3, and the density profile at entrance, $\rho_1(z)$, was measured. Measured values of ρ_1 at different elevations at the entrance of the closed-end channel are given in Table C.1. The term of double integrations in eq.3.62 can be expressed as a summation according to

$$\int_0^H [\int_z^H \rho_1(z)\, dz]\, dz = \sum_{i=1}^{8} [\sum_{j=i}^{8} \rho_{1j}\, \Delta z_j]\, \Delta z_i \qquad (C.1)$$

Computations of this summation are given in Table C.1.

Table C.1 Computation of Maximum Surface Rise

i	z_i (cm)	ρ_{1i} (kg/m^3)	$\rho_{1i}\Delta z_i$ (kg/m^2)	$\sum_{j=i}^{8}\rho_{1j}\Delta z_j$ (kg/m^2)	$(\sum_{j=i}^{8}\rho_{1j}\Delta z_j)\Delta z_i$ (kg/m)
8	9.3	996.836	0	0	0
7	8.5	997.116	7.977	7.977	0.032
6	7.0	997.199	14.957	22.934	0.232
5	5.5	997.243	14.958	37.892	0.456
4	4.0	997.251	14.959	52.851	0.681
3	2.5	997.251	14.959	67.810	0.905
2	1.0	997.252	14.959	82.769	1.129
1	0.0	997.252	9.970	92.740	0.878

$$\sum_{i=1}^{8}\left(\sum_{j=i}^{8}\rho_{1j}\Delta z_j\right)\Delta z_i = 4.313$$

Therefore,

$$\Delta H_{max} = \frac{1}{9.3}\left\{\frac{1}{0.996836} \times 4.313 \times 10 \times \frac{(9.3)^2}{2}\right\} = 0.024 \text{ mm}$$

APPENDIX D
CHARACTERISTICS OF CLOSED-END CHANNEL DEPOSITS

Characteristics of the deposits of closed-end channel at COEL are listed in the following table, which include sample location, median dispersed particle size, d_m, 85% finer particle size, d_{85}, and modified sorting coefficient.

Table D.1 Characteristics of Closed-End Channel Deposits.

Flume Test Number	Sample Number	Location, x (m)	d_m (μm)	d_{85} (μm)	Sorting Coefficient
2	1	0.00U - 0.50U	4.12	23.6	2.4
	2	0.00D - 0.500	3.08	15.5	2.2
	3	0.00 - 0.50	1.82	9.6	2.3
	4	0.50 - 1.00	1.40	8.3	2.4
	5	1.00 - 1.50	1.40	6.8	2.2
	6	1.50 - 2.00	1.38	5.6	2.0
	7	2.00 - 2.50	1.18	5.4	2.1
	8	2.50 - 3.50	1.17	5.3	2.1
	9	3.50 - 5.00	1.00*	4.5	2.1
	10	5.00 - 7.00	—	—	—
3	1	0.50U - 0.50D	4.32	20.3	2.2
	2	0.00 - 1.00	2.50	13.3	2.3
	3	1.00 - 2.00	1.81	8.0	2.1
	4	2.00 - 3.50	1.46	6.1	2.0
	5	3.50 - 7.00	0.96*	4.6	2.2
4	1	0.75U - 0.50D	4.14	18.2	2.1
	2	0.00 - 3.00	2.78	10.7	2.0
	3	3.00 - 10.00	0.91*	4.3	2.2

* indicates extrapolated data
U represents a location at the upstream of the main channel from the center of the closed-end channel
O represents a location at the downstream of the main channel from the center of the closed-end channel

Table D.1 — continued

Flume Test Number	Sample Number	Location, x (m)	d_m (μm)	d_{85} (μm)	Sorting Coefficient
5	1	0.00U – 0.50U	3.72	23.3	2.5
	2	0.00 – 3.00	2.78	14.3	2.2
	3	3.00 – 10.00	1.07*	3.9	1.9
6	1	0.00U – 0.50U	22.90	43.0*	1.4
	2	0.00 – 2.00	12.40	24.9	1.4
	3	2.00 – 6.00	6.01	12.1	1.4
7	1	0.50U – 0.50D	24.55	44.5*	1.3
	2	0.00 – 1.50	13.41	27.5	1.4
	3	1.50 – 4.50	6.21	11.2	1.3
8	1	0.50U – 0.50D	29.47	50.8*	1.3
	2	0.00 – 2.00	14.15	34.5	1.6
9	1	0.00U – 0.50U	2.89	15.7	2.3
	2	0.00 – 3.00	1.69	9.4	2.4
	3	3.00 – 10.00	0.77*	4.4	2.4
12	1	0.00 – 8.00	9.71	38.2	2.0
13	1	0.50U – 0.75U	1.84	14.2	2.8
	2	0.00 – 0.56	1.39	9.9	2.7
	3	0.63 – 2.63	1.26	8.7	2.6
	4	4.00 – 7.00	0.52*	2.9	2.4
14	1	0.50U – 0.75U	1.83	14.1	2.8
	2	0.00 – 0.53	1.70	13.2	2.8
	3	0.69 – 2.69	1.71	7.6	2.1
	4	4.00 – 7.00	0.61*	3.2	2.3

* indicates extrapolated data

U represents a location at the upstream of the main channel from the center of the closed-end channel

D represents a location at the downstream of the main channel from the center of the closed-end channel

REFERENCES

Abbott, M. B., Computational Hydraulics: Elements of the Theory of Free Surface Flows, Pitman Publishing Ltd., London, 1979.

Akiyama, J. and Stefan, H., "Turbidity Current with Erosion and Deposition," Journal of Hyraulic Division, American Society of Civil Engineers, Vol.111, No. 12, December, 1985, pp.1473-1496.

American Society for Testing and Materials, "Standard Method for Particle-Size Analysis of Soils (designation D422-63)," 1983 Annual Book of ASTM Standards, Vol. 04.08, ASTM, Philadelphia, Pennsylvania, 1983.

Ariathurai, R., A Finite Element Model for Sediment Transport in Estuary, Ph.D Dissertation, University of California, Davis, California, 1974.

Ariathurai, R., and Krone, R. B., "Finite Element Model for Cohesive Sediment Transport," Journal of Hydraulic Division, American Society of Civil Engineers, Vol. 102, No. HY3, 1976, pp. 323-338.

Ariathurai, R., MacArthur, R. C., and Krone, R. G., Mathematical Model of Estuarial Sediment Transport, Technical Report D-77-12, U.S. Army Engineers Waterway Experiment Station, Vicksburg, Mississippi, October, 1977.

Bagnold, R. A., "Auto-Suspension of Transported Sediment: Turbidity Current," Proceedings of Royal Society of London, Vol. 265, Series A, 1962, pp. 315-319.

Bailard, J. A., Jenkins, S., and Dellaripa, F., Assessment of Crossbe-th Circulation at Charleston Naval Station, Technical Note No. N-1729, Naval Civil Engineering Laboratory, Port Hueneme, California, August, 1985.

Barr, D. I. H., "Densimetric Exchange Flow in Rectangular Channels, I: Definitions, Review and Relevance to Model Design," La Houille Blanche, Vol. 7, 1963a, pp. 739-753.

Barr, D. I. H., "Densimetric Exchange Flow in Rectangular Channels, II: Some Observations of Structures of Lock Exchange Flow," La Houille Blanche, Vol. 7, 1963b, pp. 757-766.

Barr, D. I. H., "Densimetric Exchange flows in Rectangular Channels, III: Large Scale Experiments," La Houille Blanche, Vol. 22, 1967,

pp. 619-631.

Benjamin, T. B., "Gravity Currents and Related Phenomena," Journal of Fluid Mechanics, Vol.31, Part 2, 1968, pp. 209-248.

Bowden, K. F. and Hamilton, P., "Some Experiments with A Numerical Model of Circulation and Mixing in A Tidal Estuary," Estuarine and Coastal Marine Science, N. C. Flemming, editor, Vol. 3, No. 3, Academic Press, New York, July, 1975, pp.281-301.

Braucher, E. P., Initial Characteristics of Density Current Flow, M. S. Thesis, Massachusetts Institute of Technology, Cambridge, Massachusetts, 1950.

Brocard, D. N. and Harleman, D. R. F.,"Two-Layer Model for Shallow Horizontal Convective Circulation," Journal of Fluid Mechanics, Vol. 100, Part 1, 1980, pp. 129-146.

Christodoulou, G. C., Leimkuhler, W. F., and Ippen, A. T., Mathematical Models of the Massachusetts Bay: Part III, A Mathematical Model for the Dispersion of Suspended Sediments in Coastal Waters, Report No. 179, Ralph M. Parsons Laboratory, Massachusetts Institute of Technology, Cambridge, Massachusetts, January, 1974.

Daily, J. W., and Harleman, D. R. F., Fluid Dynamics, Addison-Wesley Publishing Company, Massachusetts, 1966.

Didden, N. and Maxworthy, T., "The Viscous Spreading of Plane and Axisymmetric Gravity Currents," Journal of Fluid Mechanics, Vol. 121, 1982, pp. 27-42.

Dixit, J. G., , Resuspension Potential of Deposited Kaolinite Beds, M. S. Thesis, University of Florida, Gainesville, Florida, 1982.

Dixit, J. G., Mehta, A. J., and Partheniades, E., Redepositional Properties of Cohesive Sediments Deposited in a Long Flume, UFL/COEL-82/002, Coastal and Oceanographic Engineering Department, University of Florida, Gainesville, Florida, August, 1982.

Dyer, K. R., Estuaries: A Physical Introduction, John Wiley & Sons, New York, 1973.

Festa, J. F. and Hansen, D. V., " A Two-Dimensional Numerical Model of Esturine Circulation: the Effect of Alternating Depth and River Discharge," Estuarine and Coastal Marine Science, N. C. Flemming, editor, Vol.4, No.3, Academic Press, New York, July, 1976, pp. 309-323.

Fischer, K., "Numerical Model for Density Currents in Estuaries," Proceedings of the Fifteenth Coastal Engineering Conference, Vol. 4, American Society of Civil Engineers, Hononulu, Hawaii, July, 1976, pp. 3295-3311.

Gole, C. V., Tarapore, Z. S.. and Gadre, M. R., "Siltation in Tidal Docks Due To Density Currents," Proceedings of the Fifteenth Congress of International Association for Hydraulic Research, Vol.1, Istanbul, Turkey, 1973, pp.335-340.

Guy, H. P., "Pipet Method," Sedimentation Engineering: Manuals and Reports on Engineering Practice No. 54, V. A. Vanoni, editor, American Society of Civil Engineers, New York, 1975, pp. 416-418.

Halliwell, A. R. and O'Dell, M., "Density Currents and Turbulent Diffusion in Locks," Proceedings of the Twelfth Coastal Engineering Conference, Vol. III, American Society of Civil Engineers, Washington, D. C., September, 1970, pp. 1959-1977.

Hoffman, J. F., "Sediment Problems and Their Control in U.S. Navy Pier Slips in Selected Harbors of the United States," Estuarine Comparisons: Proceedings of the Sixth Biennial International Estuarine Research Conference, V. S. Kennedy, editor, Academic Press, New York, 1982, PP. 623-633.

Hunt, J. R., "Prediction of Oceanic Particle Size Distribution from Coagulation and Sedimentation Mechanisms," In Advances in Chemistry Series No. 189-Particles in Water, M. D. Kavanaugh and J. O. Keckie, editors, American Chemical Society, Washington, D. C., 1980, pp. 243-257.

Huppert, H. E., "The Propagation of Two-Dimensional and Axisymmetric Viscous Gravity Currents over A Rigid Horizontal Surface," Journal of Fluid Mechanics, Vol. 121, 1982, pp. 43-58.

Huppert, H. E. and Simpson, J. E., "The Slumping of Gravity Currents," Journal of Fluid Mechanics, Vol. 99, Part 4, 1980, pp. 785-799.

Interagency Committee, A Study of New Methods for Size Analysis of Suspended Sediment Samples, Report No. 7, Federal Inter-departmental Committee, Hydraulic Laboratory of the Iowa Institute of Hydraulic Research, Iowa City, Iowa, 1943.

Ippen, A. T., and Harleman, D. R. F., "Steady-State Characteristics of Subsurface Flow," Proceedings of NBS Symposium on Gravity Waves, Circular No.521, National Bureau of Standards, November, 1952, pp. 79-93.

Kao, T. W., "Density Currents and Their Applications," Journal of Hydraulic division, American Society of Civil Engineers, Vol. 103, No. HY5, May, 1977, pp. 543-555.

Kármán, T. Von, "The Engineer Grapples with Nonlinear Problems," Bulletin of American Mathematical Society, Vol. 46, 1940, pp. 615-683.

Keulegan, G. H., An Experimental Stuoy of the Motion of Saline Water from Locks into Fresh Water Channels, Report No. 5168, National Bureau of Standards, March, 1957.

Keulegan, G. H., The Motion of Saline Fronts in Still Water, Report No.5831, National Bureau of Standards, April, 1958.

Keulegan, G. H., "The Mechanism of an arrested Saline Wedge," Estuary and Coastline Hydrodynamics, A. T. Ippen, editor, Chapter 11, McGraw-Hill Book Company, New York, June, 1966, pp. 546-574.

Komar, P. D., "Computer Simulation of Turbidity Current Flow and the Study of Deep-Sea Channels and Fan Sedimentation," The Sea: Ideas and Observations on Progress in the Study of the Seas, Vol. 6, Marine Modeling, E. D. Goldberg, et al., editors, John Wiley & Sons Inc., New York, 1977, pp. 603-621.

Krone, R. B., Flumes Studies of the Transport of Sediment in Estuarial Shoaling Processes, Final Report, Hydraulic Engineering Laboratory and Sanitary Engineering Research Laboratory, University of California, Berkeley, California, June, 1962.

Kuo, A., Nichols, M., and Lewis, J., Modeling Sediment Movement in the Turbidity Maximum of an Estuary, Bulletin 111, Virginia Institute of Marine Science, Gloucester Point, Virginia, 1978.

Lawson, T. J., "Haboob Structure at Khartoum," Weather, Vol.26, 1971, pp. 105-112.

Lin, C. P. and Mehta, A. J. "Sediment-driven Density Fronts in Closed End Canals," Lecture Notes on Coastal and Estuarine Studies, Vol. 16: Physics of Shallow Estuaries and Bays, J. Van de Kreeke, editor, Springer-Verlag, New York, 1986, pp.259-276.

Lott, J. W., Laboratory Study on the Behavior of Turbidity Current in A Closed-End Channel, M. S. Thesis, University of Florida, Gainesville, Florida, 1986.

McDowell, D. M., "Currents Induced in Water by Settling Solids," Proceedings of the Fourteenth Congress of International Association for Hydraulic Research, Vol. 1, Paris, France, September, 1971, pp. 191-198.

McLaughlin, R. T., " The Settling Properties of Suspensions," Journal of Hydraulic Division, American Society of Civil Engineers, Vol. 85, No. HY12, December, 1959, pp. 9-41.

Mehta, A. J., Depositional Behavior of Cohesive Sediments, Ph.D Dissertation, University of Florida, Gainesville, Florida, 1973.

Mehta, A. J., "Characterization of Cohesive Sediment Properties and Transport Processes in Estuaries," Lecture Notes on Coastal and Estuarine Studies, Vol. 14: Estuarine Cohesive Sediment Dynamics, A. J. Mehta, editor, Springer-Verlag, New York, 1986, pp. 290-325.

Mehta, A. J., Partheniades, E., Dixit, J., and McAnally, W. H., "Properties of Deposited Kaolinite in a Long Flume," Proceedings of Hydraulic Division Conference on Applying Research to Hydraulic Practice, American Society of Civil Engineers, Jackson, Mississippi, August, 1982.

Middleton, G. V., "Experiments on Density and Turbidity Currents. I. Motion of the Head," Canadian Journal of Earth Sciences, Vol. 3, 1966a, pp. 523-546.

Middleton, G. V, "Experiments on Density and Turbidity Currents, II. Uniform Flow of Density Current," Canadian Journal of Earth Sciences, Vol. 3, 1966b, pp. 627-637.

Middleton, G. V., "Experiments on Density and Turbidity Currents, III. Deposition of Sediment," Canadian Journal of Earth Sciences, Vol. 4, 1967, pp. 475-505.

Migniot, C., "A Study of the Physical Properties of Different Very Fine Sediments and their Behavior under Hydrodynamic Action," La Houille Blanche, No. 7, 1968, pp.591-620. (In French, with English abstract).

Miles, G. V., Formulation and Development of A Multi-Layer Model of Estuarine Flow, Report No. INT 155, Hydraulic Research Station, Wallingford, England, 1977.

O'Brien, M. P., and Cherno, J., "Model Law for Salt Water through Fresh," Transactions, American Society of Civil Engineers, 1934, pp. 576-609.

Odd, N. V. M., and Owen, M. W., "A Two-Layer Model for Mud Transport in the Thames Estuary," Proceedings of the Institution of Civil Engineering, London, Supplement (ix), 1972, pp. 175-205.

O'Dell, M., Silt Distributions and Siltation Processes (with Particular Reference to the Mersey Estuary and Dock Systems), Ph.D Dissertation, Liverpool University, Liverpool, England, December, 1969.

Owen, M. W., Determination of the Settling Velocities of Cohesive Muds, Report No. IT 161, Hydraulic Research Station, Wallingford, England, October, 1976.

Pallesen, T. R., Turbidity Current, Series Paper No. 32, Institute of Hydrodynamics and Hydraulic Engineering, Technical University of Denmark, Lyngby, Denmark, January, 1983.

Parchure, T. M., Erosional Behavior of Deposited Cohesive Sediments, Ph.D. Dissertation, University of Florida, Gainesville, Florida, 1983.

Parchure, T. M., and Mehta, A. J., "Erosion of Soft Cohesive Sediment Deposits," Journal of Hydraulic Division, American Society of Civil Engineering, Vol. 111, No. HY10, October, 1985, pp. 1308-1326.

Perrels, P. A. J., and Karelse, M., "A Two-Dimensional, Laterally Averaged Model for Salt Intrusion in Estuaries," Transport Models for Inland and Coastal Waters, H. B. Fischer, editor, Academic Press, New York, 1981, pp.483-535.

Pritchard, D. W., "The Movement and Mixing of Contaminants in Tidal Estuaries," Proceedings of the First International Conference on Waste Disposal in the Marine Environment, University of California at Berkeley, Pergamon Press, New York, 1960, pp. 512-525.

Richardson, J. F., and Zaki, W. N., "The Sedimentation of a Suspension of Uniform Spheres under Conditions of Viscous Flow," Chemical Engineering Science, Vol. 3, 1954, pp. 65-72.

Roache, P. J., Computational Fluid Dynamics, Hermosa Publishing, Albuquerque, NM, 1972.

Rottman, J. W. and Simpson, J. E., "Gravity Currents Produced by Instantaneous Releases of A Heavy Fluid in A Rectangular Channel," Journal of Fluid Mechanics, Vol. 135, 1983, pp. 95-110.

Schijf, J. B. and Schonfeld, J. C., " Theoretical Considerations on the Motion of Salt and Fresh water," Proceedings of Minnesota International Hydraulic Convention, Minneapolis, Minnesota, 1953, pp.321-333.

Sheng, Y. P., " Finite-Difference Models for Hydrodynamics of Lakes and Shallow Seas," Physics-Based on Modeling of Lakes, Reservoirs, and Impoundments, American Society of Civil Engineers, January, 1986, pp. 146-228.

Simmons, H. B., "Field Experience in Estuaries," Estuary and Coastline Hydrodynamics, A. T. Ippen, editor, McGraw-Hill Book Company, New York, 1966, pp. 673-690.

Simpson, J. E., "Effect of the Lower Boundary on the Head of a Gravity Current," Journal of Fluid Mechanics, Vol.53, 1972, pp. 757-768.

Simpson, J. E., "Gravity Currents in the Laboratory, Atmosphere, and Ocean," Annual Review of Fluid Mechanics, Vol.14, 1982, pp. 213-234.

Simpson, J. E., and Britter, R. E., "The Dynamics of the Head of A Gravity Current Advancing over A Horizontal Surface," Journal of Fluid Mechanics, Vol.94, 1979, pp. 477-495.

Streeter, V. L. and Wylie, E. B., Fluid Mechanics, McGraw-Hill, Inc., New York, 1975.

Sturm, T. M. and Kennedy, J. F., "Heat Loss from Sidearms of Cooling Lakes," Journal of Hydraulic Division, American Society of Civil Engineers, Vol. 106, No. HY5, May, 1980, pp. 783-804.

Teeter, A. M., "Investigations on Atchafalaya Bay Sediment," Proceedings of the Conference on Frontiers in Hydraulic Engineering, American Society of Civil Engineers, Cambridge, Massachusetts, August, 1983, pp. 85-90.

Tesaker, E., "Modelling of Suspension Currents," Proceedings of the Second Annual Symposium on Modeling Techniques, Vol. II, WaterWays, Harbors, and Coastal Engineering Division, American Society of Civil Engineers, New York, September, 1975, pp. 1385-1401.

Thorn, M. F. C., "Physical Processes of Siltation in Tidal Channel," Proceeding Hydraulic Modeling Applied to Maritime Engineering Problems, ICE, London, 1981, pp. 47-55.

Turner, J. S., Bouyancy Effects in Fluids, Cambridge University Press, Cambridge, England, 1979.

van de Kreeke, J., Carpenter, J. H., and McKeehan, D. S., "Water Motions in Closed-End Residential Canals," Journal of the Waterway, Port, Coastal and Ocean Division, American Society of Civil Engineers, Vol.103, No. WW1, February, 1977, pp. 161-166.

Wanless, H. R., Sedimentation in Canals, Division of Marine Geology and Geophysics, Rosenstiel School of Marine and Atmospheric Science, University of Miami, Miami, Florida, 1975.

Wood, I. R., Studies in Unsteady Self Preserving Turbulent Flows, Report No. 81, Water Research Laboratory, University of New South Wales, Manly Vale, Australia, 1965.

Yih, C. S., Dynamics of Nonhomogeneous Fluids, The Macmillan Company, New York, 1965.

BIOGRAPHICAL SKETCH

The author was born October 31, 1954, in Taipei, Taiwan, Republic of China. He attended National Cheng Kung University at Tainan and majored in hydraulic engineering from September 1973 to June 1977. In June 1977 he graduated with a Bachelor of Science degree. He worked as an assistant engineer in the Water Resources Planning and Design Bureau at Taipei from September 1977 to September 1978. In September 1978 he was employed as research and teaching assistant in the Department of Hydraulic Engineering at National Cheng Kung University. In the meantime, he enrolled as a graduate student at the same university and majored in ocean engineering. He graduated from National Cheng Kung University in June 1980 with a Master of Science degree. In the period between June 1980 and August 1982 he continued working as research and teaching assistant at the same department.

He entered graduate school at the University of Florida in September 1982 in the Department of Civil Engineering to work toward the Doctor of Philosophy degree. He has been working as a graduate research assistant in the Coastal and Oceanographic Engineering Department since September 1982.

I certify that I have read this study and that in my opinion it conforms to acceptable standards of scholarly presentation and is fully adequate, in scope and quality, as a dissertation for the degree of Doctor of Philosophy.

Ashish J. Mehta

Ashish J. Mehta, Chairman
Associate Professor of Civil Engineering

I certify that I have read this study and that in my opinion it conforms to acceptable standards of scholarly presentation and is fully adequate, in scope and quality, as a dissertation for the degree of Doctor of Philosophy.

B.A. Christensen

Bent A. Christensen
Professor of Civil Engineering

I certify that I have read this study and that in my opinion it conforms to acceptable standards of scholarly presentation and is fully adequate, in scope and quality, as a dissertation for the degree of Doctor of Philosophy.

Robert G. Dean

Robert G. Dean
Graduate Research Professor of Coastal and Oceanographic Engineering

I certify that I have read this study and that in my opinion it conforms to acceptable standards of scholarly presentation and is fully adequate, in scope and quality, as a dissertation for the degree of Doctor of Philosophy.

D. Max Sheppard

Donald M. Sheppard
Professor of Coastal and Oceanographic Engineering

I certify that I have read this study and that in my opinion it conforms to acceptable standards of scholarly presentation and is fully adequate, in scope and quality, as a dissertation for the degree of Doctor of Philosophy.

Arun Kumar Varma

Arun K. Varma
Professor of Mathematics

This dissertation was submitted to the Graduate Faculty of the College of Engineering and to the Graduate School and was accepted as partial fulfillment of the requirements for the degree of Doctor of Philosophy.

May, 1987

Dean, College of Engineering

Dean, Graduate School

UNIVERSITY OF FLORIDA
3 1262 08552 3222